HOKKAIDO UNIVERSITY

| | |
|---|---|
| Title | Seismic Imaging of the Upper Mantle with Multi-mode Surface Waves Using Broadband Seismic Arrays |
| Author(s) | 松澤, 仁志 |
| Degree Grantor | 北海道大学 |
| Degree Name | 博士(理学) |
| Dissertation Number | 甲第14368号 |
| Issue Date | 2021-03-25 |
| DOI | https://doi.org/10.14943/doctoral.k14368 |
| Doc URL | https://hdl.handle.net/2115/81971 |
| Type | doctoral thesis |
| File Information | Hitoshi_Matsuzawa.pdf |

Hokkaido University Collection of Scholarly and Academic Papers : HUSCAP

# Seismic Imaging of the Upper Mantle with Multi-mode Surface Waves Using Broadband Seismic Arrays

（広帯域地震観測網を用いたマルチモード表面波による
上部マントルの地震学的イメージング）

**Hitoshi Matsuzawa**

A thesis submitted for
the degree of Doctor of Philosophy

Department of Natural History Sciences
Graduate School of Science
Hokkaido University

March 2021

# Abstract

Seismic surface waves are powerful means to map the heterogeneity and the anisotropy in the upper mantle. The use of higher-mode surface waves is essential for enhancing the vertical resolution of seismic tomography models since they are much more sensitive to the deep structure of the Earth's mantle than fundamental-mode surface waves. However, measuring multi-mode phase speeds is not a straightforward issue since wavetrains of different modes overlap each other in a seismogram, which cannot readily be separated.

Recently, a number of high-density broad-band seismic networks have been deployed in many continental areas. One of the most remarkable continent-wide arrays is the high-density Transportable Array (USArray) in North America. The North American continent encompasses a variety of complex structural features, including tectonically active regions and stable cratons. The deployment of USArray across the contiguous United States has facilitated seismological studies to unravel the crust and mantle structure of the North American upper mantle. To delineate the deep root of the cratonic lithosphere and asthenosphere, the use of higher-mode surface waves is essential, although such studies have still been limited.

In the first half of this study, we developed the two-step array-based method for higher-mode analysis, consisting of (1) multi-mode phase speed measurements based on a classical $f$-$k$ analysis using a long-range linear array of several-thousand kilometers (e.g., Nolet, 1975) and (2) modal waveform decomposition for the centroid location of a linear array using the linear

Radon transform (e.g., Luo et al., 2015). The synthetic experiments reveal that the precise measurement of multi-mode phase speeds requires a long linear array, longer than 2000—3000 km. The extracted dispersion curves well represent the weighted-average structure depending on the station distribution in a linear array. The decomposed modal waveforms at the centroid of an array match well with theoretically predicted waveforms. These decomposed waveforms can be used to perform subsequent dispersion analyses.

By applying our linear array-based method to a large data set of seismograms at USArray, we mapped phase speed distributions in North America. We could obtain reliable phase speed maps of the fundamental-mode surface waves. Although the large-scale anomalies (i.e., fast anomalies in cratons in the stable eastern U.S., slow anomalies in the tectonically-active western U.S.) can be identified, the lateral resolution of the phase speed maps was insufficient compared to the inter-station/array-based tomography models. This suggests that the small-scale tectonic features tend to be blurred and averaged out due to the use of long linear arrays (2000–4000 km).

In the latter half of this study, we employed the single-station method of multi-mode dispersion measurements based on a fully nonlinear waveform fitting method (Yoshizawa & Kennett, 2002a; Yoshizawa & Ekström, 2010) to extract the multi-mode phase speeds for each source-receiver path for permanent and temporary stations in North America. These measurements are then applied to the array-based eikonal tomography (Lin et al., 2009). At first, in this hybrid approach, multi-mode phase speeds for all stations from each seismic event are used to reconstruct travel-time fields by tracking the phase front for each mode and period. The phase speed distributions derived from the lateral gradient of travel-time fields are stacked and averaged for all events to reconstruct the final phase speed maps. Our hybrid method is applied to teleseismic events ($M \geq 5.8$) from 2007 to 2015, including over 700

events for Rayleigh and Love waves. The contiguous United States can be covered with many single-station ray paths (e.g., over 100000 paths for the fundamental-mode Rayleigh wave at 100.0 s), which allows us to reconstruct phase speed models with $3.0^\circ \times 3.0^\circ$ grids.

We could successfully retrieve phase speed maps of Love and Rayleigh waves for the fundamental-mode and up to the 4th higher modes with this hybrid approach. The images of small-scale features in the U.S., such as the Snake River Plains, Colorado Plateau and Rio Grande Rift, are well imaged in the eikonal tomography models for the fundamental mode. Some large-scale tectonic features are imaged in the higher-mode models, such as the fast anomaly related to deep cratonic root. However, the interpretation of the higher-mode phase speed maps is not straightforward due to their complicated vertical sensitivities.

These multi-mode phase speed maps are then used to map a radially anisotropic 3-D shear wave model in a wide depth range, including the continental lithosphere and asthenosphere in the U.S. The multi-mode phase speed maps in a wide period range allow us to image the continental mantle to the depth of the transition zone. We can image the root of the cratonic lithosphere at the depth of around 200–250 km. The model of the radially anisotropic parameter ($\xi = (V_{SH}/V_{SV})^2$) have shown faster SH wave speed ($\xi > 1$) under North America at depth shallower than 100 km and faster SV wave speed ($\xi < 1$) corresponding to the slab subduction and the possible delamination of the cratonic keel deeper than 250 km depth.

# Acknowledgements

First of all, I would like to thank my supervisor, Professor Kazunori Yoshizawa. He has given me many advice and suggestions during the course of this study. Without his great support, I could not make progress in my study for this thesis. He has provided me with several opportunities to participate in academic meetings and workshops to present my results and interact with researchers from other institutions.

I also acknowledge the helpful comments provided by Professor Kiyoshi Yomogida. His essential and sharp points made me think objectively about my research. Also, I talked with him about various topics other than research, which made my laboratory life even more enjoyable. I am grateful to Professors Junji Koyama, Kosuke Heki, Masato Furuya, Youichiro Takada, and Kei Katsumata for their comments and discussions.

Professor Fan-Chi Lin (University of Utah) has kindly become my host during my visit to his laboratory twice (in Utah and Taiwan), giving me irreplaceable and valuable opportunities. He has always been kind to me during my stay in the United States and Taiwan. It was my first time to stay abroad for a long time, so his kindness helped relieve my anxiety. He has given me the idea of combining the multi-mode single-station analysis and the eikonal tomography and provided the code for his eikonal tomography.

I also thank many researchers for their comments and discussions for my presentations at meetings and workshops: Professors Hitoshi Kawakatsu, Kiwamu Nishida, Akiko Takeo, Takehi Isse (ERI, the University of Tokyo).

I also thank the fellow students and alumni of the Solid Earth Geophysics Seminar at Hokkaido University. Some have kindly provided me with much advice on my research; others have discussed my study and something else.

During my PhD course, the JSPS fellowship supported me, and this work was partly supported by JSPS KAKENHI Grant Number 18J22114. I used MINEOS v1.0.2 (Masters et al., 2011) published under the GPL2 license and distributed from Computational Infrastructure for Geodynamics for the calculations of synthetic seismograms. I also used the code of the inter-station phase speed measurements with a nonlinear waveform fitting developed by Hamada & Yoshizawa (2015), single-station phase speed measurements by Yoshizawa & Ekström (2010), surface wave tomography code by Yoshizawa & Kennett (2004), and the eikonal tomography code by Lin et al. (2009). I used the FORTRAN subroutine in Numerical Recipes for various calculations and the GMT5 (Wessel et al., 2013) for making figures. The IRIS Data Management Center provides all seismograms used in this study. I would like to thank them for providing software (e.g., SAC (Seismic Analysis Code), SOD (Standing Order for Data)) and seismic waveform data.

# Contents

*Abstract* . . . . . i
*Acknowledgements* . . . . . iv

**1 Introduction** **1**
1.1 Upper mantle imaging using surface waves . . . . . 1
1.2 Multi-mode surface wave studies . . . . . 2
1.3 Array-based surface wave studies . . . . . 6
1.4 Recent progress in surface wave mapping . . . . . 7
1.5 The scope of this study . . . . . 12

**2 Linear array analysis for multi-mode dispersion measurements of surface waves** **16**
2.1 Introduction . . . . . 16
2.2 Methods of Linear-array Analysis . . . . . 16
2.2.1 Multi-mode surface-wave dispersion measurements . . . 16
2.2.2 Decomposition into modal waveforms . . . . . 22
2.2.3 Numerical experiments for the effect of array length . . 24
2.2.4 Numerical experiments for heterogeneous models . . . 31
2.3 Application to Observed Data in USArray . . . . . 32
2.3.1 Multi-mode dispersion measurements . . . . . 32
2.3.2 2-D mini-array analysis with the decomposed modal waveforms . . . . . 37
2.4 Discussion . . . . . 38

**3 Phase Speed Mapping with a Linear-array Method 47**

3.1 Introduction . . . . . 47

3.2 Methods for Phase Speed Mapping . . . . . 47

3.2.1 Phase speed maps (1): the direct use of long linear arrays 48

3.2.2 Phase speed maps (2): inter-centroid (inter-station) dispersion analysis . . . . . 48

3.2.3 Phase speed maps (3): eikonal tomography with 2-D array analysis . . . . . 49

3.3 Data and Processing . . . . . 51

3.3.1 Linear-array phase speed measurements . . . . . 51

3.3.2 Inter-centroid phase speed measurements . . . . . 53

3.3.3 Phase travel times at linear-array centroids for eikonal tomography . . . . . 56

3.4 Three-types of Phase Speed Maps with Linear-array Measurements . . . . . 56

3.5 Discussion . . . . . 64

**4 A Hybrid Approach for Multi-mode Phase Speed Mapping: Single-station Dispersion Measurements and Eikonal Tomography 67**

4.1 Introduction . . . . . 67

4.2 Method of Single-station Multi-mode Dispersion Measurements 68

4.3 Data Sets . . . . . 71

4.3.1 Data for hybrid phase speed mapping . . . . . 71

4.3.2 Data for the linearized inversion . . . . . 78

4.4 Phase Speed Maps with Single-station and Hybrid Methods . 79

4.5 Discussion . . . . . 84

**5 Radially Anisotropic 3-D Shear Wave Structure in North**

**America Using Array-based Multi-mode Phase Speed Mapping** **89**

5.1 Introduction . . . . . 89

5.2 Method of Inversions for 1-D S-wave Models . . . . . 89

5.3 3-D S-wave Models in North America with USArray . . . . . 94

5.4 Discussion . . . . . 96

**6 Conclusions and Future Directions** **105**

6.1 Summary of this thesis . . . . . 105

6.2 Discussion on multi-mode dispersion analyses and their applications to structural reconstruction . . . . . 107

6.3 Future directions . . . . . 109

**A Methods for Linear Array Analysis** **111**

A.1 Multi-mode Phase Speed Measurements . . . . . 111

A.2 Linear Radon Transform . . . . . 117

**Bibliography** **119**

# Chapter 1

# Introduction

Seismic imaging of detailed three-dimensional structures of the Earth's mantle is one of the most important topics in global seismology and physics of the Earth's interior. Understanding the structure and dynamic processes in the Earth can be the basis of geosciences by unraveling the history and evolution of the Earth and the plate tectonic and mantle dynamic processes that have taken place in the Earth's interior. Seismic surface waves enable us to reconstruct spatial variations of the heterogeneity and anisotropy in the upper mantle, which directly reflect the dynamic processes in the solid Earth. In this chapter, we first review a variety of methods used in the surface wave analysis and their application to tomographic studies in the upper mantle. Then we will overview the objective and contents of this thesis.

## 1.1 Upper mantle imaging using surface waves

Seismic surface waves (Love and Rayleigh waves) are sensitive to Earth's shallow layers and have been the major sources of information for investigating the lateral variations of both heterogeneity and anisotropy in the crust and upper mantle. Surface waves are characterized by their large amplitude and dispersive characters, representing the frequency dependence of propagation speeds. They can be represented by the summation of Earth's normal

modes, which comprise the fundamental-mode with a large amplitude and several higher-modes or overtones equivalent to multiply reverberated body-wave arrivals (e.g., Aki & Richards, 2002; Dahlen & Tromp, 1998).

There are various types of surface wave observables, such as phase speed, group speed, amplitude anomaly, arrival-angle anomaly and Rayleigh wave's ellipticity, all of which are primarily sensitive mostly to the shear wave structure in the crust and upper mantle. Fig. 1.1 displays the vertical sensitivity kernels of phases speeds of Rayleigh and Love waves calculated for Preliminary Reference Earth Model (PREM, Dziewoński & Anderson, 1981). Since surface-wave phase speeds are sensitive to the S-wave structure at different depths depending on mode and period (e.g., Takeuti & Saito, 1972; Dahlen & Tromp, 1998), we can construct a 3-D S-wave structure from multi-mode phase speeds of surface waves.

Tomographic studies using surface waves have been initiated in early1980s (e.g., Nakanishi & Anderson, 1982, 1983; Tanimoto & Anderson, 1985). Several methods for phase speed measurements were devised based on the single-station analysis (e.g., Levshin et al., 1972), the inter-station (two-station) analysis (e.g., Dziewoński & Hales, 1972), and the multiple-station analysis (e.g., Nolet, 1975; Cara, 1978). Of these three types, the single-station method has been widely employed due to the limited numbers of seismic stations in the world in earlier days of tomographic studies. They were employed for constructing many global-scale seismic tomography models (e.g., Trampert & Woodhouse, 1995; Ekström et al., 1997).

## 1.2 Multi-mode surface wave studies

Higher-mode surface waves have multiple sensitivity peaks in deeper parts of the mantle than the fundamental mode so that they can be of help in imaging the deep mantle. However, the phase speed measurements of higher

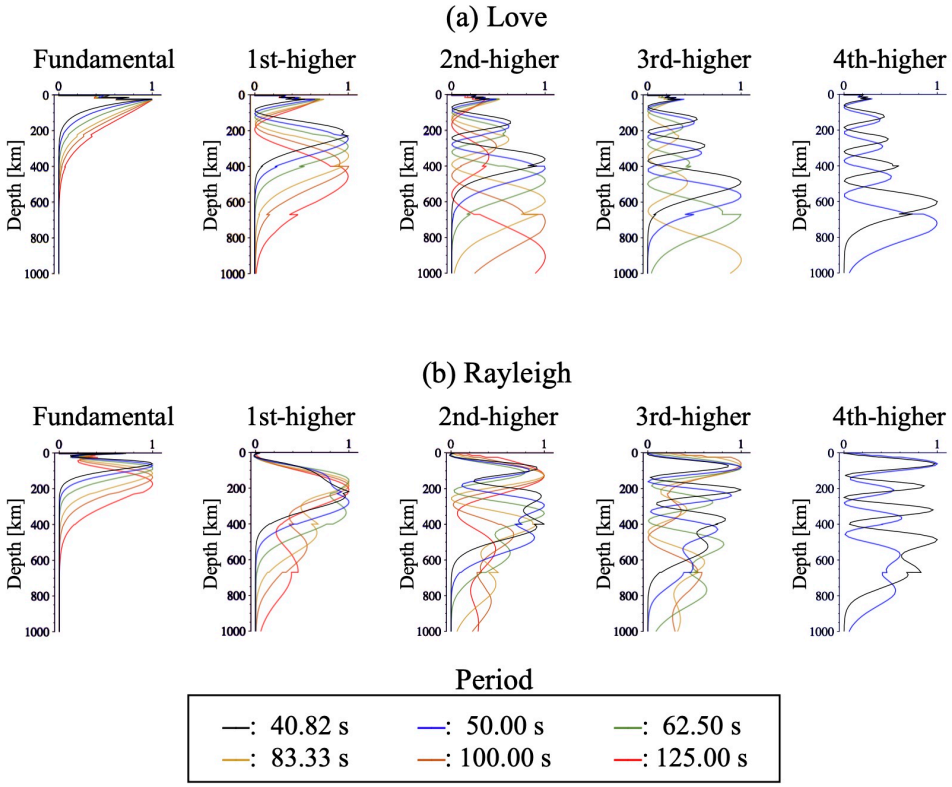



Figure 1.1: Example of vertical sensitivity kernels of (a) the multi-mode Love waves and (b) the multi-mode Rayleigh waves calculated for PREM (Preliminary Reference Earth Model by Dziewoński & Anderson (1981)) at a period of (black) 40.8 s, (blue) 50.0 s, (green) 62.5 s, (brown) 83.3 s, (yellow) 100.0 s and (red) 125.0 s. Solid lines represent the sensitivity of phase speed to S-wave speed. These sensitivity kernels are calculated by DISPER80 (Saito, 1988).

modes are intrinsically difficult since the wavetrains of several higher modes propagate with similar group speeds and overlap each other in a seismogram. For example, as Foster et al. (2014c) reported, we cannot ignore the effects of the higher-mode contamination on the fundamental-mode Love waves, which causes about 10% errors in the Love-wave phase speeds measured by the conventional inter-station analysis.

Most of the current practical techniques to measure multi-mode phase dispersions are based on the single-station methods (e.g., van Heijst & Woodhouse, 1997; Stutzmann & Montagner, 1993; Beucler et al., 2003; Yoshizawa & Kennett, 2002a). van Heijst & Woodhouse (1997) developed the mode-branch stripping technique to separate several overtones through iterative fitting and stripping processes. A phase speed dispersion curve of a given mode with the largest amplitude is first measured using cross-correlation functions; then, the corresponding mode-branch waveform is subtracted from the original seismogram, repeating this procedure for several mode-branches in order of relative amplitude. Stutzmann & Montagner (1993) presented a different method using a set of seismograms of teleseismic events at different depths in the same area recorded at the same station. Beucler et al. (2003) proposed a so-called 'roller-coaster' technique in which the phase velocity perturbation is obtained by fitting synthetic seismograms to real data.

An alternative method for measuring higher-mode phase speeds is based on a nonlinear waveform fitting technique originally developed by Yoshizawa & Kennett (2002a) and have been automated later by Yoshizawa & Ekström (2010), in which a path-specific 1-D profile is used as a guide to represent multi-mode phase dispersion curves. Similar approaches were also employed by Visser et al. (2007, 2008), and Xu & Beghein (2019), who utilized the hierarchical transdimensional Bayesian approach for nonlinear waveform fittings.

The applications of higher-mode phase speed data to tomographic reconstruction have been limited to large-scale (global or regional-scale) studies based on either single-station multimode dispersion measurements (e.g., van Heijst & Woodhouse, 1999; Beucler et al., 2003; Yoshizawa & Kennett, 2004; Visser et al., 2008; Yoshizawa & Ekström, 2010; Yoshizawa, 2014) or extracting path-average 1-D models through waveform fittings, such as, Partitioned Waveform Inversion (PWI), Automated Multi-mode Inversion(AMI) that are subsequently used to construct 3-D S velocity models (e.g., Nolet, 1990; van der Lee & Nolet, 1997a; Debayle & Kennett, 2000; Lebedev et al., 2005).

Practical techniques for the measurement of higher-mode phase speeds in tomographic mapping have been mostly based on the waveform analysis with a single-station (source–receiver) path; the mode-branch stripping method (van Heijst & Woodhouse, 1997; van Heijst & Woodhouse, 1999) and the nonlinear waveform fitting method (Yoshizawa & Kennett, 2002a; Visser et al., 2007; Yoshizawa & Ekström, 2010). There are some intrinsic limitations in these single-station approaches. First, the single-station method requires synthetic seismograms that are influenced by uncertainties in the estimated source parameters. Second, the epicentral distance must be longer than 30° for the mode-branch stripping, and 10° for the nonlinear waveform fitting to avoid the severe overlapping by the preceding body-wave arrivals. Furthermore, the overlapped modes make it difficult to extract each modal contribution in an observed seismogram, and thus the reliable measurements of higher-mode phase speeds can be available only in the limited frequency range.

An alternative approach for measuring higher-mode phase dispersions is a classical array-based analysis using a long-range linear array (Nolet, 1975, 1976; Nolet & Panza, 1976; Cara, 1978; Cara & Minster, 1981), which

enables us to extract the average multi-mode phase speeds over the array. In this technique, the slant-stacking process of multiple seismograms reduces the influence of noise included in each seismogram while enhancing coherent signals. One of the most important advantages of this array analysis is that any information of source mechanisms is not required since we do not need to use synthetic seismograms. However, this classical method has not been applied to modern high-density broad-band seismic arrays yet. One of the main reasons is that this style of linear array analyses has been considered it unable to assess localized structural variations within a linear array (e.g., Laske & Widmer-Schnidrig, 2015).

## 1.3 Array-based surface wave studies

Some classical methods for the multi-mode phase speed measurements based on an array-based analysis with a long linear array were developed in the 1970s, and their validities and limitations were investigated in earlier studies (e.g., Nolet, 1975, 1976; Nolet & Panza, 1976; Cara, 1978; Cara & Minster, 1981). These studies are based on a beamforming technique with a time-variant filter such as a group-speed windowing to separate different higher-mode branches, which enables us to extract the average phase speeds along the array. Using a power spectrogram in the "phase-speed"-"group-speed" domain at a fixed frequency, the spectral peaks corresponding to overlapped modes can be separated well each other. Nolet & Panza (1976) showed that the precision of phase speed measurements largely depends on a linear-array size through synthetic experiments. These approaches have been applied to the seismograms recorded along a linear array of long-period stations for studying structures in Western Europe and North America (Nolet, 1975, 1976; Cara et al., 1980, 1981).

There are some studies that have proposed new mode separation tech-

niques based on a 1-D-array-based analysis in the last decade. Datta (2019) tried to implement a *fk*–MUSIC method (Schmidt, 1986; Goldstein & Archuleta, 1987), which was developed originally for the signal processing used in electrical engineering applications, for extracting the multi-mode phase dispersions. Luo et al. (2015) have proposed a method for decomposing fundamental-mode Love waves from observed waveforms in which multiple mode signals are overlapped, based on the linear Radon transform with the iterative conjugate gradient algorithm (Luo et al., 2008, 2009). Using a set of decomposed single-mode waveforms, more precise measurements of Love wave phase speeds can be made by inter-station analysis or array-based analysis.

With a dense 2-D broad-band array, the $f$-$k$ analysis with beamformings can be used to estimate average phase speeds as well as arrival angles of surface waves in the array (e.g., Alvizuri & Tanimoto, 2011; Tanimoto & Prindle, 2011). Foster et al. (2014a) mapped arrival-angle anomalies in the U.S. from the array-based analysis, which investigated the wave propagation across the array and model accuracy. The development of high-density broad-band seismic arrays, such as the USArray, also facilitates the studies of new approaches for surface wave analysis using multiple seismic stations. For example, Forsyth & Li (2005) developed the multiple plane wave method to estimate both phase speeds and arrival-angles for each of two incoming plane waves. Eikonal tomography with phase front tracking (Lin et al., 2009) and its extension to a finite-frequency case, Helmholtz tomography (Lin & Ritzwoller, 2011), have been used mainly for ambient noise tomography.

## 1.4 Recent progress in surface wave mapping

Recently, high-density broad-band seismic networks have been developed in many regions in the world, for example, Transportable Array (TA) of USArray in the United States in Fig. 1.2 (e.g., Busby et al., 2018), SKIPPY and its

succeeding arrays deployed throughout Australia, F-net Broadband Seismograph Network in Japan, NECESSArray in north-eastern China, AlpArray around the Alps Mountains in Europe. Seismic waveform data derived from these high-density broad-band arrays have been of great help in enhancing our knowledge of the crust and upper mantle structures in many continental regions in the last two decades.

For example, the Transportable Array in the U.S. (USArray) as a part of the Earthscope project was launched in 2004 to investigate the deep Earth structure under the North American continent (Fig. 1.3). Its deployments started from the western quarter of the U.S. and reached the east coast in 2013. Each station continued to record the ground motion for two years, then gradually migrates to the eastern region of the contiguous U.S. Broad-band seismic stations comprising USArray were installed with nearly about 70° km grid spacing, which has allowed us to construct high-resolution regional-scale phase speed maps and 3-D shear wave models at an unprecedented lateral resolution. Both teleseismic earthquake signals (e.g., Yoshizawa & Ekström, 2010; Foster et al., 2014b; Hamada & Yoshizawa, 2015; Schaeffer & Lebedev, 2014) and ambient noise (Lin et al., 2009; Lin & Ritzwoller, 2011; Jin & Gaherty, 2015; Ekström, 2017) have been widely used for the model construction in the U.S. and North America. Foster et al. (2014b) and Hamada & Yoshizawa (2015) achieved about 100-km lateral resolution for the fundamental-mode model by using the inter-station method. Yoshizawa & Ekström (2010) constructed higher-mode phase speed models in North America using the single-station method with a fully nonlinear waveform fitting.

Combining surface-wave waveforms and SKS splitting measurements, Yuan & Romanowicz (2010) and Yuan et al. (2011) constructed 3-D radially and azimuthally anisotropic models of the North American upper mantle. Their

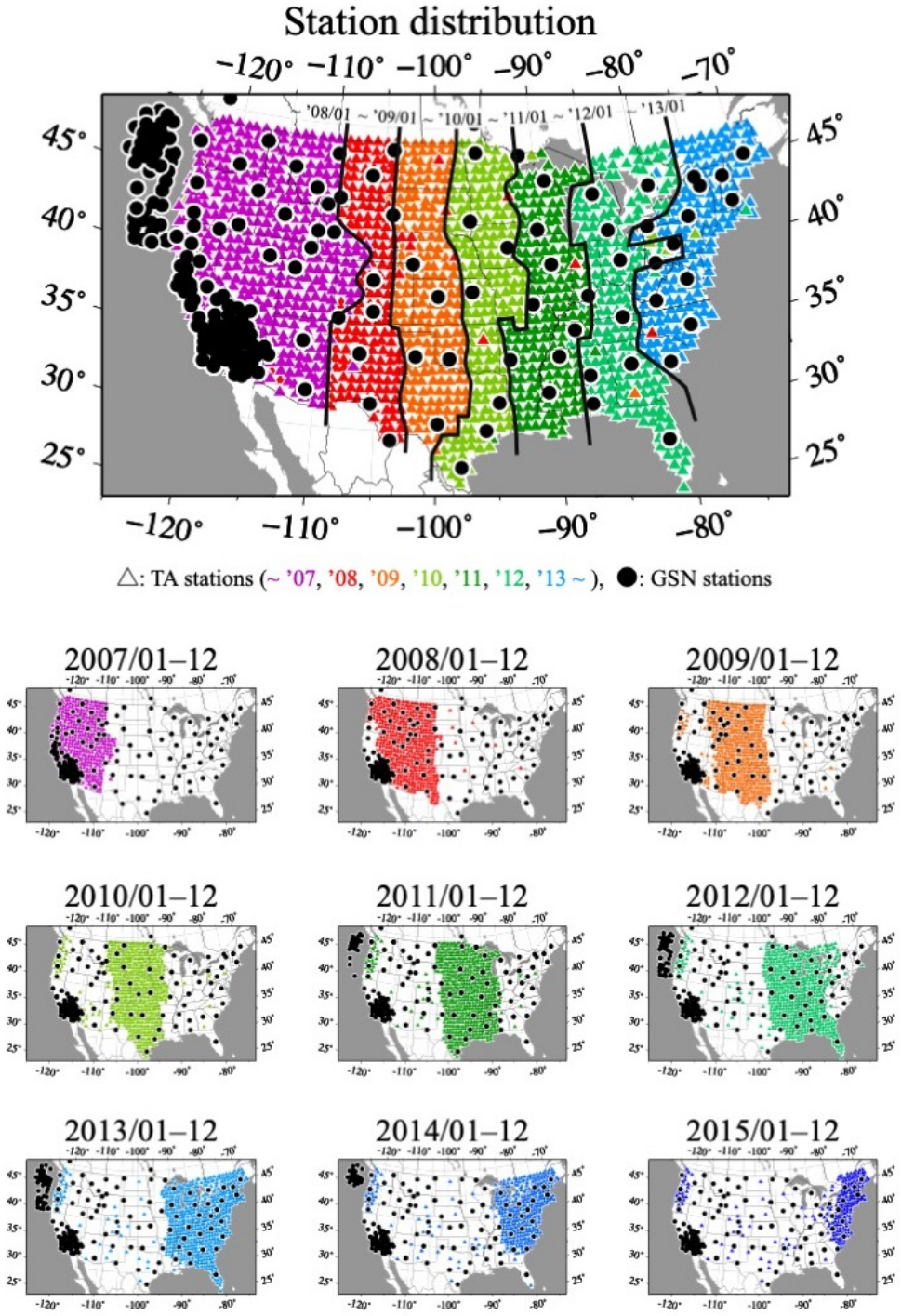



Figure 1.2: Configuration of US Transportable Array and GSN stations. Top panel shows all of the station in 2007–2015 and bottom panel shows the stations for each year.

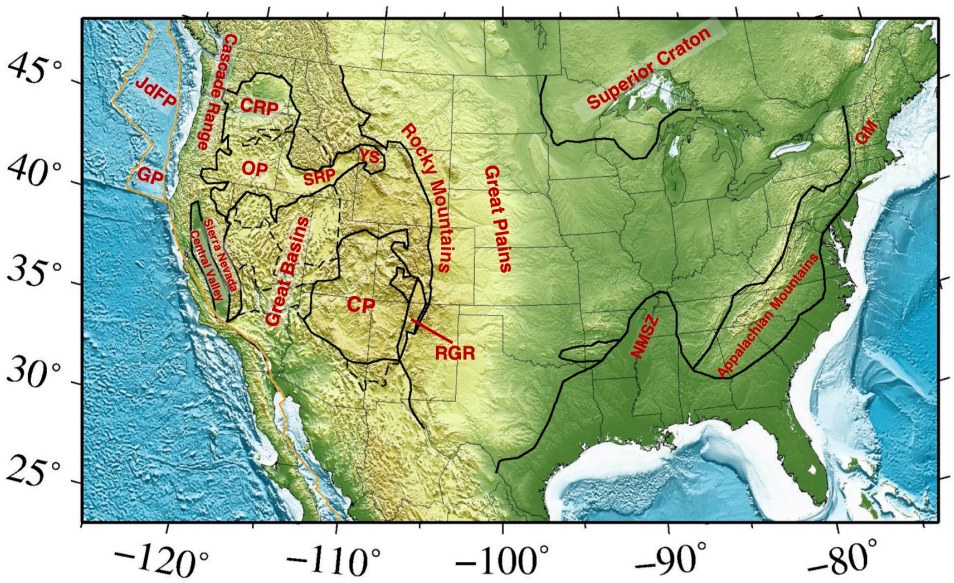



Figure 1.3: Topographic map of North America. CP: Colorado Plateau, CRP: Columbia River Plateau, NMSZ: New Madrid Seismic Zone, OP: Oregon Plateau, RGR: Rio Grande Rift, SRP: Snake River Plains, YS: Yellow Stone Hotspot, GP: Gorda Plate and JdFP: Juan de Fuca Plate. The boundaries between the geoprovinces are repoducted from Reed & Bush (2007).

azimuthally anisotropic models show depth dependence of fast directions of shear wave propagations. In their model, two anisotropic layers within the cratonic lithosphere beneath North America were found, which was interpreted as chemical and thermal boundary layers in the continental lithosphere. Nettles & Dziewoński (2008) inverted radial anisotropy from Rayleigh and Love wave dispersion data in the Pacific and North America. They suggested notable difference in radial anisotropy beneath oceans and continents. In particular, anomalously faster SH wave speed than SV was found under the Pacific plate. A high-resolution Pacific plate model has recently also been obtained by using multi-mode surface waves incorporating the data from broad-band ocean bottom seismic networks (e.g., Isse et al., 2019).

There are also many tomographic studies by a joint inversion of surface wave phase speeds and other observations; for example, the amplitude anomalies (Hamada & Yoshizawa, 2015), Rayleigh wave ellipticity (e.g., Lin et al., 2012) and receiver functions (e.g., Bodin et al., 2016; Calò et al., 2016; Taira & Yoshizawa, 2020). The amplitude data of surface waves can be of help to recover the strength of heterogeneity since they are sensitive to the lateral variations of velocity gradient (Hamada & Yoshizawa, 2015). Rayleigh-wave ellipticity is sensitive to the shallower layer than phase speeds, which can be used as a strong constraint on sediment layers and the shallow crust depending on the employed frequency (Tsuboi & Saito, 1983; Tanimoto & Tsuboi, 2009). Bodin et al. (2016) and Calò et al. (2016) employed joint inversion of phase speeds and receiver functions with a trans-dimensional Bayesian method, which resulted in the layered structure model beneath North America. A similar method has also been applied to the Australian continent incorporating higher-mode dispersion data by Taira & Yoshizawa (2020). Kaban et al. (2015) have constructed a 3-D compositional density model by using gravity and topography data with estimated mantle temper-

ature from the 3-D S-wave model derived from the earlier North American tomography model by van der Lee & Nolet (1997b) and revealed the deformed root of the Superior craton due to the basal drag by the convecting mantle under the cratonic lithosphere.

## 1.5 The scope of this study

This thesis develops and implements some new approaches for dispersion analysis of multi-mode surface waves using dense broad-band seismic networks. We employ hybrid approaches incorporating several different techniques to reconstruct the 3-D mantle structure with multi-mode surface waves. The overlapped modes in an observed seismogram can be separated and measured by phase speeds of each mode using long-range linear seismic arrays. Furthermore, with a two-dimensional array, we can estimate average phase speeds of surface waves propagating in arbitrary directions due to the effects of lateral heterogeneity and anisotropy, enabling us to enhance the accurate reconstruction of seismic structure in the Earth. The multiple approaches for waveform analyses and mapping processes in this thesis are summarized in the flow chart shown in Fig. 1.4.

In chapters 2 and 3, we employ our original method of multi-mode dispersion analysis based on the 1-D linear array analysis (Matsuzawa & Yoshizawa, 2019). This is a two-step array-based method for multi-mode surface wave analysis (Matsuzawa, 2018; Matsuzawa & Yoshizawa, 2019); (1) multi-mode phase speed measurements based on a classical $f$–$k$ analysis modeled on an early work of Nolet (1976), and (2) modal waveform decomposition for the centroid location of an array, based on the linear Radon transform (Luo et al., 2008). In chapter 2, we summarize the methodology for the linear array-based analysis and demonstrate its validity through synthetic experiments and application to observed data in USArray. In chapter 3, using the

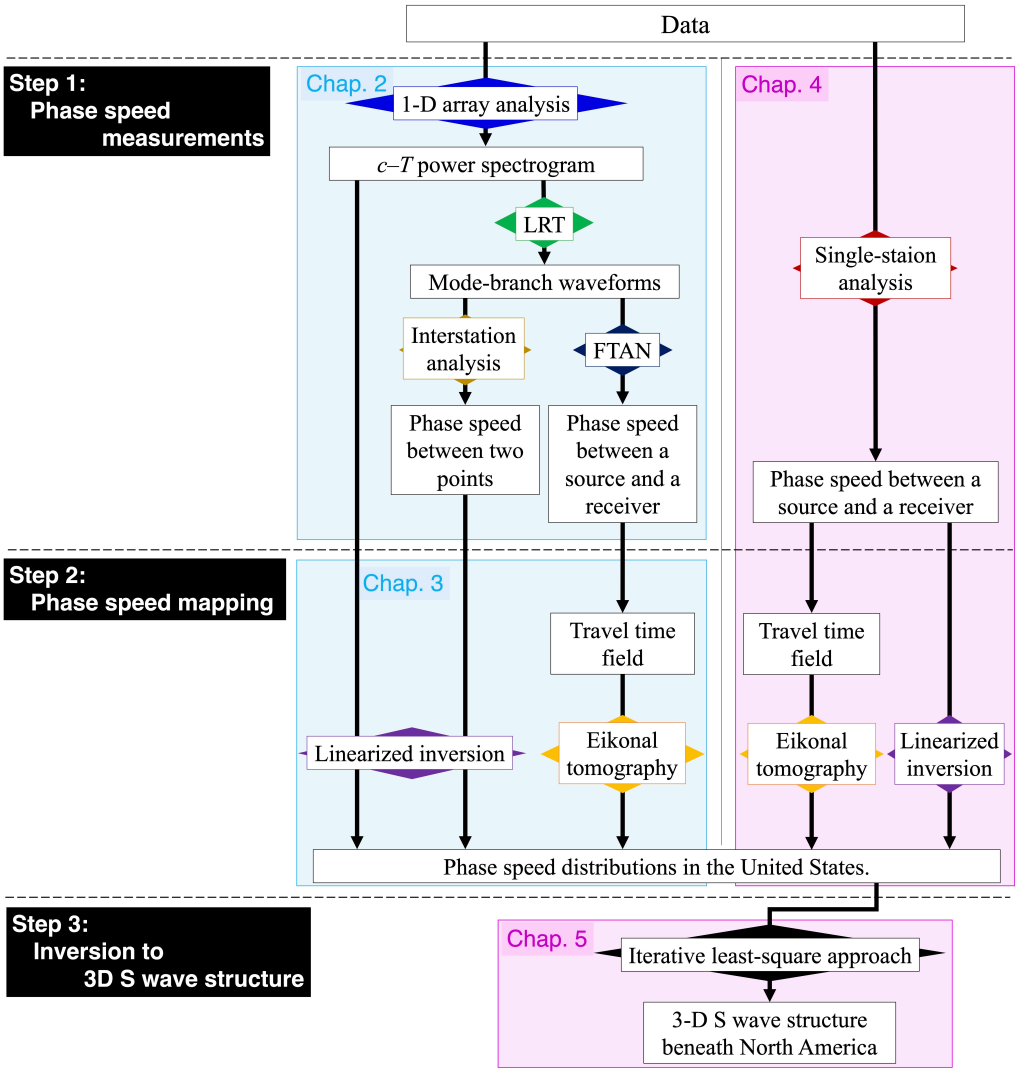



Figure 1.4: The flow chart of this thesis.

phase speeds the modal waveforms decomposed at the centroid of the linear array, we construct several types of phase speed maps in the United States derived from the following three approaches:

(a) direct use of average phase speeds of the long linear array,

(b) inter-station (inter-centroid) phase speeds (Hamada & Yoshizawa, 2015),

(c) eikonal tomography (Lin et al., 2009) based on the phase tracking across the 2-D array using the mode-branch waveforms at the centroids.

We will demonstrate and discuss the utility and limitations of the linear array-based analysis by comparing the above different phase speed mapping approaches.

In chapters 4 and 5, we propose and employ an alternative hybrid approach for multi-mode phase speed measurements and structural mapping, combining the single-station multi-mode dispersion measurement and the eikonal tomography. In chapter 4, we first show the results of the single-station multi-mode dispersion measurements based on the fully nonlinear waveform fitting by Yoshizawa & Kennett (2002a); Yoshizawa & Ekström (2010) for USArray stations. This multi-mode dispersion analysis naturally enables us to separate modal contributions from the overlapped modes. The collected phase speed data for the dense seismic network allows us to track the phase front of each mode, so that we can construct high-resolution phase speed models in the U.S. using the eikonal tomography including several higher-mode waves. These eikonal tomography models are also compared with another type of phase speed models derived from the conventional linearized inversion, which appears to be contaminated by uneven path coverage. Using these multi-mode phase speed maps in chapter 4, we construct radially anisotropic 3-D S wave speed models in the U.S. in chapter 5 and

discuss the structural characteristics and their tectonic and geodynamic implications. We will then summarize the results of this thesis in chapter 6, with some indications for future works.

# Chapter 2

# Linear array analysis for multi-mode dispersion measurements of surface waves

## 2.1 Introduction

In this study, we use the two-step array-based method developed by Matsuzawa (2018) and Matsuzawa & Yoshizawa (2019). Their detailed theory and formulations have been described in those papers. In this section, the method and procedure are briefly reviewed through their application to synthetic seismograms. More details of the formulations are given in Appendix A. Throughout this study, we have used a program package, MINEOS v1.0.2 (Masters et al., 2011), for calculating normal-mode based synthetic seismograms. MINEOS enables us to compute synthetics through the summation of normal modes for a non-rotating spherical Earth.

## 2.2 Methods of Linear-array Analysis

### 2.2.1 Multi-mode surface-wave dispersion measurements

Our 1-D-array-based analysis has been designed on a kind of slant-stacking techniques with group speed window originally developed by Nolet (1975, 1976). Here, we explain this analysis with synthetic waveforms in an ideal setting. We consider a linear array of seismic stations of the total 4000-

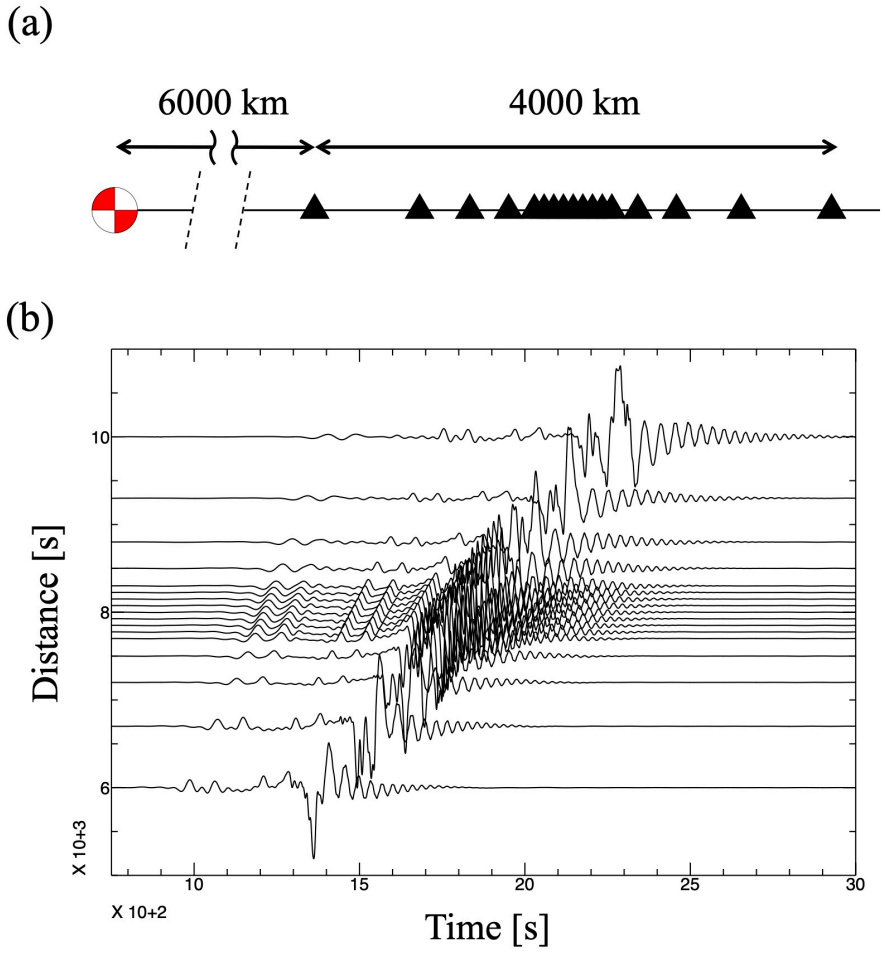



Figure 2.1: (a) A linear array with an assumed source mechanism of a strike-slip fault. Black triangles indicate locations of seismic stations. (b) A record section of synthetic seismograms (transverse component) for all stations in (a), including the fundamental-mode and 1st-8th overtone Love waves calculated for no-oceanic PREM.

km span with a given focal mechanism as shown in Fig. 2.1a. Synthetic seismograms of the transverse component for all the stations are shown in Fig. 2.1b. The background seismic structure under the array is supposed to be uniform. We employ the no-oceanic PREM (Preliminary Reference Earth Model) (Dziewoński & Anderson, 1981) as our reference model. A strike-slip source is located 6000 km away from the array at 200 km depth, which excites both fundamental- and higher-mode Love waves.

At first, time windows of a given group speed are applied to seismograms of all the stations to extract seismic signals that propagate with this speed. Next, a beam spectrum is obtained by slant-stacking Fourier spectra of the windowed seismograms, assuming a constant phase speed across an array. Here, they are stacked with respect to the centroid of an array (i.e., the reference position) by shifting phases with the given phase speed. This stacking process enhances coherent signals and cancels out incoherent ones as well as random noises effectively.

The beam spectra can be expressed as a function of group speed, $U$, phase speed, $c$, and angular frequency $\omega$. As a result, we make a spectrogram in the $c$-$U$ domain at each $\omega$. An example of the beam power spectra at $\omega = 2\pi/30$ (or 30 s period) is shown in Fig. 2.2a, which is derived from the synthetic waveforms of Fig. 2.1b.

The black triangles in the figure indicate the true spectral peaks calculated from the normal modes for the reference model (i.e., no-oceanic PREM). We can see that the triangles are collocated with the true spectral peaks, but many "spurious" peaks exist along the "phase-speed" axis. This is mainly because the beam spectrum represents the weighted average at centroid locations multiplied by the array response function, $H(k) = \frac{1}{N}\sum_{j=1}^{N} \exp\left[ik\left(x_j - \bar{x}\right)\right]$, as shown in Fig. 2.3, which is determined only by the array configuration. The spurious peaks in Fig. 2.2a are attributed to

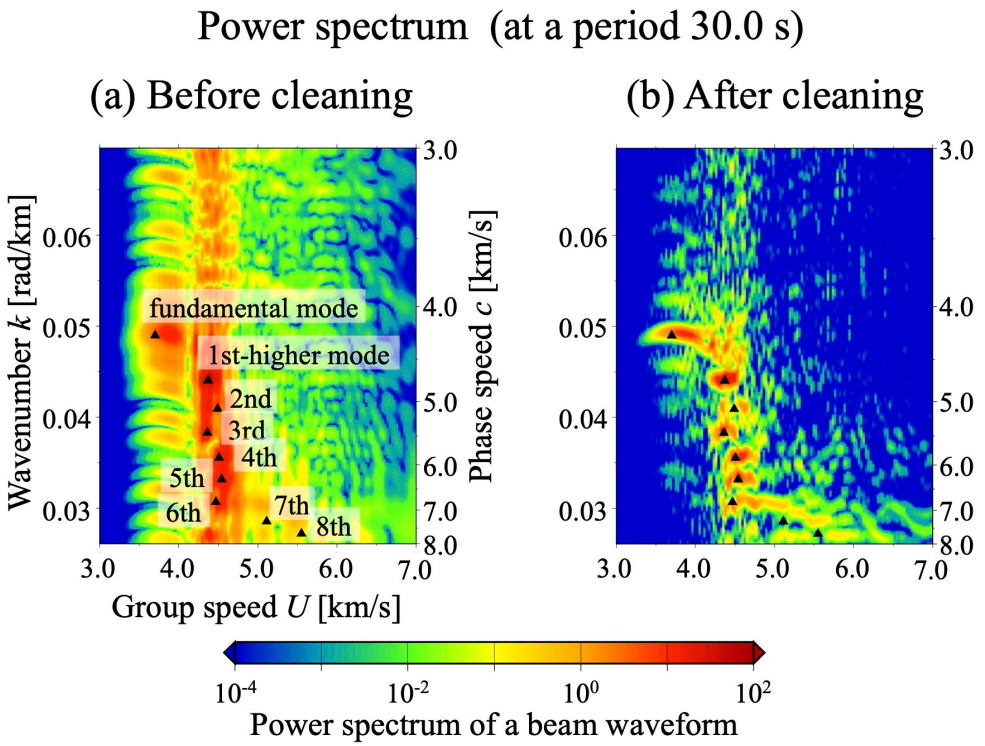



Figure 2.2: Power spectra at period $T = 30.0$ s in the $c$–$U$ domain, calculated from the synthetic waveforms shown in Fig. 2.1(b). (a) Before and (b) after the cleaning process of spurious peaks due to the sidelobes of array response. Black triangles indicate the true spectral peaks for no-oceanic PREM.

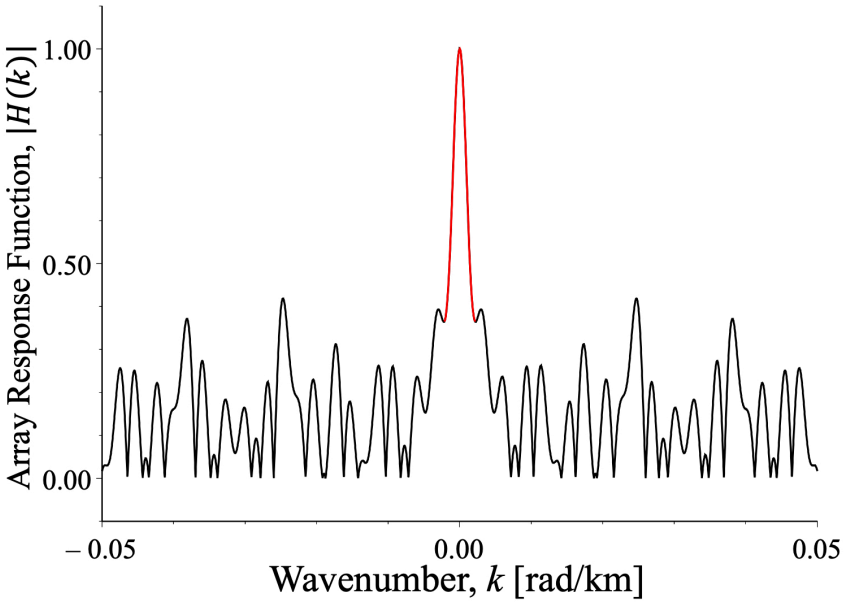



Figure 2.3: An example of the array response function for the linear array in Fig. 2.1b. The red line indicates its mainlobe.

the sidelobes in Fig. 2.3.

We can eliminate these spurious peaks and enhance the true peaks through an iterative cleaning process based on the array response function described by Nolet (1975, 1976). This process corresponds to a narrow wavenumber filtering applied to the array response function around its main lobe. Figure 2.2b shows the spectrogram after the cleaning process. Only the conspicuous peaks corresponding to each mode remain, implying that the process works well.

Next, the beam spectrogram in the $c$-$U$ domain at each frequency $\omega$ is projected in the $c$-$T$ domain (where $T$ is the period), which eventually provides us with multi-mode dispersion curves as continuous spectral peaks. Figure 2.4b shows the normalized multi-mode dispersion curves extracted from the set of seismograms in Figure 2.1b. Black dashed lines are the theoretical curves calculated from the reference model. Spectral peaks in

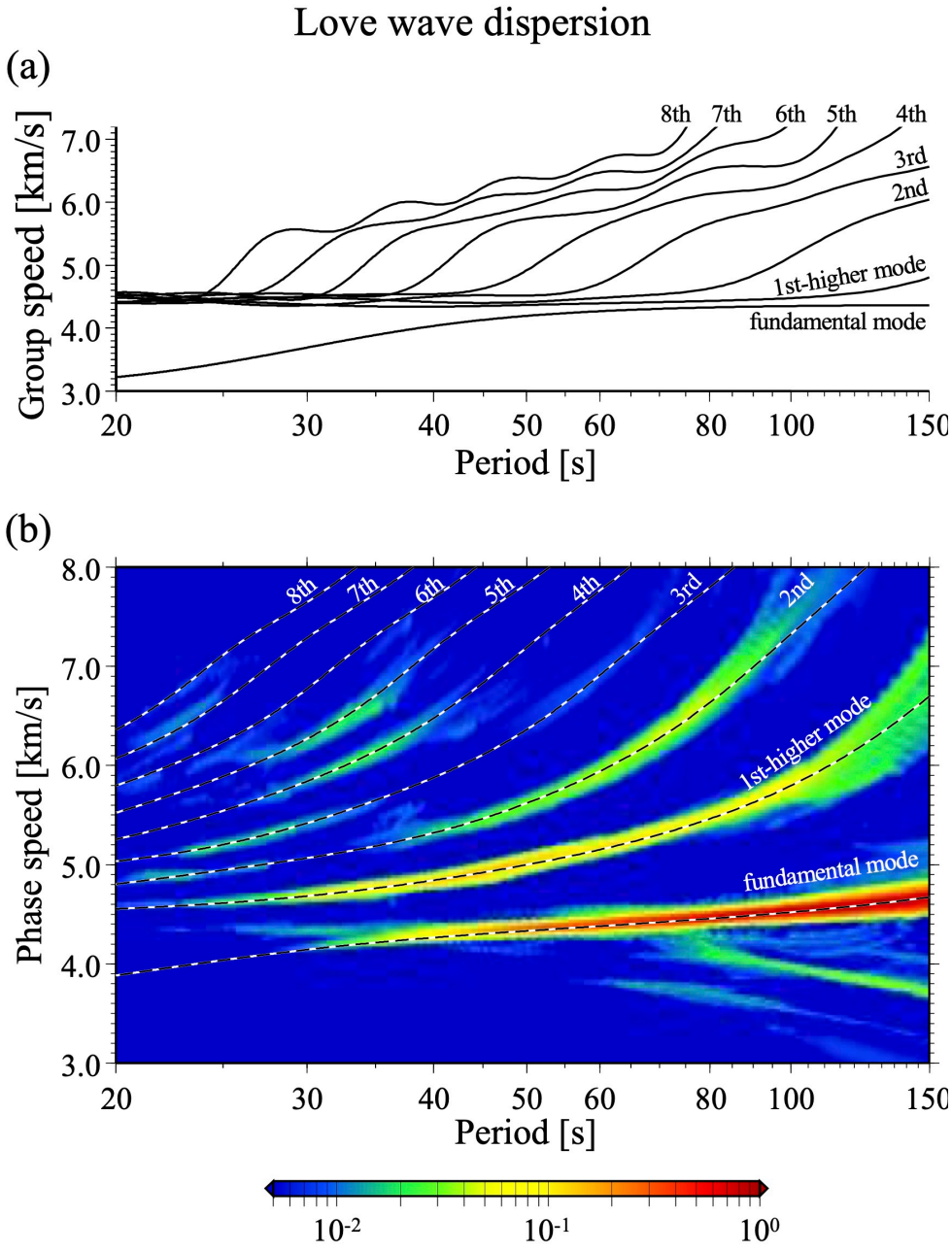



Figure 2.4: (a) Love wave group speed curves for the fundamental mode and 1st–8th higher modes calculated from no-oceanic PREM. (b) Estimated multi-mode phase speed curves (power spectrogram) in the $c$–$T$ domain. Black and white dashed lines are the theoretical dispersion curves of each mode from no-oceanic PREM.

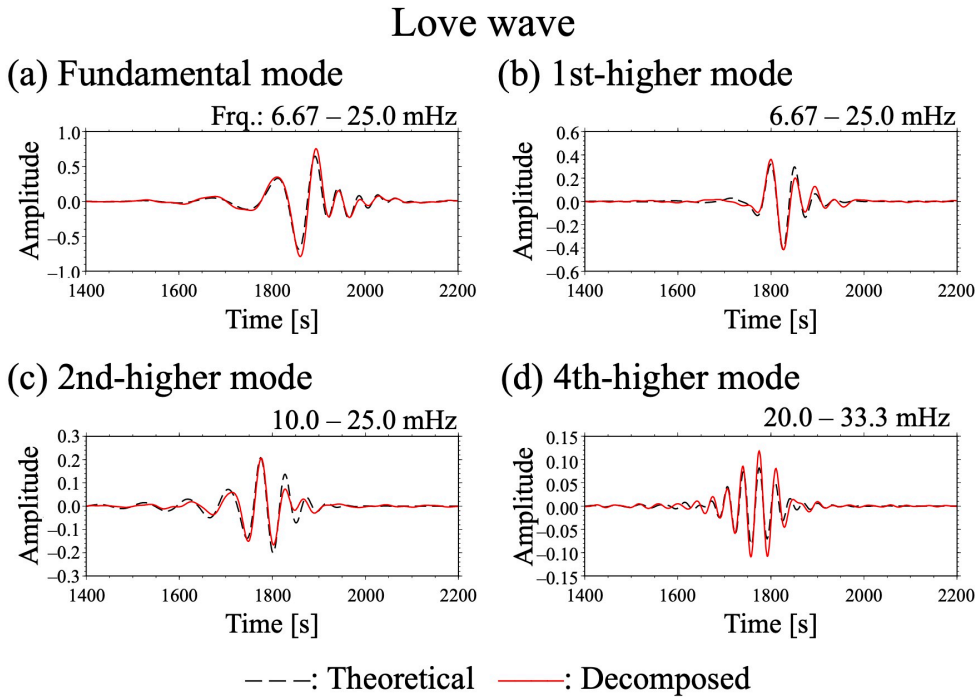



Figure 2.5: Comparison of theoretical (black dashed line) and decomposed (red solid line) mode-branch waveforms of Love waves: (a) fundamental mode, (b) 1st higher mode, (c) 2nd higher mode and (d) 4th higher mode.

Figure 2.4b agree well with the reference dispersion curves, and lower-order modes are mutually separated well even in a short period range ($T < 50$ sec) where group speeds of different modes overlap each other (Fig. 2.4a).

It should be noted that when we obtain the spectrum in Figure 2.4b, we employ a narrow Gaussian filter with a standard deviation of 1.0 % of wavenumber for the fundamental-mode Love wave. The subjective selection of this filter width is not unique, but it is practically useful to improve the resolution of the dispersion spectrogram.

### 2.2.2 Decomposition into modal waveforms

Our multi-mode dispersion spectrogram such as Fig. 2.4b can be used for extracting modal waveforms for several lower modes. An individual modal

waveform should include only a single mode, which may lead to more precise dispersion measurements through the subsequent interstation analysis or array-based analysis, minimizing the contaminations of neighboring mode branches. In this study, we used a method based on the Linear Radon Transform (Luo et al., 2015) for the decomposition into the set of single-mode waveforms. The details of the LRT formulation have been described by Luo et al. (2015) and Matsuzawa (2018). A brief summary of the method is also given in Appendix A. Using LRT, we can perform the linear transform from the spectra in the "phase-speed"–"period" domain to that in the "distance"–"period" domain. The LRT can therefore reconstruct single-mode waveforms from a single-mode dispersion spectrogram extracted from the array-based dispersion analysis explained in the previous section.

The single-mode waveforms of Love waves obtained from the mode separation are shown in Fig. 2.5. They correspond to the waveforms derived from the spectrogram shown in Fig. 2.4b at the centroid location of the linear array in Fig. 2.1. Since several filters have been applied during multiple steps for extracting the $c$–$T$ spectra, absolute amplitudes of each mode cannot be fully recovered. The waveform amplitudes in Fig. 2.5 are normalized by the maximum amplitude of the fundamental-mode Love wave. Nevertheless, we can see clear relative differences in amplitude among mode-branch seismograms and their phases for the first five modes. For the fundamental and the first higher modes, main wavetrains with the largest amplitude have been retrieved almost perfectly. While major phases of these seismograms with long periods match well, the recovery of relative amplitudes in a shorter period range becomes degraded, mainly due to the uncertainty in spectral amplitudes of the phase–dispersion spectrogram. For the same reason, the accuracy of mode-branch waveforms for other higher modes tends to be limited in comparison with that for the fundamental mode. Still, the major

features of mode-branch seismograms can be recovered well, enabling us to utilize such modal seismograms in a framework of classical dispersion analysis with a single-plane wave approximation, such as the inter-station method and/or two-dimensional array-based method.

Matsuzawa & Yoshizawa (2019) have shown that the decomposed modal waveform with the LRT can be used to improve the inter-station phase speed measurements of the fundamental-mode Love waves. Our synthetic results suggest that the uncertainty in measurements can be reduced dramatically to less than 1.5 % by the decomposed fundamental-mode Love waves, compared to those derived from the waveforms without decomposition, particularly for shorter interstation distances less than 2000 km. This is mainly because we can reduce the well-known higher-mode interference on the fundamental mode Love waves. Furthermore, our results suggest that the higher-mode phase speed can be measured by the inter-station analysis using the decomposed modal waveforms.

### 2.2.3 Numerical experiments for the effect of array length

It should be noted that resulting $c$-$T$ power spectrograms such as Fig. 2.4 are affected directly by the excitation level of each mode and the array size, as indicated by Nolet & Panza (1976). For stable measurements of multimode phase speeds with the present array-based method, we need a long-range linear array to isolate the effects of several overlapping modes that propagate with different or similar group speeds. If the array scale is sufficiently greater than the wavelength of surface waves, the multimode phase dispersion can be precisely estimated in a wider period range.

Fig. 2.6 shows the results of estimated multi-mode dispersion spectrograms for Love waves in the $c$–$T$ domain using the linear array method with different array lengths: (a) 1500 km, (b) 2000 km, (c) 2500 km and (d) 3000

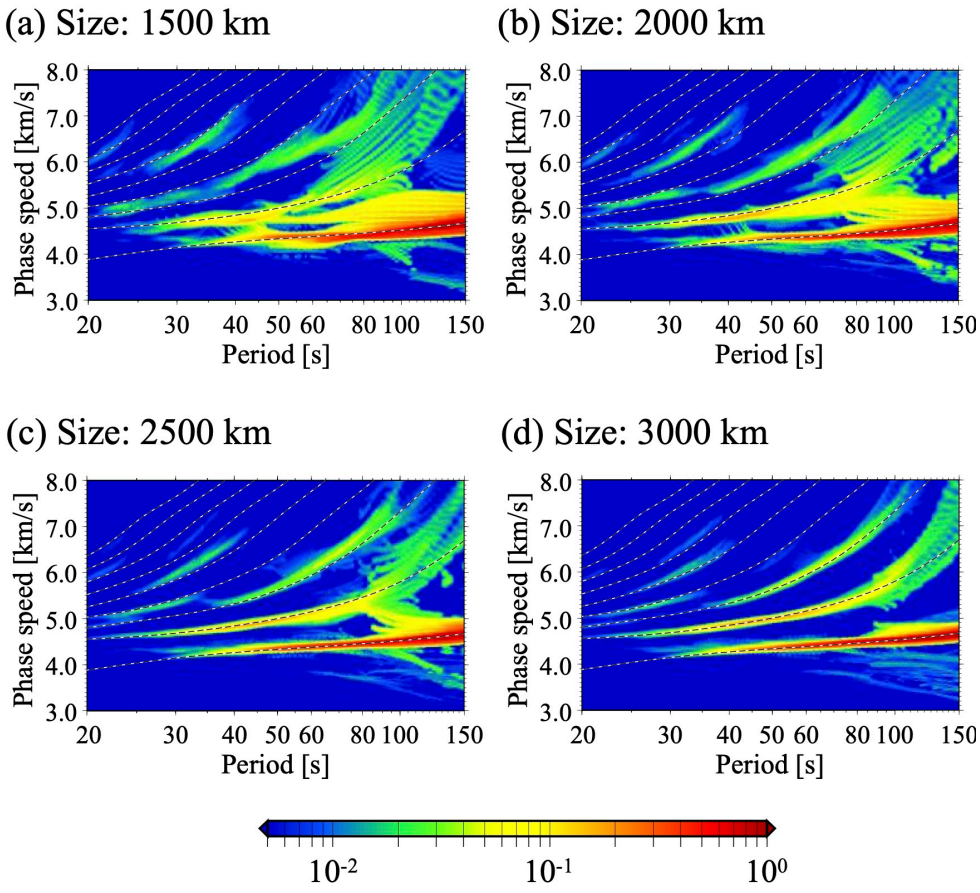



Figure 2.6: Results of synthetic experiments for extracting $c$–$T$ spectrograms with different array lengths; (a) 1500 km, (b) 2000 km, (c) 2500 km and (d) 3000 km. The black and white dashed lines are the theoretical dispersion curves for no-oceanic PREM.

km. Seismic stations are assumed to be located at every 100 km, and the centroid location of the array is set to be at 8000 km from the epicenter. Synthetic seismograms of the transverse component at each station are calculated for no-oceanic, isotropic PREM using the focal mechanism shown in Fig. 2.1a with the source depth of 200 km.

Even wit relatively short-range arrays with 1500 km or 2000 km (Figs 2.6(a and b)), we can see clear spectral peaks of the fundamental mode, but their spectrograms are contaminated by spurious striped spectra that make it difficult to identify higher mode dispersion curves precisely. Although the spectral peaks of the first-higher mode can be identified in the period range of 30–45 s, they appear to be mixed up with the fundamental mode. We may concluded that, a short array relative to the wavelength of higher modes, the enhancement of higher mode signals through the slant-stacking process does not work properly.

With an array over 2500 km in length (Fig. 2.6c), we can extract multi-mode spectrogram with distinct spectral peaks of the fundamental, first and second higher modes. There still remain some spurious peaks, but they are almost eliminated if an array span exceeds 3000 km (Fig. 2.6d), in which the phase dispersion of the first six modes can be retrieved fairly well. The resolution in the $c$–$T$ domain is primarily controlled by the mainlobe width of the array response function, which is used as a basis for the wavenumber filtering. The overall width of the mainlobe is inversely proportional to the array length. The present synthetic experiments suggest that a linear array longer than 2500 km is necessary to properly extract multi-mode dispersion curves in our target period orange (20-150 s) through the isolation of the spectral peaks of several higher modes.

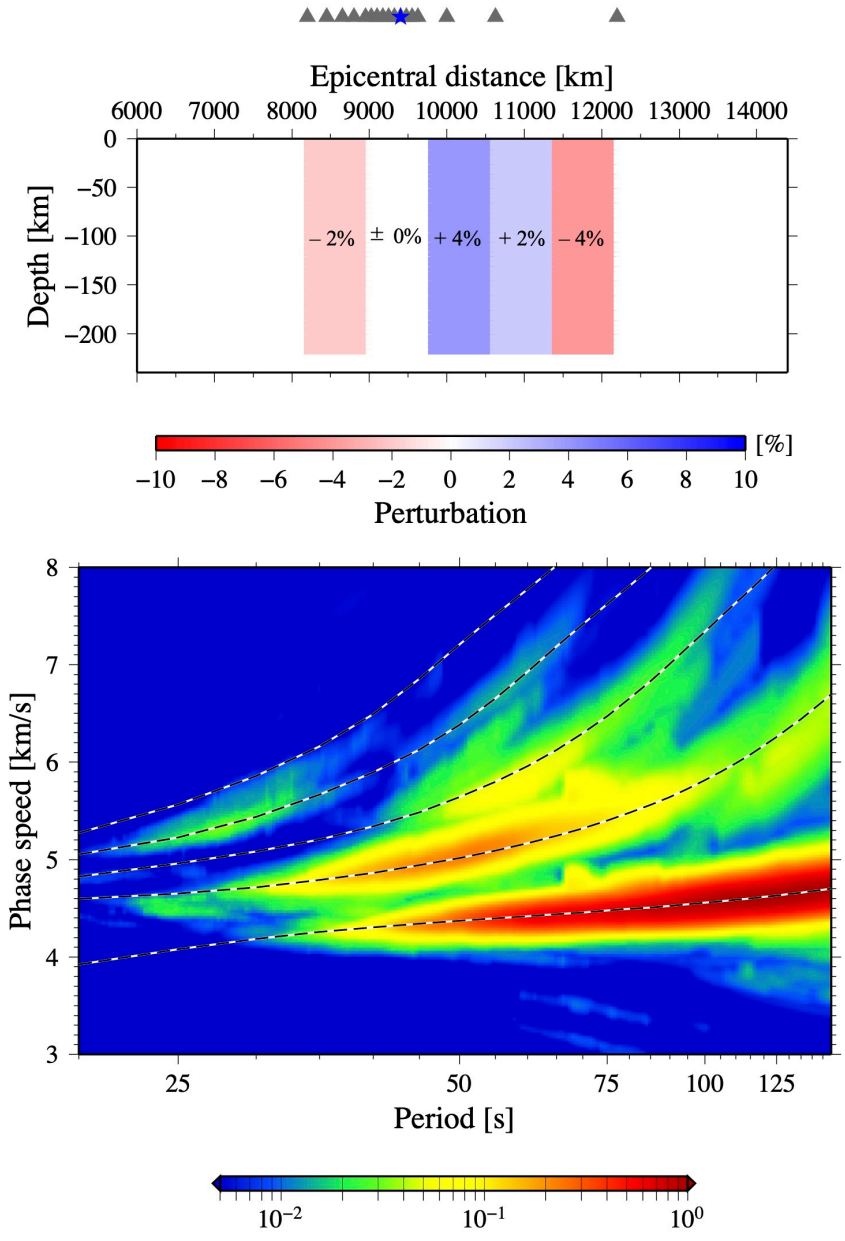



Figure 2.7: (Top) The seismic structure and the location of array. (Bottom) The power spectrogram in the $c$–$T$ domain. The black and white dashed lines are the weighted-average dispersion curves. The weight functions are shown in Fig. 2.10. The centroid of the array is 9400 km away from the source.

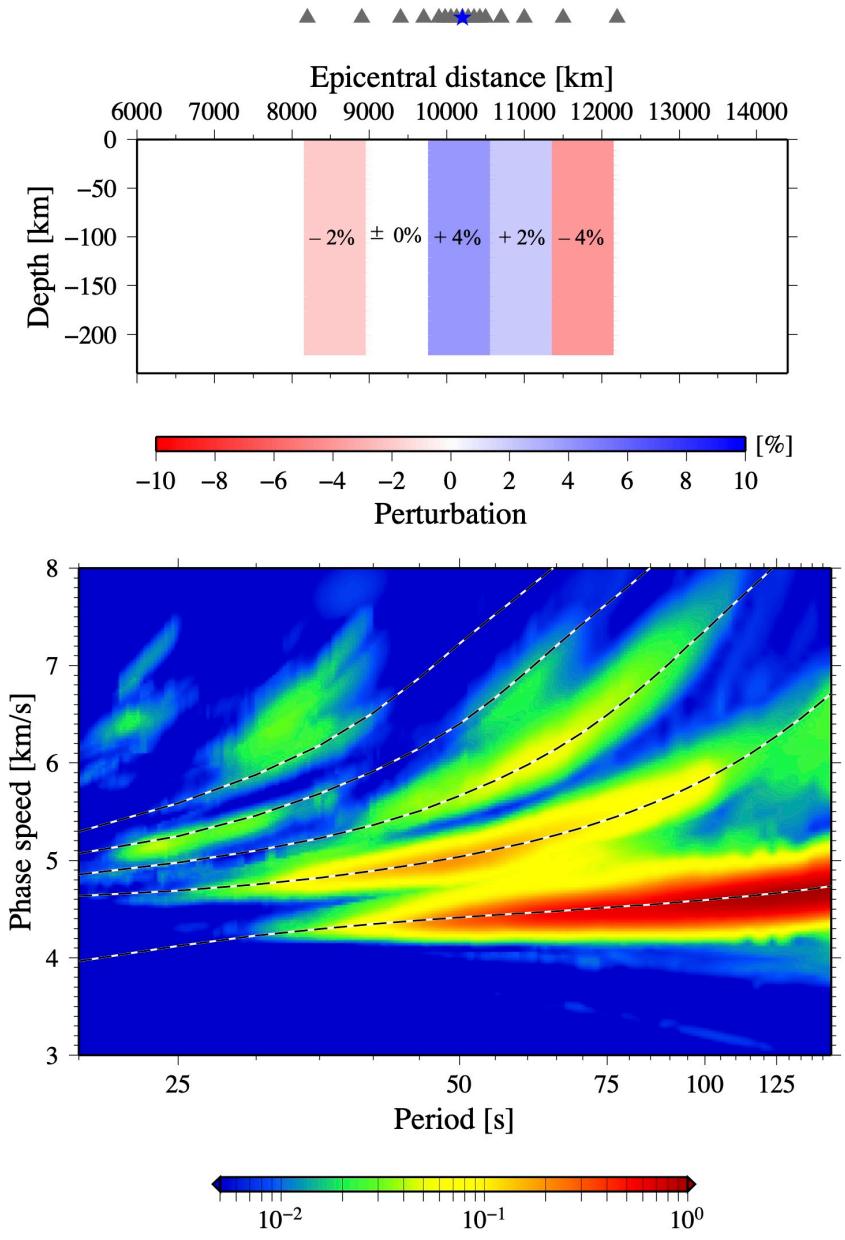



Figure 2.8: Same to Figure 2.7, but the centroid of the array is 10200 km away from the source.

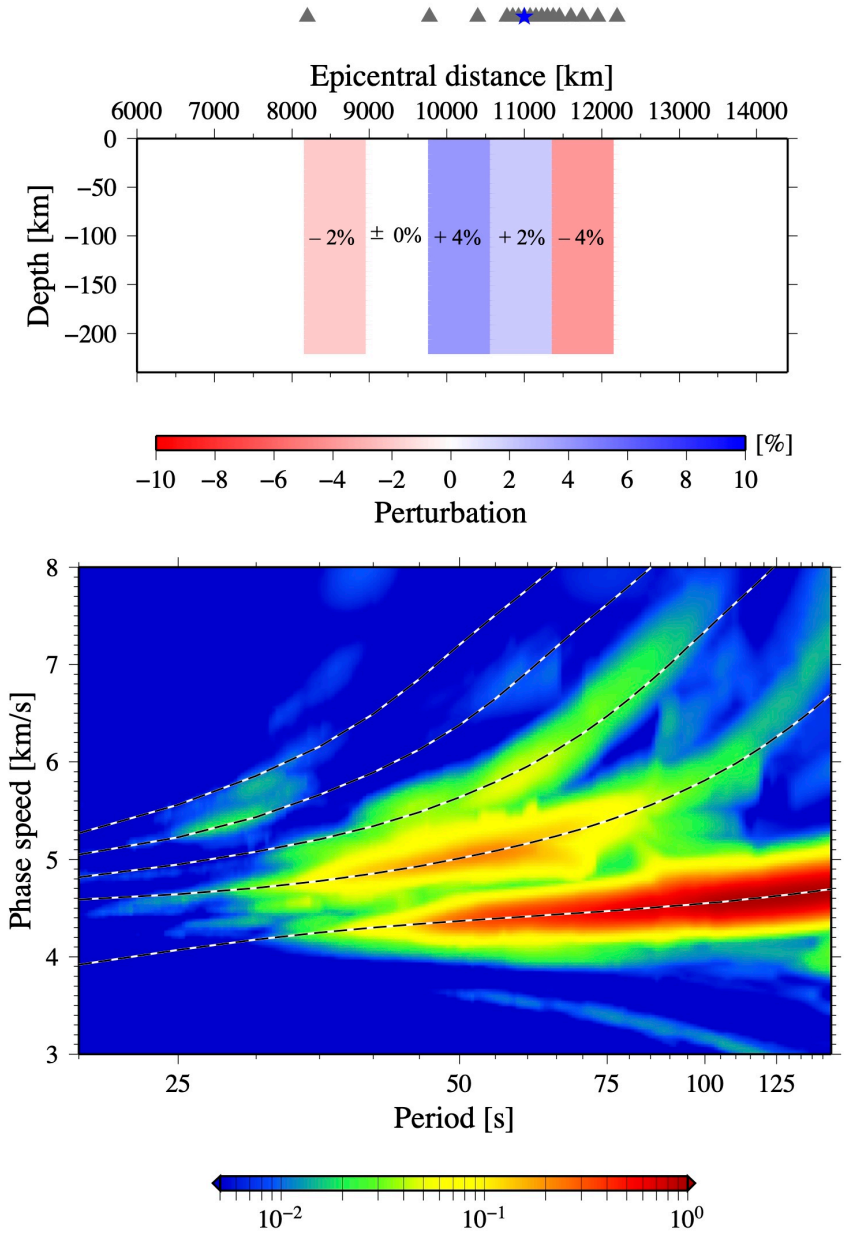



Figure 2.9: Same to Figure 2.7, but the centroid of the array is 11100 km away from the source.

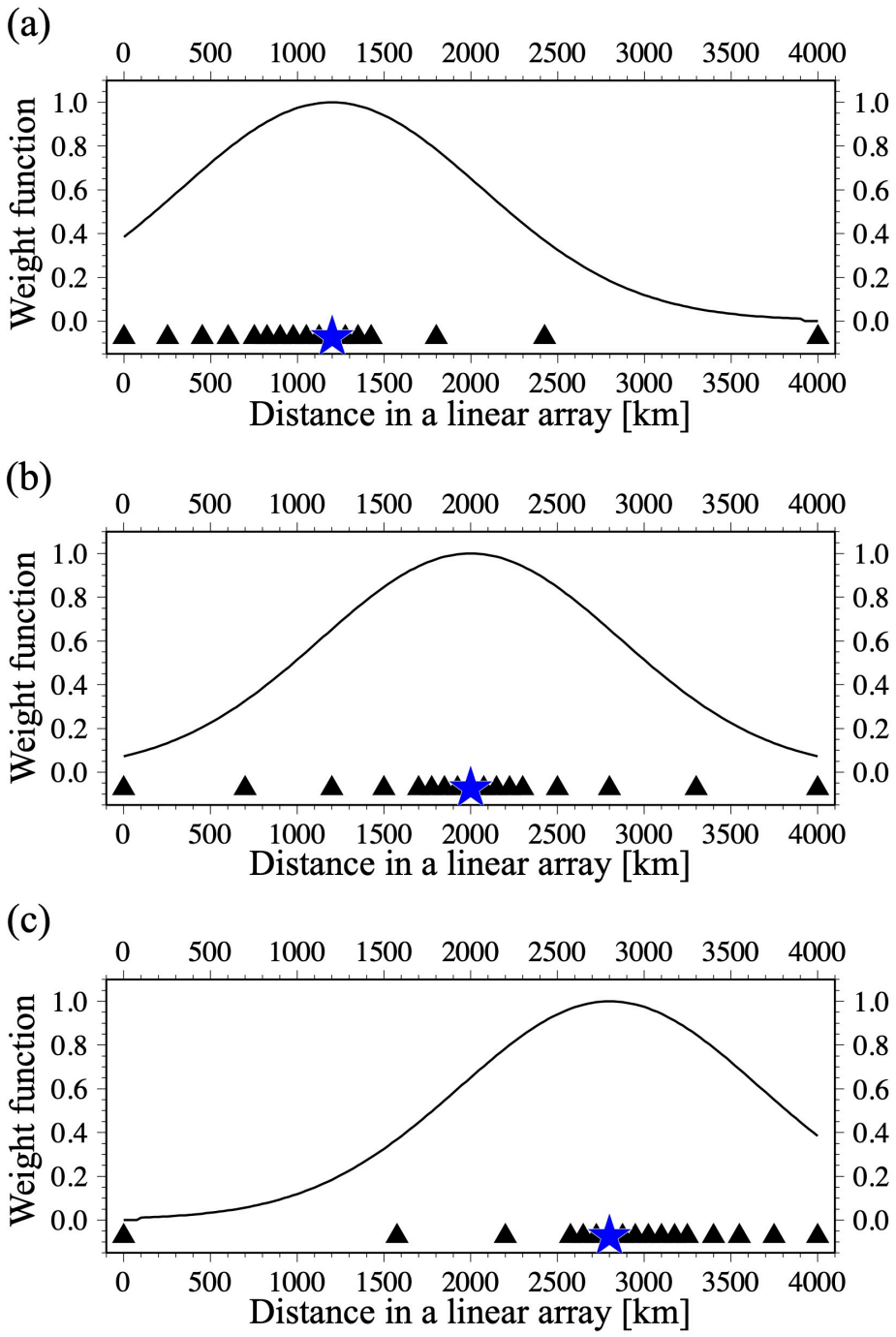



Figure 2.10: The weight functions associated with each linear array shown in the top panel of Figs. 2.7–2.9.

### 2.2.4 Numerical experiments for heterogeneous models

Similar to the classical beamforming method, the method explained in the previous section assumed a laterally homogeneous structure under the given long-range array. However, it is obviously not practical in the real Earth. Now we verify how well our method works for laterally heterogeneous structures.

Examples of synthetic experiments with a laterally heterogeneous structure beneath the array are shown in Figs. 2.7–2.9. The top panel of each figure shows the employed seismic structure with a given array location. The S wave speeds in the top 220 km are perturbed from $-4\%$ to $+4\%$ with respect to the reference model (no-oceanic PREM) in the target area beneath the array; $-2\%$ between 8200 and 9000 km, $+4\%$ between 9800 km and 10600 km, $+2\%$ between 10600 km and 11400 km, and $-4\%$ between 11400 km and 12200 km in epicentral distances. The average structure is the reference model (no oceanic PREM). While all the 4000-km arrays in the top panel of Figs. 2.7–2.9 cover the same heterogeneous region, their centroid locations (blue star) are different: 9400 km in Fig. 2.7, 10200 km in Fig. 2.8 and 11000 km in Fig. 2.9, away from the source, respectively.

The bottom panels in Figs. 2.7–2.9 show the $c$–$T$ spectrograms extracted by using our method. We can see dominant spectral peaks corresponding to the reference dispersion curves represented by black and white dashed lines. In the extraction of these curves from the heterogeneous structure in the top panel, we employ weight functions shown in Fig. 2.10. Each function is derived from the array response function associated with the array. The array response function is determined only by the station configuration of each array. Each phase speed measurement can be interpreted as the average weighted by its array response function. Therefore, the weight functions shown in Fig. 2.10 are generated by the inverse Fourier transform from the

wavenumber ($k$) domain to the space ($x$) domain based on the main lobe of the array response function used for the cleaning process. The weight functions look like a Gaussian one, and its sensitivity peak coincides with the centroid location of each array. These results suggest that our 1-D-array method works well for measuring multi-mode phase speed dispersions, even in the case of heterogeneous structures beneath the array. The final measurement reflects the averaged phase speed within the entire array around its centroid location.

## 2.3 Application to Observed Data in USArray

In this section, the linear array-based method described in the previous sections is applied to the actual seismograms recorded at broad-band stations in the United States.

### 2.3.1 Multi-mode dispersion measurements

We show three selected examples of the $c$–$T$ power spectrograms of dispersion curves in a period range of 20–150 s derived from our array-based method: one for multi-mode Love waves and two for multi-mode Rayleigh waves.

The configuration of the employed array for Love-wave dispersion spectrograms is displayed in Fig. 2.11. We used an event in Equador on August 12 (11:54 UT), 2010, with the moment magnitude 7.1 at a depth of 197.8 km. The azimuth from the source to the array is 331°. The array length is about 3300 km with the epicentral distance of its centroid at 4975 km. The array, which crosses from south-east to north-west in the North American continent, comprises 33 stations mostly in the western and central U.S. Its centroid coincides with a cratonic region of fast seismic speed. The orignal record section of the transverse component in Fig. 2.12 shows the propagation and dispersion of coherent signals including the fundamental- and

higher-mode Love waves along this long-range array.

Fig. 2.13 shows the $c$-$T$ dispersion spectrum of the multi-mode Love waves obtained by applying our 1-D-array-based analysis to the seismograms of Fig. 2.12. We can identify several continuous spectral peaks corresponding to the dispersion curves of fundamental and first four higher modes in a wide period range over 25 s. This result is due to the sufficiently long array length compared to the wavelength of higher modes, which are well excited by the deep event (about 200 km). The measured phase speeds are mostly close to the reference curves indicated by the dashed lines computed from global 3-D crust and upper mantle models; that is, CRUST1.0 (Laske et al., 2013) and S362ANI+M (Moulik & Ekström, 2014; Trabant et al., 2012). In a period range shorter than 50 s, the measured phase speeds are faster than the reference ones by $0.1 - 0.3$ km/s, reflecting localized structure around the centroid. We next extract modal waveforms decomposed using the $c$–$T$ spectrogram by applying the LRT. Fig. 2.14 shows the modal waveforms of the fundamental and first two higher-mode Love waves at the centroid of the array, as well as the observed seismograms recorded at T27A (TA), which is the nearest station to the centroid. These waveforms are normalized by the maximum amplitude of the fundamental mode. Even for the present real data, their phases and relative amplitudes can be retrieved successfully, indicating the utility of the LRT.

For Rayleigh wave dispersion analysis, we employ two linear arrays, "Azimuth45" and "Azimuth50" shown in Fig. 2.15. In this analysis, we used an event that occurred near Tonga Islands on October 22nd (12:56 UT), 2008, with the moment magnitude 6.4 at a depth of 224.0 km. These two arrays are about 2800 km long with the centroid of the epicentral distance of 9300–9400 km. The number of stations is 36 in both cases.

The $c$–$T$ spectrograms derived from the seismograms in Fig. 2.16 are

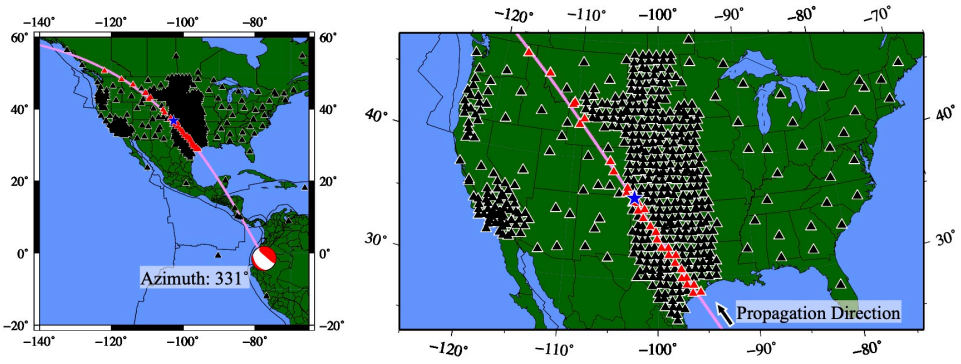



Figure 2.11: Locations of the source and linear arrays; the great-circle path (azimuth: 331°) from the source (pink line), seismic stations (black and red triangles; red triangles indicate selected stations for the linear array) and the centroid of the array (blue star). The employed event occurred on August 12th, 2010. (Left) Overview (Right) Zoom-in view of the U.S. The source location and the focal mechanism are taken from the Global CMT catalog. (Dziewoński et al., 1981; Ekström et al., 2012)

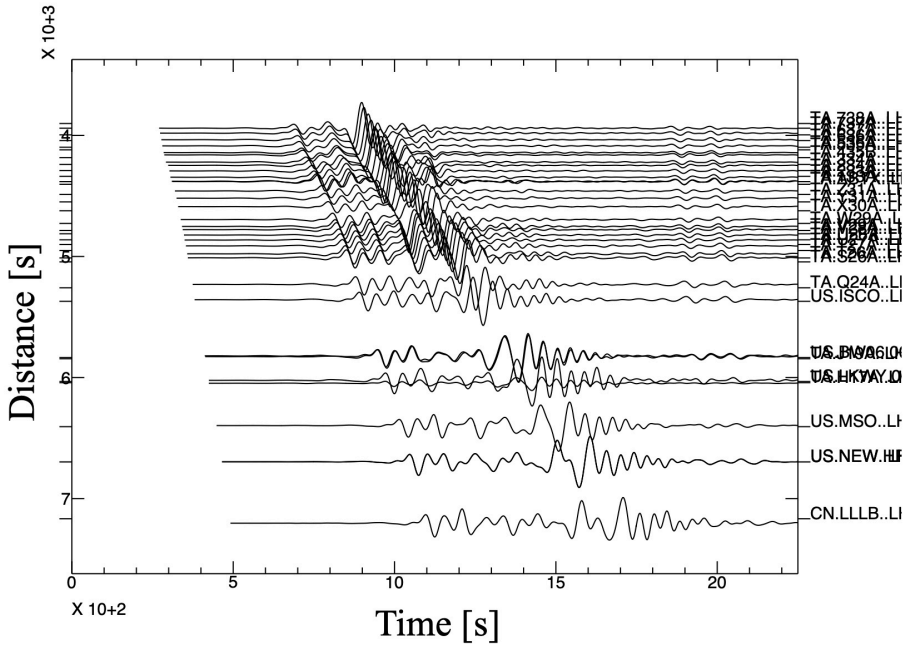



Figure 2.12: Transverse-component seismograms observed at stations along a great-circle path in direction of azimuth 331° indicated by red triangles in Fig. 2.11. A wide bandpass filter (6.67–25 mHz) was applied.

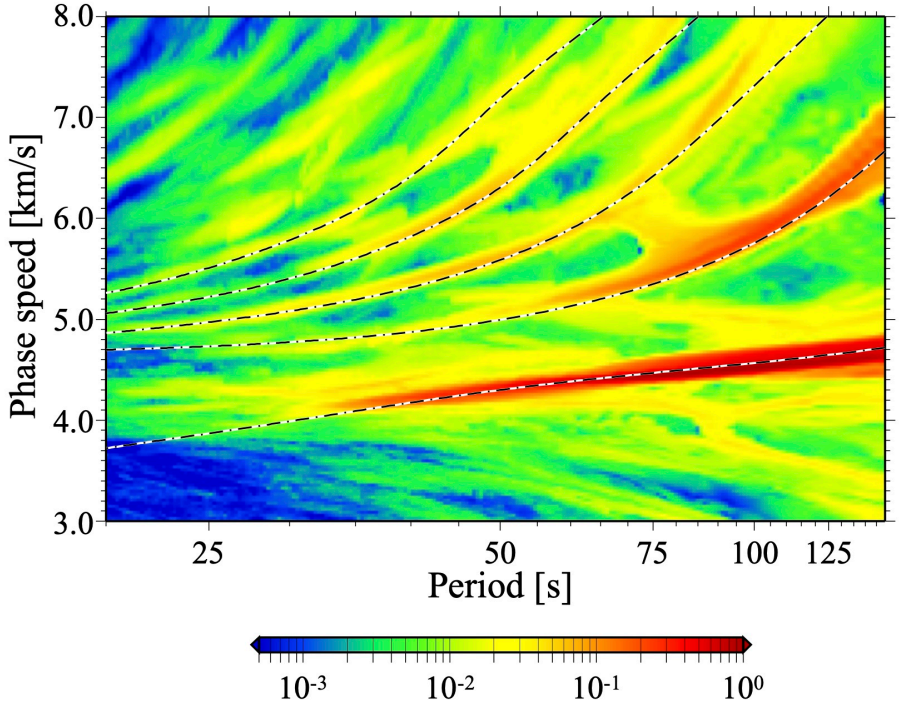



Figure 2.13: An example power spectrogram of the multi-mode Love wave dispersion in the $c$–$T$ domain derived from seismograms shown in Fig 2.12. The dashed lines represent the reference dispersion curves calculated from global 3-D model.

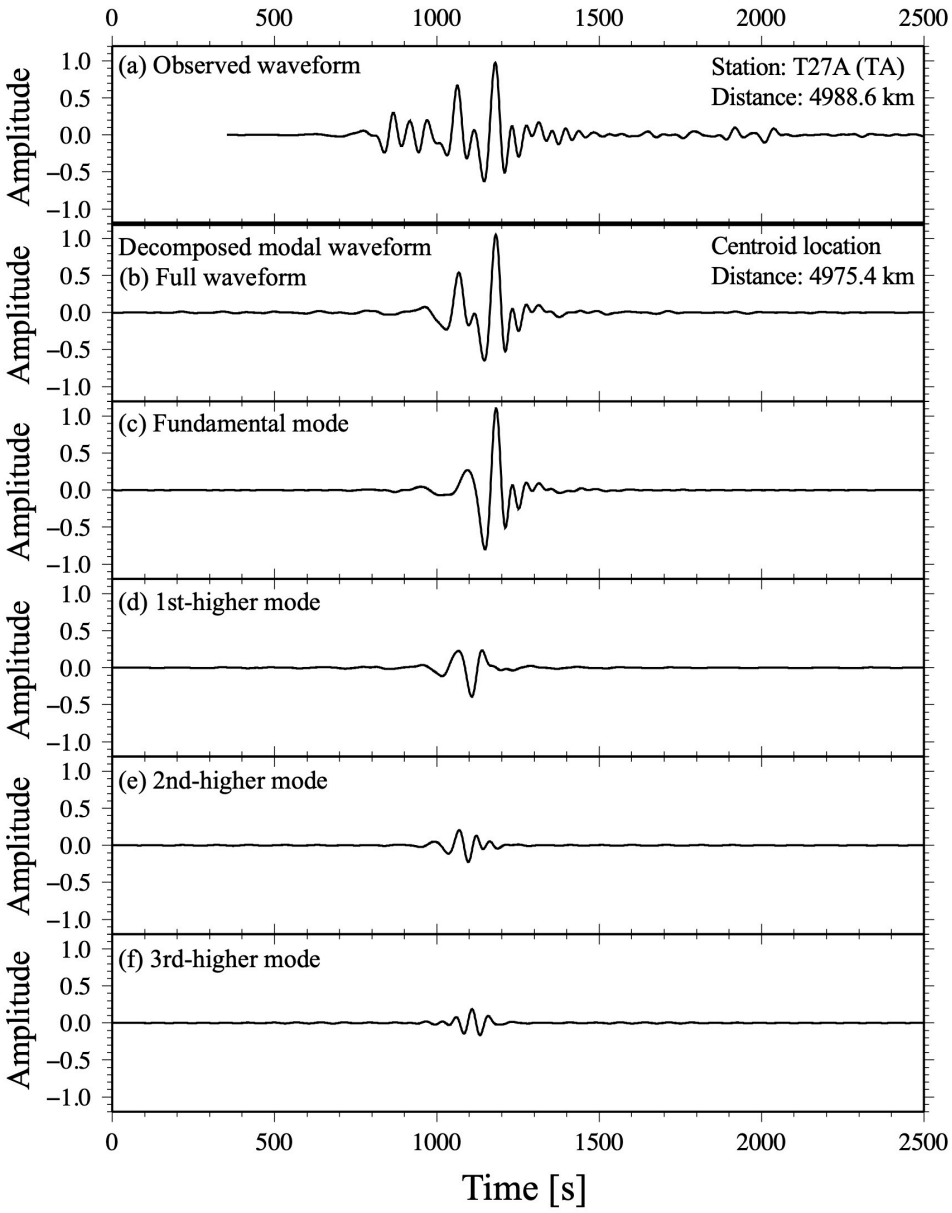



Figure 2.14: Comparison of (a) observed full waveforms at TA.T27A station (4988.6 km from the source) and (b-f) decomposed Love wave modes. (b) the sum of the first four modes, (c) the fundamental-mode, (d) 1st-higher mode (e) 2nd-higher mode and (f) 3rd-highwe mode at the centroid (4975.4 km from the source) of the linear array.

shown in Fig. 2.17. Similar to the Love wave case, we can see several spectral peaks, especially, equivalent to the fundamental and 1st-higher mode dispersion in a longer period than 60 s.

While the conspicuous peaks in Array45 are consistent with reference curves extracted from the global 3-D model, those in Array50 are faster than the reference ones by 2–3%. This may reflect the local-scale fast anomalies near the centroid slightly shifted to the east.

### 2.3.2 2-D mini-array analysis with the decomposed modal waveforms

In this section, the decomposed mode-branch waveforms at centroid locations of linear arrays are applied to secondary two-dimensional array analysis using the same data set from the Tonga Islands earthquake as in the previous section. Here we briefly explain the procedures for the two-dimensional mini-array analysis for mode-branch waveforms.

At first, an original long linear array along a given great circle is selected (e.g. Fig. 2.15), then several subarrays are constructed from the original one; that is, all the sub-arrays share the two end points, with different combinations of station groups inside the original, resulting in sets of slightly shifted centroid locations (e.g., Fig 2.18). The centroid of each sub-array (Fig. 2.19) can be treated as an imaginary station, and the decomposed waveforms at all the centroids are then used as a data set for the 2-D array analysis. Here, we employ the classical 2-D-array analysis based on the beamforming approach to extract average phase speed and propagation direction of a plane wave passing through the 2-D array (e.g., Tanimoto & Prindle, 2011; Alvizuri & Tanimoto, 2011; Maupin, 2011).

Fig. 2.19 shows two examples of circular mini-arrays ('Array-I' and 'Array-II') with a diameter of about 500 km, indicated by orange stars. While Array-I is located around the Array45 and consists of 27 centroids within a

circle with a radius of 250 km centered on (39°N, 112°W), Array-II arround the Array50 of 44 centroids with a radius of 250 km centered on (35°N, 107°W) (see Table 2.1.) The epicentral distance of centroid locationed at these two mini-arrays are over 9000 km away from the source and locate the northwestern and the southeastern edges of the Colorado Plateau.

Figs. 2.20 and 2.21 show the resultant power spectrograms in the 2-D slowness domain ($x$- and $y$-axes represent east-west and north-south directions, respectively) at several periods for the fundamental-mode and 1st-higher-mode Rayleigh waves. The dominant peak (the white star in each spectrogram) indicates the slowness and the back azimuth of an incoming single-plane wave. The obtained phase speeds of the fundamental- and 1st-higher mode are mostly consistent with the global model by Visser et al. (2008), reflecting the influence of large-scale tectonics in the U.S. While the arrival angles of the fundamental-mode are slightly shifted to the north, those of the 1st-higher mode corresponds to great-circle paths.

## 2.4 Discussion

We have proposed a new hybrid approach of array-based analysis for multi-mode surface waves by combining (1) multimode phase speed measurements based on $f$–$k$ analysis with a long-range linear array, and (2) decomposition of a single original seismogram into mode-branch waveforms using the LRT. The present method has been applied to synthetic seismograms for arrays as well as seismograms obtained by USArray.

In its practical application, we need to use a linear array longer than 2000–3000 km for the precise measurement of higher mode phase speeds. We can extract weighted-average dispersion curves within the array, depending on its station configuration. As shown in Fig. 2.15, our dispersion analysis works well even if the background structure rapidly changes in the linear

Table 2.1: Information of mini-arrays of centroids shown in Fig. 2.19.

| | Array location | | | Number of |
|---|---|---|---|---|
| | Latitude | Longitude | Distance | 'centroid' |
| Array-I | 38.7° | −111.3° | 9172 km | 27 |
| Array-II | 35.5° | −106.9° | 9339 km | 44 |

Table 2.2: Rayleigh wave phase speed and arrival angle anomaly for the fundamental and 1st-higher mode. These are obtained from the dominant peak in the power spectrogram shown in Figs. 2.20 and 2.21.

| | Array-I | | | Array-II | | |
|---|---|---|---|---|---|---|
| Period | Phase speed | Arrival angle | Angle anomaly | Phase speed | Arrival angle | Angle anomaly |
| Fundamental mode | | | | | | |
| 50.0 s | 3.98 km/s | 243.5° | 4.4° | 3.86 km/s | 242.0° | −0.3° |
| 60.0 s | 3.89 km/s | 238.5° | −0.6° | 3.96 km/s | 247.0° | 4.7° |
| 80.0 s | 3.98 km/s | 239.0° | −0.1° | 3.97 km/s | 241.0° | −1.3° |
| 100.0 s | 3.99 km/s | 243.0° | 3.9° | 4.02 km/s | 240.0° | −2.3° |
| 1st-higher mode | | | | | | |
| 50.0 s | 4.78 km/s | 242.5° | 3.4° | 4.27 km/s | 240.5° | −1.8° |
| 60.0 s | 5.25 km/s | 240.5° | 1.4° | 5.13 km/s | 243.0° | 0.7° |
| 80.0 s | 5.42 km/s | 241.0° | 1.9° | 5.37 km/s | 242.5° | 0.2° |
| 100.0 s | 5.72 km/s | 238.0° | −1.1° | 5.72 km/s | 242.0° | −0.3° |

array.

These dispersion curves can help us to decompose the original waveform into the mode-branch waveforms at the centroid location by the LRT. Such decomposed waveforms at the centroid can be utilized in the subsequent secondary analyses, such as interstation dispersion measurement and local 2-D array analysis. In the examples of the classical 2-D array analyses shown in Figs. 2.20 and 2.21, both phase speed and arrival angle (the propagation direction) can be measured for each mode, which suggest that the extracted modal seismograms can be used to constrain local phase speeds fairly well.

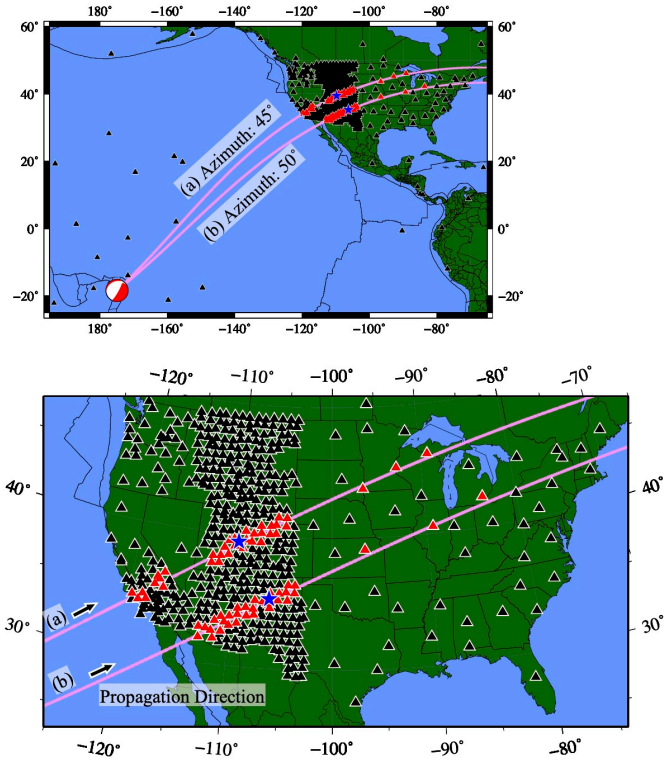



Figure 2.15: Locations of the source and linear arrays along the great-circle path. (a) "Array45" (azimuth: 45°) and (b) "Array50" (50°) from the source (pink line), seismic stations (black and red triangles; red triangles are used in each linear array) and the centroids of the arrays (blue stars). The employed event occurred on October 22nd, 2008. (Top) Overview (Bottom) Zoom-in view of the U.S. The source location and the focal mechanism are taken from the Global CMT catalog. (Dziewoński et al., 1981; Ekström et al., 2012)

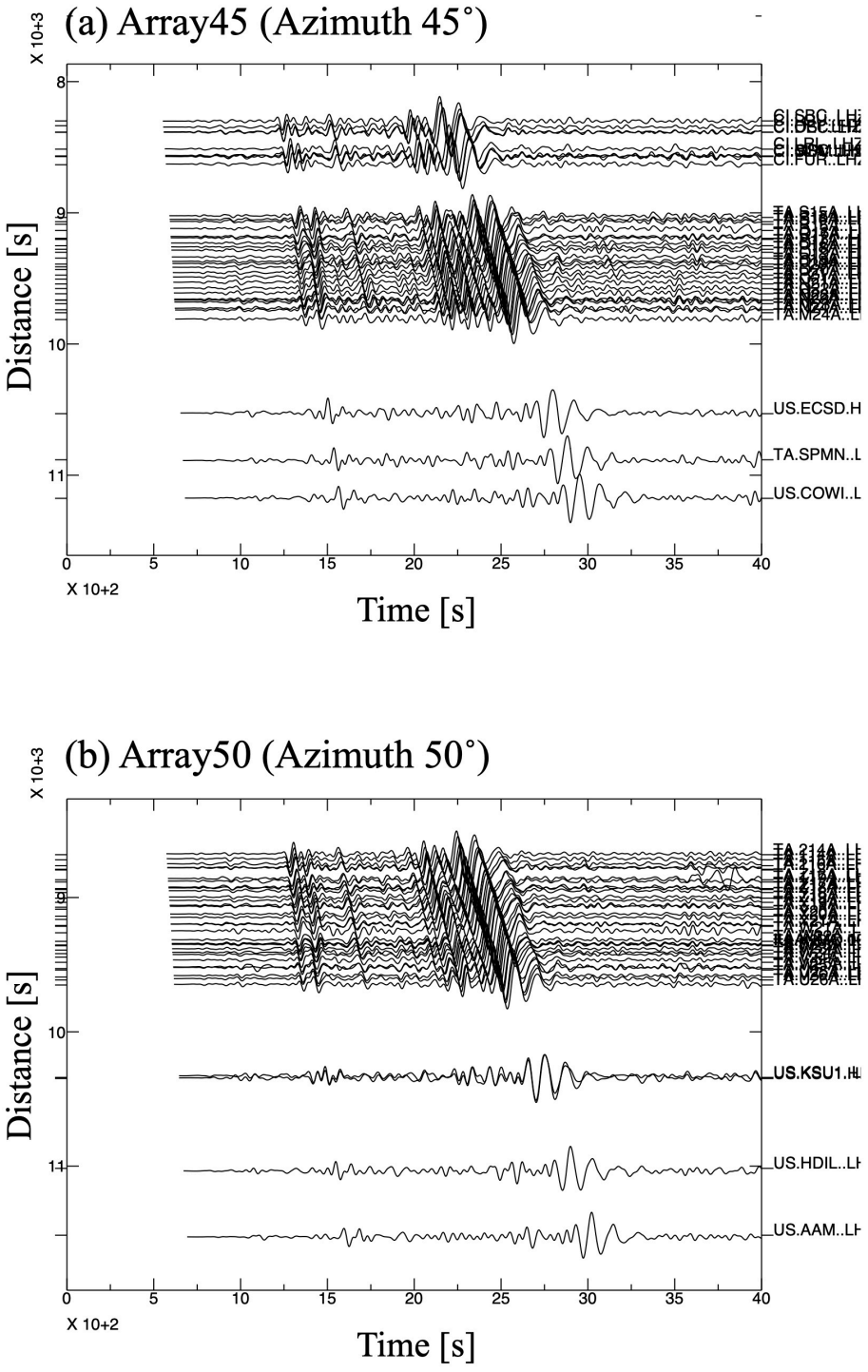



Figure 2.16: Vertical-component seismograms observed at stations of (a) Array45 and (b) Array50, indicated by red triangles in Fig. 2.16. A wide bandpass filter (6.67–25 mHz) was applied.

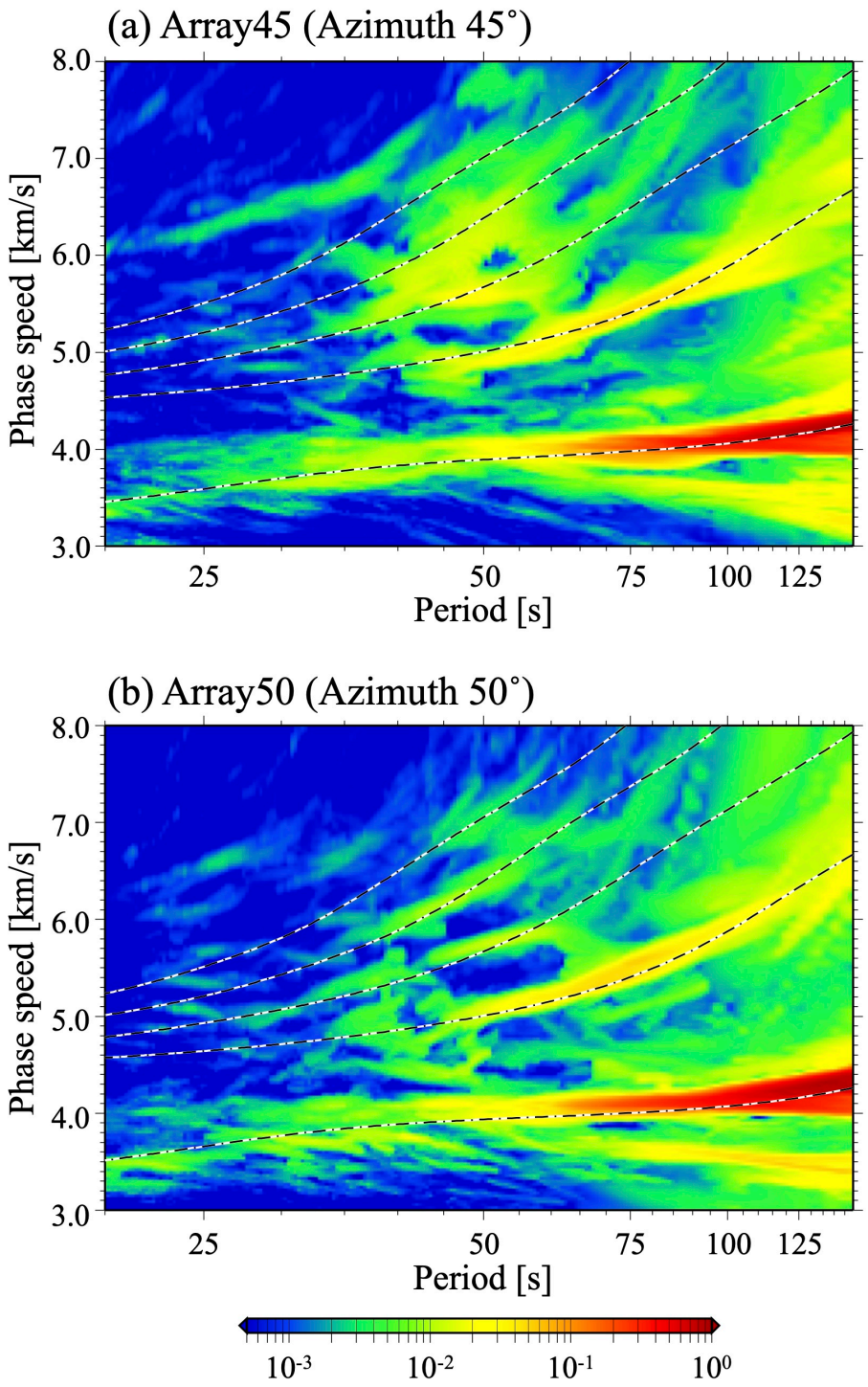



Figure 2.17: Example power spectrograms of the multi-mode Rayleigh wave dispersion in the $c$–$T$ domain derived from seismograms of (a) Array45 and (b) Array50 shown in Fig 2.16. The dashed lines represent the reference dispersion curves calculated from global 3-D model.

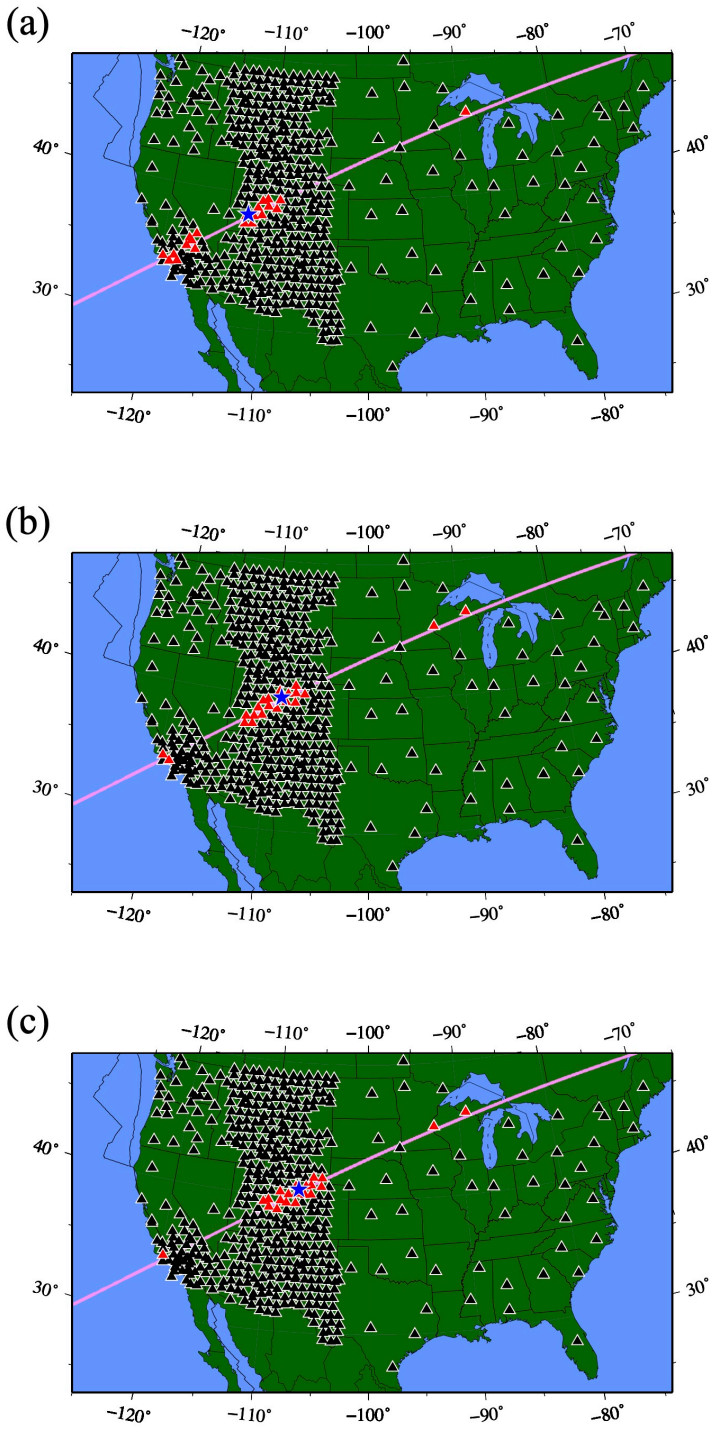



Figure 2.18: Examples of the subarray extracted from Array45. The centroid, which locates (a) 9081.1 km, (b) 9400.4 km and (c) 9563.1 km away from the source, sifted from west to east.

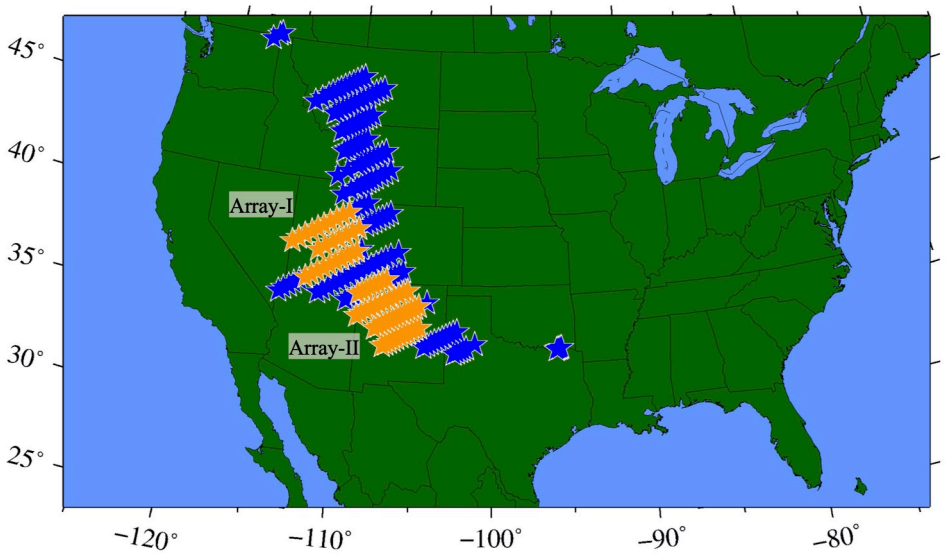



Figure 2.19: Centroid locations of sub-arrays extracted from the stations in Fig. 2.15. The orange stars indicate the centroids used as imaginary stations in the two mini-arrays, "Array-I" and "Array-II". Back azimuth to the source from the center of mini arrays is 239.1° for Array-I and 242.3° for Array-II. Information of these mini-array are summarized in Table 2.1.

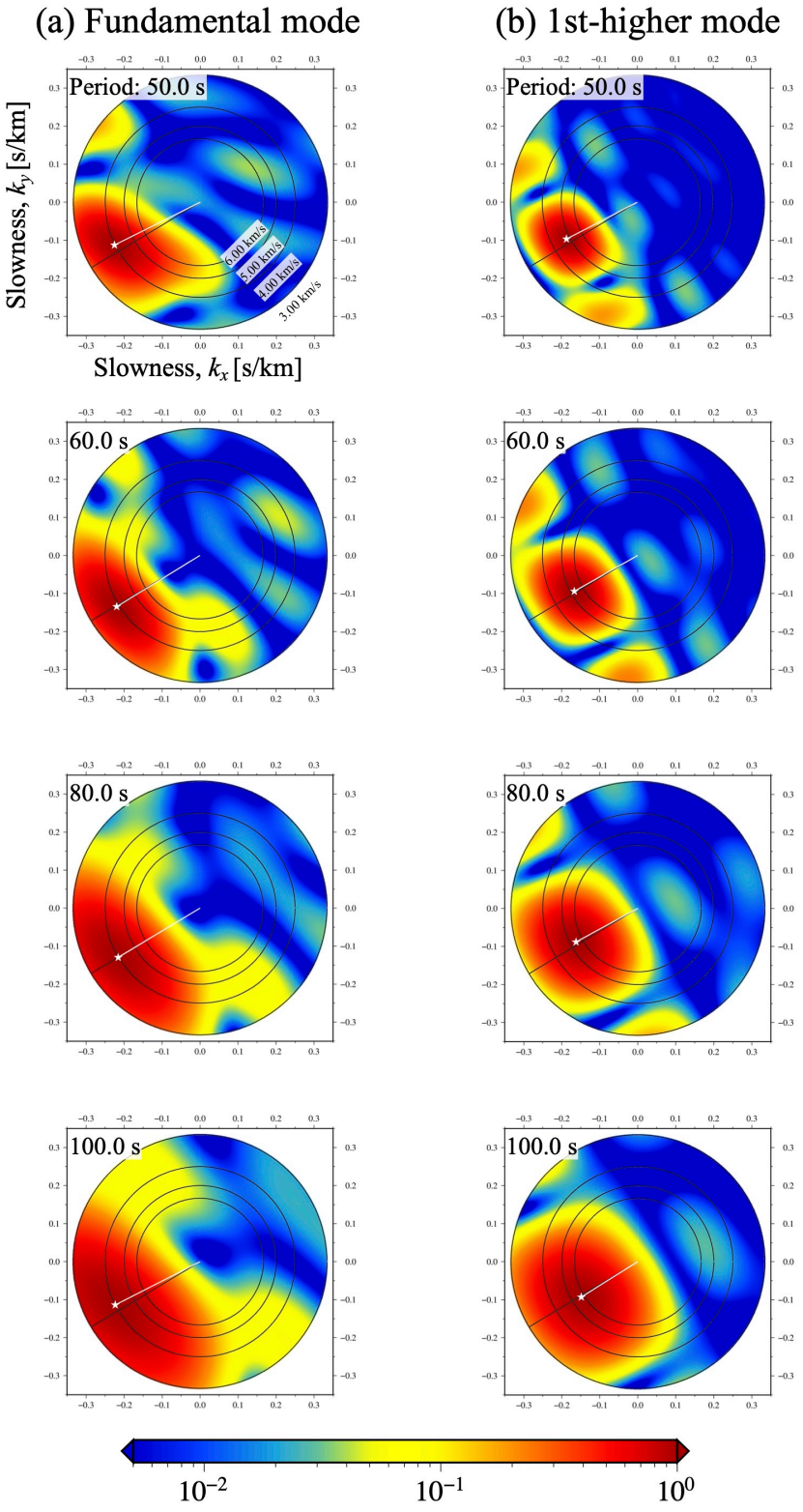



Figure 2.20: Power spectra by the 2D $f$-$k$ beamforming for the fundamental-mode and the 1st-higher-mode Rayleigh waves at 50 s, 60 s, 80 s and 100 s. The spectral peaks (white star and solid line) indicate phase velocity of surface wave propagating within the Array-I. The azimuth to the source is indicated by black solid line.

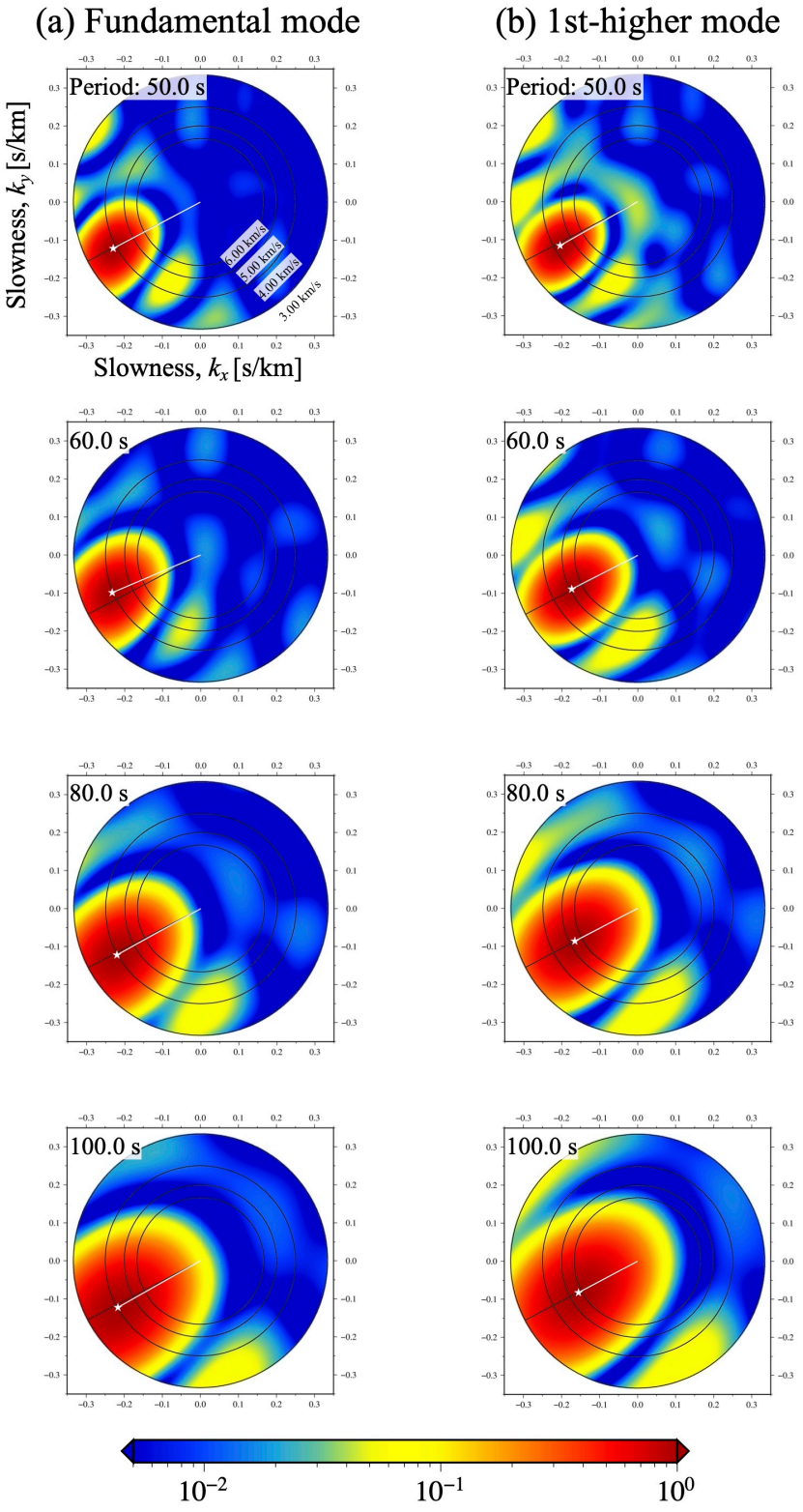



Figure 2.21: Same as Fig. 2.20, but for the Array-II.

# Chapter 3

# Phase Speed Mapping with a Linear-array Method

## 3.1 Introduction

In this chapter, the linear-array method in the previous chapter is applied to a large dataset of seismograms observed at broadband seismic stations in the contiguous United States. We will demonstrate the validity of our method and the difference among several mapping techniques by comparing fundamental-mode phase speed maps. Seismic waveform data were downloaded from the IRIS Data Management Center using "SOD" (Standing Order for Data, Owens et al., 2004). Event locations and focal mechanisms were taken from the Global CMT catalog (Dziewoński et al., 1981; Ekström et al., 2012).

## 3.2 Methods for Phase Speed Mapping

Using the multi-mode dispersion data derived from a long linear-array in the previous chapter, here we employ three different ways to construct phase speed maps.

### 3.2.1 Phase speed maps (1): the direct use of long linear arrays

The most straightforward approach for phase speed mappings is based on a linearized inversion with ray theory. The phase speeds measured from the 1-D linear array analysis along great-circle paths can be simply mapped into the space domain through the conventional tomographic inversion scheme incorporating the weight function along the path, as shown in Fig. 2.7 in the previous chapter. In this study, the method of surface wave tomography developed by Yoshizawa & Kennett (2002a, 2004) has been employed to construct phase speed maps using the path-averaged data derived from long linear arrays. Spatial parameters (local phase speeds) are expanded in the spherical B-spline functions. Linear simultaneous equations are solved by a damped least-squares scheme using the LSQR algorithm (Paige & Saunders, 1982). A damping parameter for each period is assessed by visually checking the trade-off curve between the data misfit and model roughness (Yoshizawa & Kennett, 2004).

### 3.2.2 Phase speed maps (2): inter-centroid (inter-station) dispersion analysis

An alternative linear inversion approach is to incorporate the inter-station dispersion analysis, which has been also employed to construct another set of phase speed maps in this study. The inter-station analysis based on fully nonlinear waveform fittings (Hamada & Yoshizawa, 2015; Hamada, 2017) is applied to the decomposed fundamental-mode waveforms at the centroid location of each linear sub-array derived from the method described in Chapter 2. A set of modal waveforms at centroid locations is used to extract inter-centroid (i.e., equivalent to inter-station) phase speeds with different centroid pairs.

The inter-station method by Hamada & Yoshizawa (2015) utilizes the

Neighbourhood Algorithm (Sambridge, 1999a,b) as a global optimizer for a fully nonlinear waveform fitting between seismograms at two stations on a common great-circle path, by modulating both phase and amplitude terms of the fundamental-mode surface waves. In this study, we use only the phase term derived from this method. The reliability parameter for each measurement, which represents how well the waveforms at two stations can be fitted in the time-frequency domain, is used as a data selection criterion as well as the weight value on each measurement during the linear inversion. The linear inversion scheme for phase speed mapping is the same as described in the previous section. Since the path-length of the inter-station (inter-centroid) analysis is generally shorter than that of the single-station method (i.e., 1-D linear array analysis), the horizontal resolution of phase speed maps derived from inter-station (inter-centroid) analysis can be much enhanced.

### 3.2.3 Phase speed maps (3): eikonal tomography with 2-D array analysis

The other method of phase speed mapping is based on the eikonal tomography (Lin et al., 2009). This method uses two-dimensional array analysis based on the eikonal equation. From the Helmholtz equation derived from the wave equation, we can derive the following relation (e.g., Wielandt, 1993; Lay & Wallace, 1995; Shearer, 1999):

$$\frac{1}{c\left(\omega,\mathbf{r}\right)^{2}}=\left|\nabla\tau\left(\omega,\mathbf{r}\right)\right|^{2}-\frac{\nabla^{2}A\left(\omega,\mathbf{r}\right)}{A\left(\omega,\mathbf{r}\right)\omega^{2}}, \tag{3.1}$$

where $\omega$ is the angular frequency, $\mathbf{r} = (\mathbf{x}, \mathbf{y})$ the 2-D position vector, $c$ the phase speed, $A$ the wave amplitude, and $\tau$ the phase travel time, respectively. $\nabla$ represents the 2-D differential operator $(\partial/\partial x, \partial/\partial y)$, and $\nabla^2$ the 2-D Laplacian $(\partial^2/\partial x^2 + \partial^2/\partial y^2)$. The left-term represents the slowness term, while the first and second terms in the right-term mean the gradient of the traveltime field and the effects of ray bending such as focusing and defocusing.

The eikonal equation can be derived from eq (3.1) by neglecting the amplitude term with the high-frequency approximation (or the weak spatial changes in the amplitude field):

$$\frac{1}{c\left(\omega,\mathbf{r}\right)^{2}}=\left|\nabla\tau\left(\omega,\mathbf{r}\right)\right|^{2}$$
$$\Longrightarrow\mathbf{p}\left(\omega,\mathbf{r}\right)\simeq\nabla\tau\left(\omega,\mathbf{r}\right),$$

where $\mathbf{p}=(p_x,p_y)$ is the slowness vector. This equation enable us to directly derive the phase speed distributions from the gradients of the 2-D travel-time field without solving any inverse problems. It should be noted that the tomographic technique based on the Helmholtz equation (or Helmholtz tomography) incorporating both phase travel-time and amplitude variations has been recently used widely in the ambient noise tomography (Lin & Ritzwoller, 2011).

The eikonal tomography complements traditional surface wave tomography methods in several ways (Lin et al., 2009). First, there are no explicit regularizations, so that the method is free from some empirical choices of *a priori* constraints. Second, this tomography accounts for ray bendings automatically, without ray tracings. The gradient of the travel-time field naturally includes the information of the local traveling direction of waves. Finally, in the construction of phase speed maps, the matrix construction and inversion of traditional methods are replaced by constructing the travel-time field, that is, the computation of its gradients and averaging. Therefore, the computational costs of the eikonal tomography are relatively small.

The eikonal tomography has been widely used for the ambient noise data (e.g., Ritzwoller et al., 2011; Zhou et al., 2012; Lin et al., 2013). Our method of the modal waveform decomposition makes it possible to use this technique for mode-branch waveforms of each mode. In this study, after the decomposition, we apply the single-station dispersion analysis with FTAN,

a frequency-time analysis (e.g., Levshin et al., 1972; Ritzwoller & Levshin, 1998) to each modal waveform for each event. Then, we construct the travel time field at each period for each mode. The phase speed maps are then obtained by averaging the gradients for each event.

## 3.3 Data and Processing

### 3.3.1 Linear-array phase speed measurements

We used 710 teleseismic events ($M_w \geq 5.8$, excluding multiple concurrent earthquakes) shown in Fig. 3.1 to map phase speed distributions for the multi-mode Rayleigh and Love waves. These events occurred from 2007 to 2015, corresponding to the duration of USArray deployment. Our data set consists of seismograms recorded at USArray (TA), Berkeley Digital Seismograph Network (BK), Southern California Seismic Network (CI), Canadian National Seismic Network (CN), GEOSCOPE (G), GEOFON (GE), United States National Seismic Network (US) and Global Seismographic Network (II, IU).

We eliminated stations located in the nodal directions of surface wave radiation or too close to the epicenter (with the epicentral distance less than 2000 km). We also excluded stations located at epicentral distances more than 12000 km for Rayleigh wave analysis and 14000 km for Love wave away to avoid contaminations due to the R2/X2/G2 phases propagating along the major-arc (Hariharan et al., 2020). Prior to the multi-mode dispersion analysis, waveforms are preprocessed by removing offset and linear trends, deconvolving the instrument response of each seismometer, and applying a wide bandpass filter (0.002–0.1 Hz). We eliminated seismograms with an S/N ratio lower than 0.7, defined by the ratio between the maximum amplitude of the signal and the root-mean-square of noises before the P-wave arrival. We also eliminated seismograms that appear to be incoherent with those of the

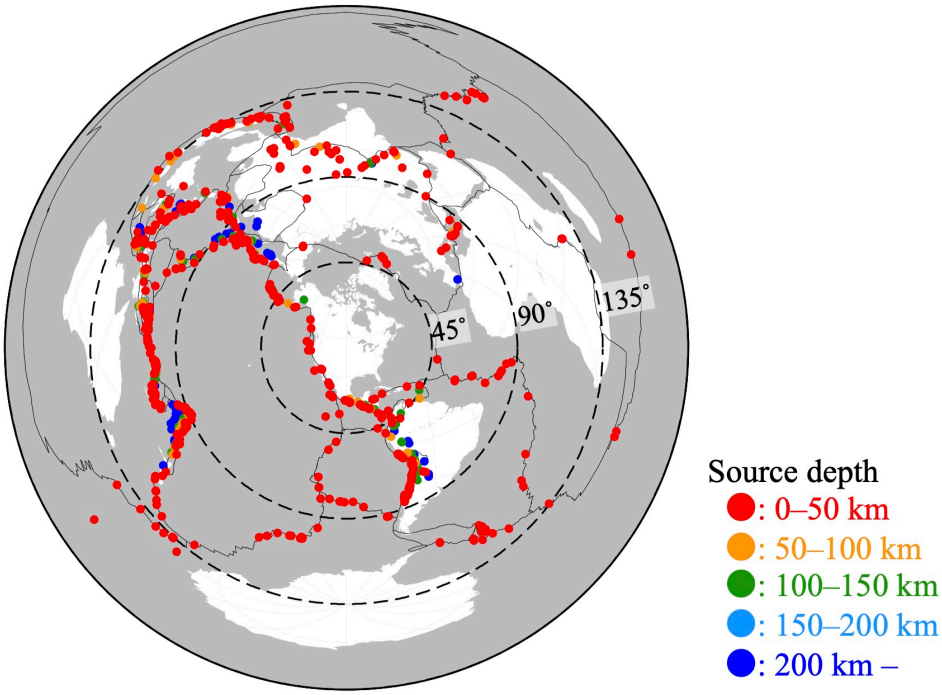



Figure 3.1: Distribution of the events used in this chapter. The color indicates the source depth. (red) 0–50 km, (orange) 50–100 km, (green) 100–150 km, (cyan) 150–200 km and (blue) deeper than 200 km.

neighboring stations in an array, for example, the correlation coefficient is less than 0.7. These preprocessings help us to avoid the phase speed spectrogram contaminated by high background noises.

We have collected about 105000 measurements along a linear array and its subarrays for Rayleigh waves and 45000 measurements for Love waves. The numbers of measurements are as much as those of the collected centroids. Two examples of path coverage maps for Rayleigh and Love waves are displayed in Fig. 3.2. Adequate path coverages across the contiguous U.S. are achieved in both cases. Fig. 3.3 displays checkerboard resolution tests for Rayleigh and Love models at a period of 100 s. In all the cases, the input checkerboard models have the maximum perturbations of about $\pm 6.0\%$ from the reference phase speed. In the resulted maps (Fig. 3.3), we can see some smearing effects mainly in the NW-SE direction, which is mainly caused by the relatively small number of events located in the northeast of the U.S.

### 3.3.2 Inter-centroid phase speed measurements

For the application of the subsequent inter-station (inter-centroid) dispersion analysis for the fundamental-mode waveforms, we employ about 33000 centroid-pairs for Rayleigh waves and about 8000 centroid-pairs for Love waves. The centroid-pairs with distances shorter than the target wavelength (150–500 km) are eliminated. Fig. 3.4 shows the distributions of ray paths (line segments) between centroids for Rayleigh and Love waves at the period of 100 s.

Since the centroids for long linear arrays with a few thousand kilometers are mostly located in the middle of the continent, the line segments (ray paths) connecting two centroids tend to be concentrated only in the inland area, but only a few in the coastal areas. Thus, the resulting phase velocity maps will have sufficient resolution only in the center of the continent. This

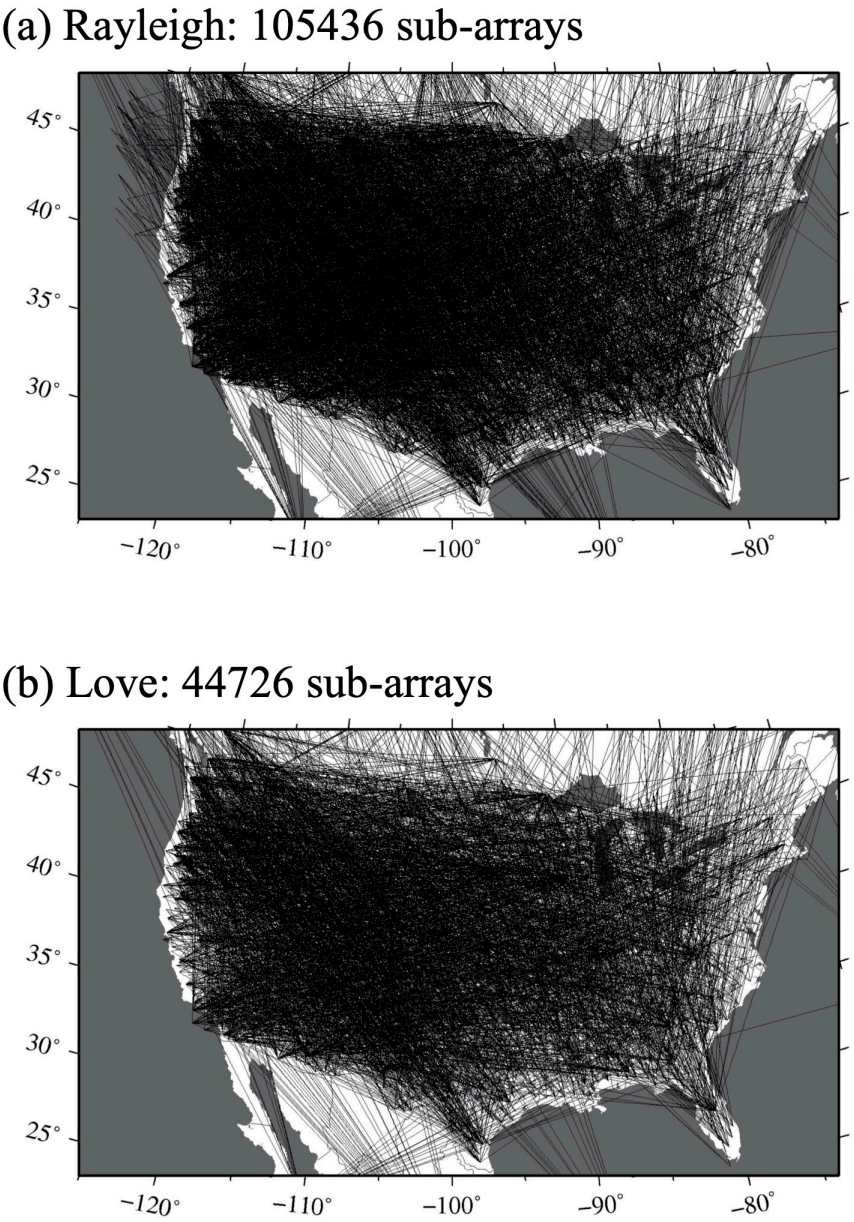



Figure 3.2: The sub-array path coverage in and around the U.S. for (a) Rayleigh and (b) Love waves.

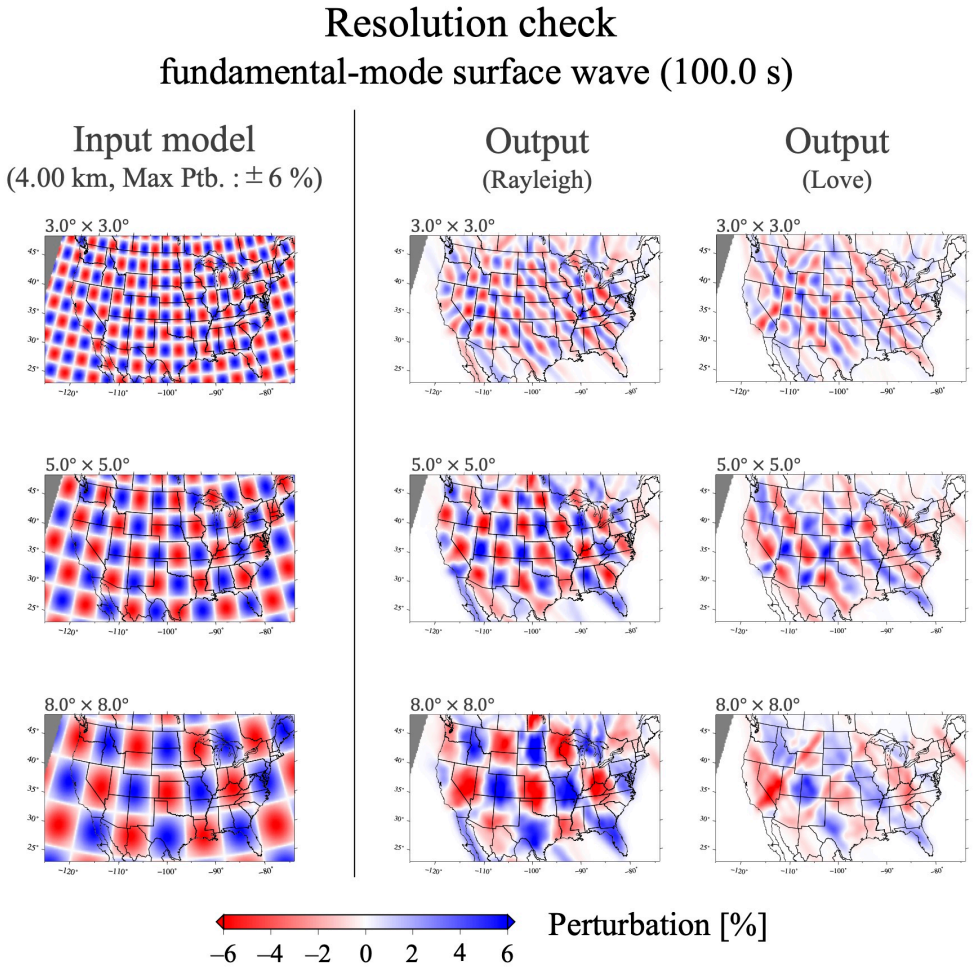



Figure 3.3: Examples of checkerboard resolution tests for the fundamental-mode Rayleigh and Love wave phase speed maps derived from the average phase speeds along the linear arrays at 100.0 s with cell sizes of 3.0° × 3.0°, 5.0° × 5.0° and 8.0° × 8.0°. Left panels are input checkerboard patterns, and center and right panels are output models for Rayleigh and Love wave.

is suggested by our checkerboard tests similar to the previous case (Fig. 3.5). In the maps with cell sizes of 3.0°, 5.0° and 8.0°, heterogeneity patterns are well recovered especially in the inland area covered with the many ray paths, but not in the coastal areas. This effect tends to be remarkable in a long period range since their wavelengths become long and short-path information cannot be reliably extracted.

### 3.3.3 Phase travel times at linear-array centroids for eikonal tomography

We implemented the eikonal tomography using all the centroids of the linear array obtained for each of 710 events. After the modal wave decomposition, the FTAN is applied to each of the mode-branch waveforms to map the travel time field (Fig. 3.6a). Then, we obtained a phase speed map of a the small region covered with the centroids using the gradient of the travel time field (Fig. 3.6b). The phase speed distribution in the entire U.S. is derived by averaging maps of all the event.

## 3.4 Three-types of Phase Speed Maps with Linear-array Measurements

Examples of fundamental-mode phase speed maps of the U.S. at periods of 40.0 s, 60.0 s, 80.0 s, and 100.0 s are shown in Fig. 3.7 for Rayleigh waves and in Fig. 3.8 for Love waves. We compare the following three different phase-speed mapping methods;

(A) linear inversion using the average phase speed of each long linear array

(B) linear inversion using the "inter-centroid" phase speeds

(C) eikonal tomography using the mode-branch waveforms at centroids of subarrays

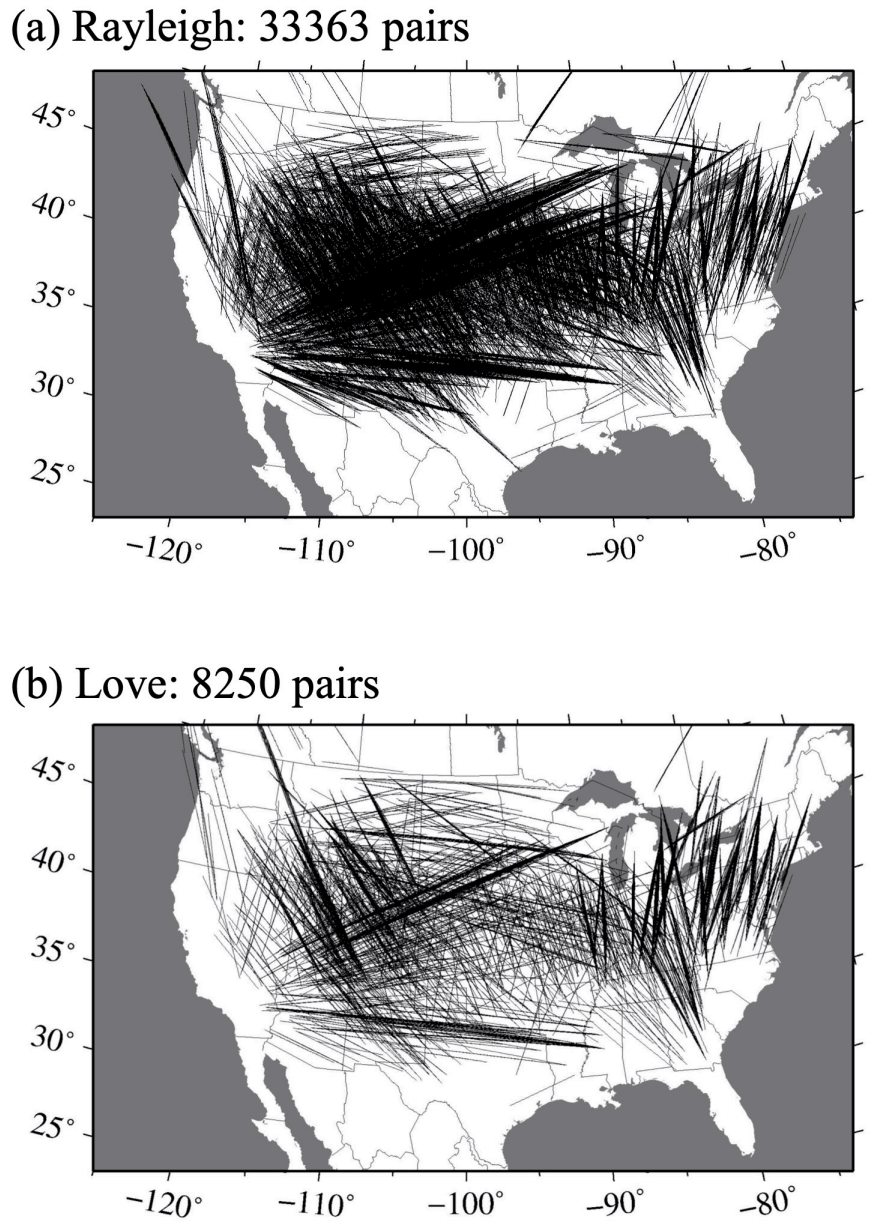



Figure 3.4: The coverage of inter-centroid paths (connecting two centroids of the subarrays) for the fundamental-mode (a) Rayleigh and (b) Love waves at a period of 100 s.

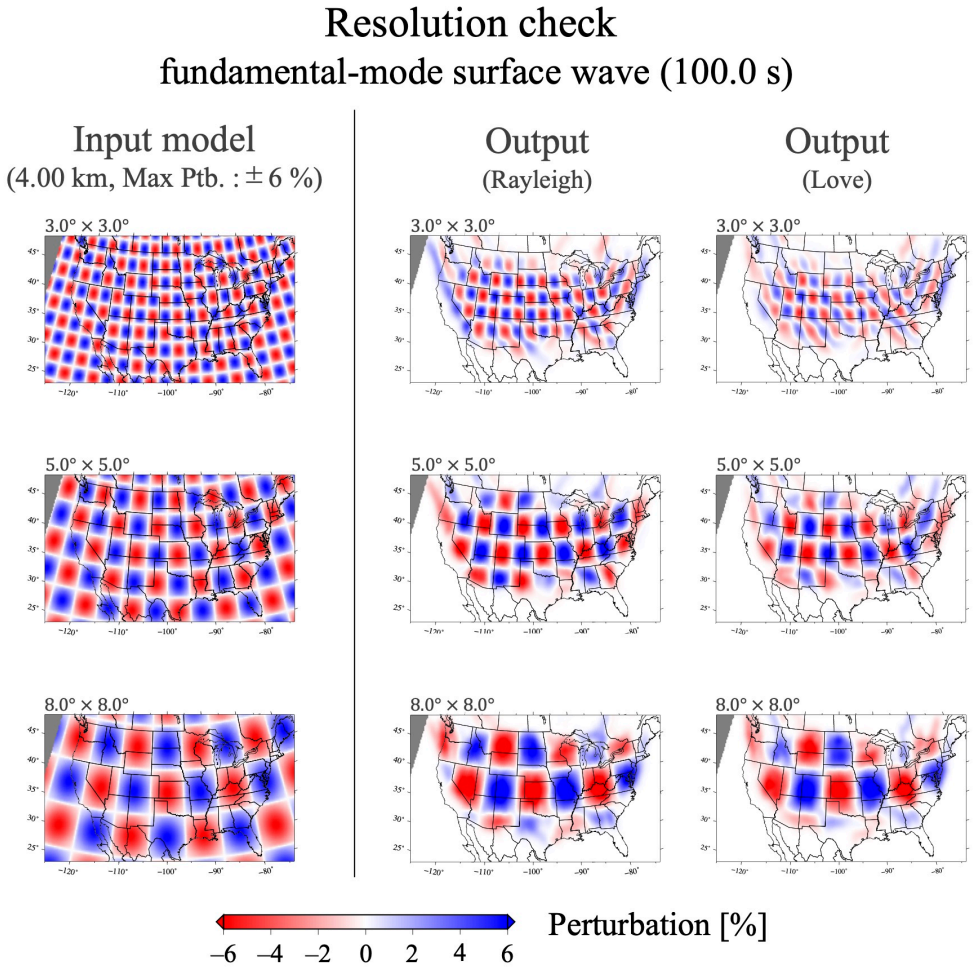



Figure 3.5: Examples of checkerboard resolution tests for the fundamental-mode Rayleigh and Love wave phase speed maps derived from the inter-centroid phase speeds at 100.0 s with cell sizes of 3.0° × 3.0°, 5.0° × 5.0° and 8.0° × 8.0°. Left panels are input checkerboard patterns, and center and right panels are output models for Rayleigh and Love wave.

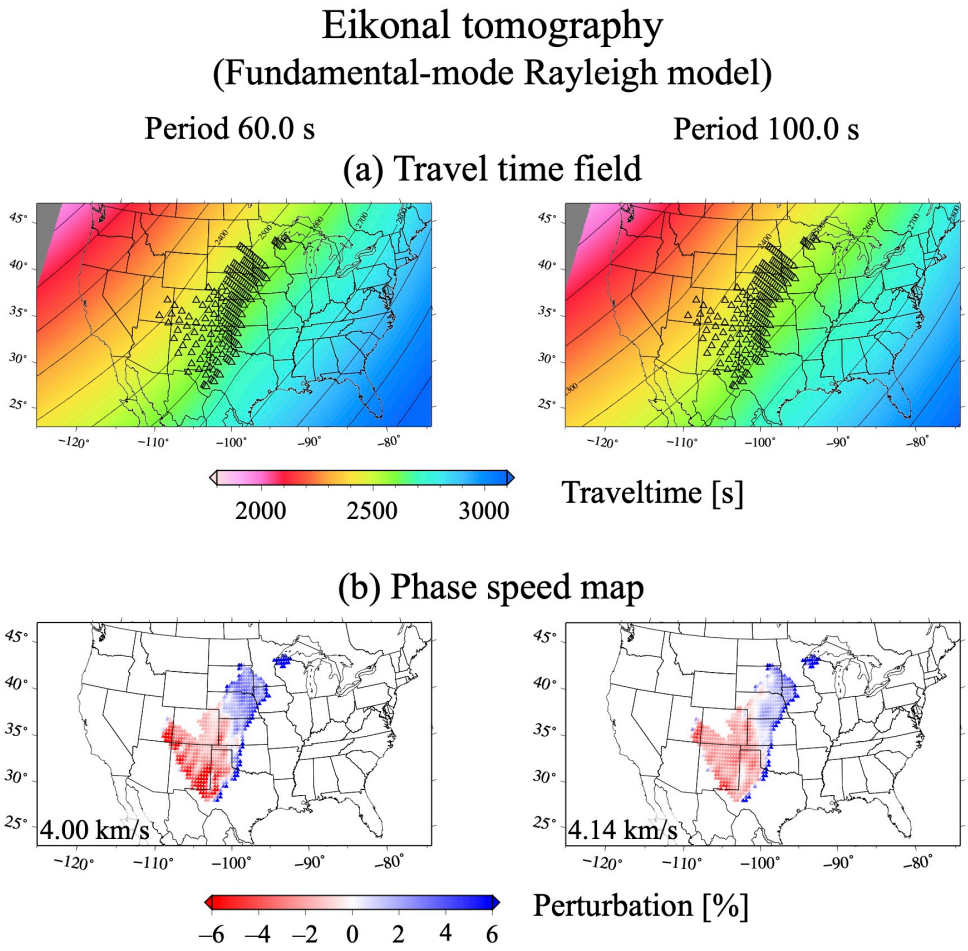



Figure 3.6: The procedure of the eikonal tomography. (a) Travel time field for the fundamental-mode Rayleigh wave at (left) 60.0 s and (right) 100.0 s. (b) The phase speed distribution within the centroids obtained by the gradient of the travel time field shown in (a). The triangles indicate the centroids of the linear array.

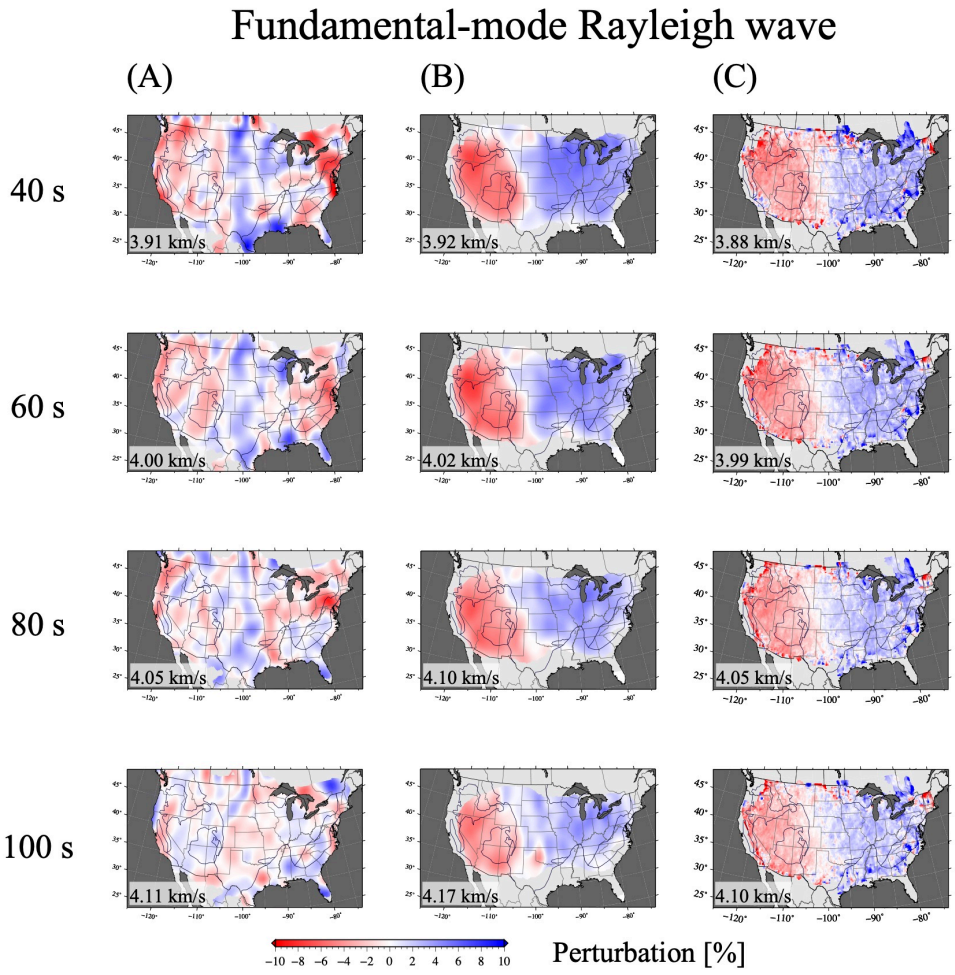



Figure 3.7: The phase speed maps for the fundamental-mode Rayleigh waves at 40 s, 60 s, 80 s, and 100 s derived from the linear inversion of (A) phase speeds for long linear array and (B) the inter-centroid phase speeds. (C) Eikonal tomography using the mode-branch waveforms at the centroids of subarrays.

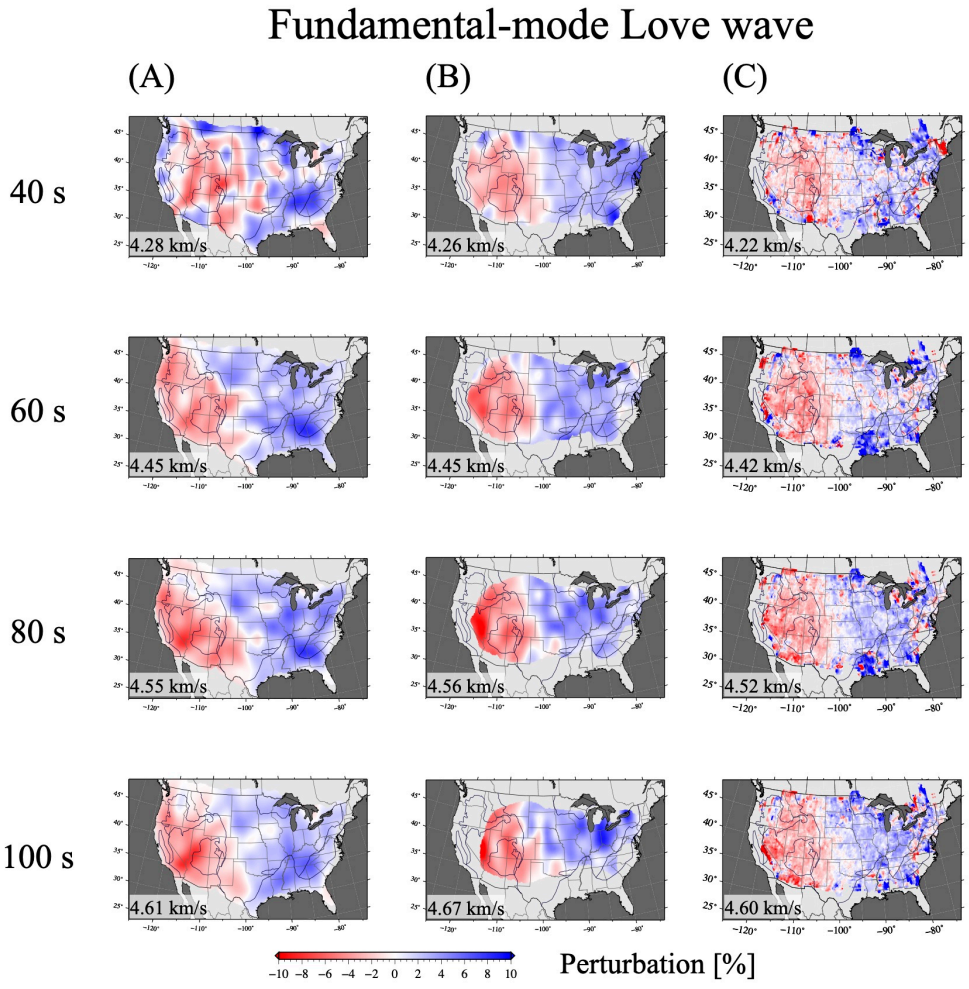



Figure 3.8: Same as Fig. 3.7, but for the fundamental-mode Love waves.

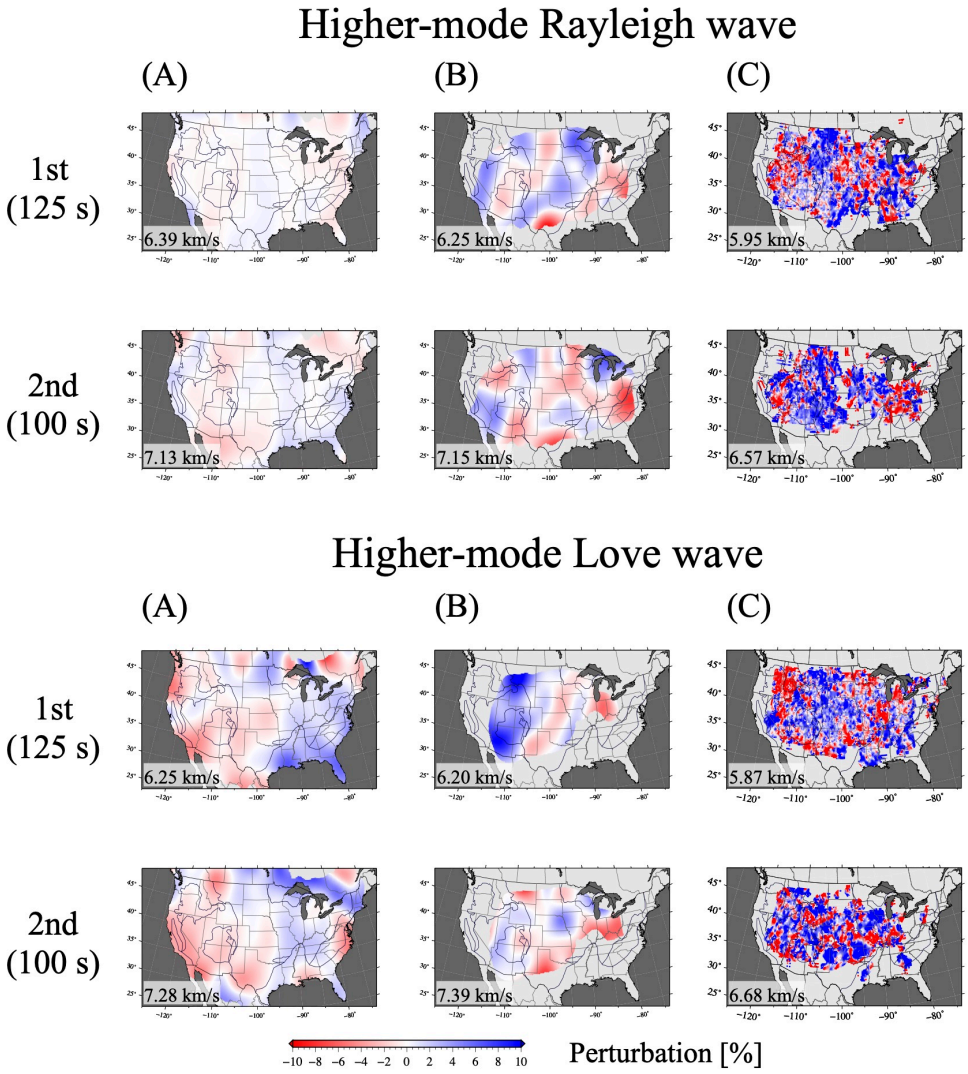



Figure 3.9: The phase speed maps for (top) the higher-mode Rayleigh and (bottom) Love waves derived from the linear inversion of (A) phase speeds for long linear array and (B) the inter-centroid phase speeds. (C) Eikonal tomography using the mode-branch waveforms at the centroids of subarrays.

In Figs. 3.7 and 3.8, we plot phase speed perturbations from −10% (red) to +10% (blue) with respect to the average in the U.S. for the models (A), (B) and (C). The achieved variance reductions by these inversions are (A) 30–40 % and (B) 70–75 % for Rayleigh waves, and (A) 40–50 % and (B) 36–51 % for Love waves. Fig. 3.9 displays phase speed distributions of higher-modes; 1st-higher-mode Rayleigh wave (refereed as R1 below) at 125.0 s, 2nd-higher-mode Rayleigh wave (R2) at 100.0 s, 1st-higher-mode Love wave (L1) at 125.0 s and 2nd-higher-mode Love wave (L2) at 100.0 s. The variance reductions of the higher-mode inversions are (A) R1: 22 %, R2: 40 %, L1: 8 %, L2: 10 % and (B) R1: 7 %, R2: 6 %, L1: 7 %, L2: 6 %, which tend to be much lower than those of the fundamental modes.

The average phase speeds are consistent with each other for the fundamental-mode models. A strong phase speed contrast between the western and central United States divided by the Rocky Mountains has been imaged well in all the cases. Such a typical tectonic feature has been commonly observed in earlier tomography models of North America in both global-scale (e.g., Nettles & Dziewoński, 2008; Visser et al., 2008; Ekström, 2011) and continental-scale studies (e.g. Yoshizawa & Ekström, 2010; Schaeffer & Lebedev, 2014; Hamada & Yoshizawa, 2015). While the phase speed maps in (B) and (C) have the horizontal resolution equivalent to global-scale models (5.0°–8.0°), small-scale heterogeneities can be more visible in the maps in (A). For example, in the fundamental-mode Rayleigh wave models at 40 s, we can see fast anomalies corresponding to Colorado Plateau, which was observed in earlier high-resolution tomographic studies using the inter-station method by Foster et al. (2014b); Hamada & Yoshizawa (2015). However, many small-scale and linear heterogeneities in (A) do not represent the tectonic features in the U.S., which are likely to be affected by relatively larger measurement errors in some specific paths.

In the phase speed models in both Rayleigh and Love wave models of (B) and (C), relatively fast anomalies corresponding to the Colorado Plateau cannot be very well resolved. These small-scale anomalies seem to be buried in the typical large-scale slow anomalies of the western U.S., indicating that local-scale tectonic features with 100-km-scales cannot be well resolved with our long linear-array-based measurements.

In the higher-mode models in Fig. 3.9, the average phase speeds of (A) and (B) are consistent with each other, but those of (C) are very different. The interpretation of higher-mode phase speed maps is difficult since their vertical sensitivity to the shear-wave structure is complex. The eikonal tomography maps in (C) are too patchy and unrealistic. The phase speed maps from inter-centroid measurements in (B) show the large-scale patterns of 400–500-km-scale, which are also difficult to interpret. These models in (B) and (C) indicate the difficulty in applying the decomposed higher-mode waveforms for the inter-centroid measurements and eikonal tomography based on the phase-front tracking. On the contrary, the model of (A) shows the large-scale pattern of the slow anomaly in the western area and fast anomaly in the eastern area, consistent with the previous higher-mode models in Yoshizawa & Ekström (2010).

## 3.5 Discussion

Based on the 1-D linear array analysis for multi-mode phase speed measurements and the modal waveform decomposition described in chapter 2, we have developed several methods to construct phase speed maps utilizing a variety of techniques to extract localized phase speeds. Using the linear array analysis, we can measure the multi-mode phase speeds in a broad period range even if several surface-wave modes overlap. We can also untangle the observed waveforms in a linear array to the mode-branch waveforms at the

centroid of the array, which helps us to extract the local heterogeneities for each mode in the subsequent dispersion analysis as proposed by Matsuzawa & Yoshizawa (2019).

In this chapter, we applied the above linear array methods to the seismograms recorded at broad-band stations, including USArray and several seismic networks in North America, for constructing several types of phase speed maps. Such a 1D-array-based analysis was originally developed in the 1970s (e.g., Nolet, 1975, 1976; Cara, 1978), but has been rarely applied for tomographic studies. One of the main reasons was due to the consideration that this style of linear array analyses does not allow us to extract variations within a long linear array (e.g., Laske & Widmer-Schnidrig, 2015). However, this problem may be overcome with seismic data of the modern highly-dense broad-band arrays such as USArray.

The resultant phase speed maps are shown in Fig. 3.7 for fundamental-mode Rayleigh waves, Fig. 3.8 for fundamental-mode Love waves and Fig. 3.9 for several higher-modes. The maps in (A) are derived from the linear inversions using the average phase speed along a linear array. Although the large-scale anomalies (i.e., fast anomalies in cratons in the stable eastern U.S., slow anomalies in the tectonically-active western U.S.) can be identified, the lateral resolution of phase speed maps was insufficient to discuss local-scale tectonic features. These results suggest that small-scale (several hundred kilometers) tectonic characteristics tend to be blurred and averaged out with the direct measurements of phase speeds for a long linear array (2000–4000 km).

The phase speed maps derived from the inter-station (inter-centroid) dispersion analysis with nonlinear waveform fittings (Hamada & Yoshizawa, 2015; Hamada, 2017) are shown in panels (B) of Figs. 3.7, 3.8 and 3.9, and the maps derived from the eikonal tomography method (Lin et al., 2009) are

shown in panel (C). Their lateral resolution is slightly higher than that of global models but lower than the earlier regional models. One of the causes for degrading the apparent resolution of these models may be the accumulation of errors through several processes during the data analysis; for example, the mode decomposition, the phase speed measurements by the inter-station (inter-centroid) analysis or the FTAN method, and the calculation of the finite difference for gradients of the travel-time fields for the eikonal tomography. Those accumulated errors may mask smaller-scale tectonic features in the U.S. in our tomography models, originally based on the long-range linear array measurements. However, it is difficult to assess the errors included in each phase speed measurements from the data set of modal waveforms.

# Chapter 4

# A Hybrid Approach for Multi-mode Phase Speed Mapping: Single-station Dispersion Measurements and Eikonal Tomography

## 4.1 Introduction

In the previous chapter, we have investigated several types of phase speed maps based on our linear array analysis. Nevertheless, the lateral resolution of these models appears to be limited compared to the conventional tomography models. To overcome this problem, we now investigate an alternative hybrid approach by employing single-station multi-mode dispersion measurements and 2-D array analysis.

In this chapter, we implement this hybrid method combining the single-station analysis for the multi-mode surface wave dispersion measurements (e.g., Yoshizawa & Kennett, 2002a; Yoshizawa & Ekström, 2010) and the eikonal tomography for mapping the phase speed distributions (Lin et al., 2009). We first measure multi-mode phase speeds for many source-receiver pairs using USArray data. These measurements are, first, inverted directly for phase speed maps using the finite-frequency tomography by Yoshizawa & Kennett (2004). We next apply those phase speed data to the eikonal to-

Table 4.1: Threshold values of the reliability parameters and normalized radiation amplitude used as selection criteria of reliable multi-mode dispersion measurements (Yoshizawa & Ekström, 2010). These threshold values vary depending on the waveform misfit values.

| Waveform misfit | Minimum reliability | | Minimum radiation |
|---|---|---|---|
| | Fundamental mode | Higher modes | |
| 0.00–0.01 | 8.0 | 2.0 | 0.50 |
| 0.01–0.02 | 9.0 | 2.5 | 0.60 |
| 0.02–0.03 | 10.0 | 3.0 | 0.70 |

mography, which may allow us to extract high-resolution phase speed models for local-scale lateral heterogeneities in a dense seismic array.

## 4.2 Method of Single-station Multi-mode Dispersion Measurements

We measure multi-mode phase speeds using the single-station dispersion analysis developed by Yoshizawa & Kennett (2002a) and automated by Yoshizawa & Ekström (2010). This approach is based on non-linear waveform inversions with the Neighbourhood Algorithm (NA) by Sambridge (1999a), which is used as the global optimizer.

Here we explain this method briefly with an example of applying to a waveform observed at a USArray station (E13A) in Fig. 4.1. The event used in this example is located in the Fiji Islands region with focal depth at 30 km. The station E13A is located in Montana with the epicentral distance of about 9500 km. Its ray path traverses the Pacific Ocean from the southwest to the northeast.

The path-specific 1-D shear wave speed profile, which best fits the observed waveform, is derived from the global search through the automatic waveform fitting process using the NA. Several time windows, including multiply-reflected S-waves and surface wave portions, are selected from an

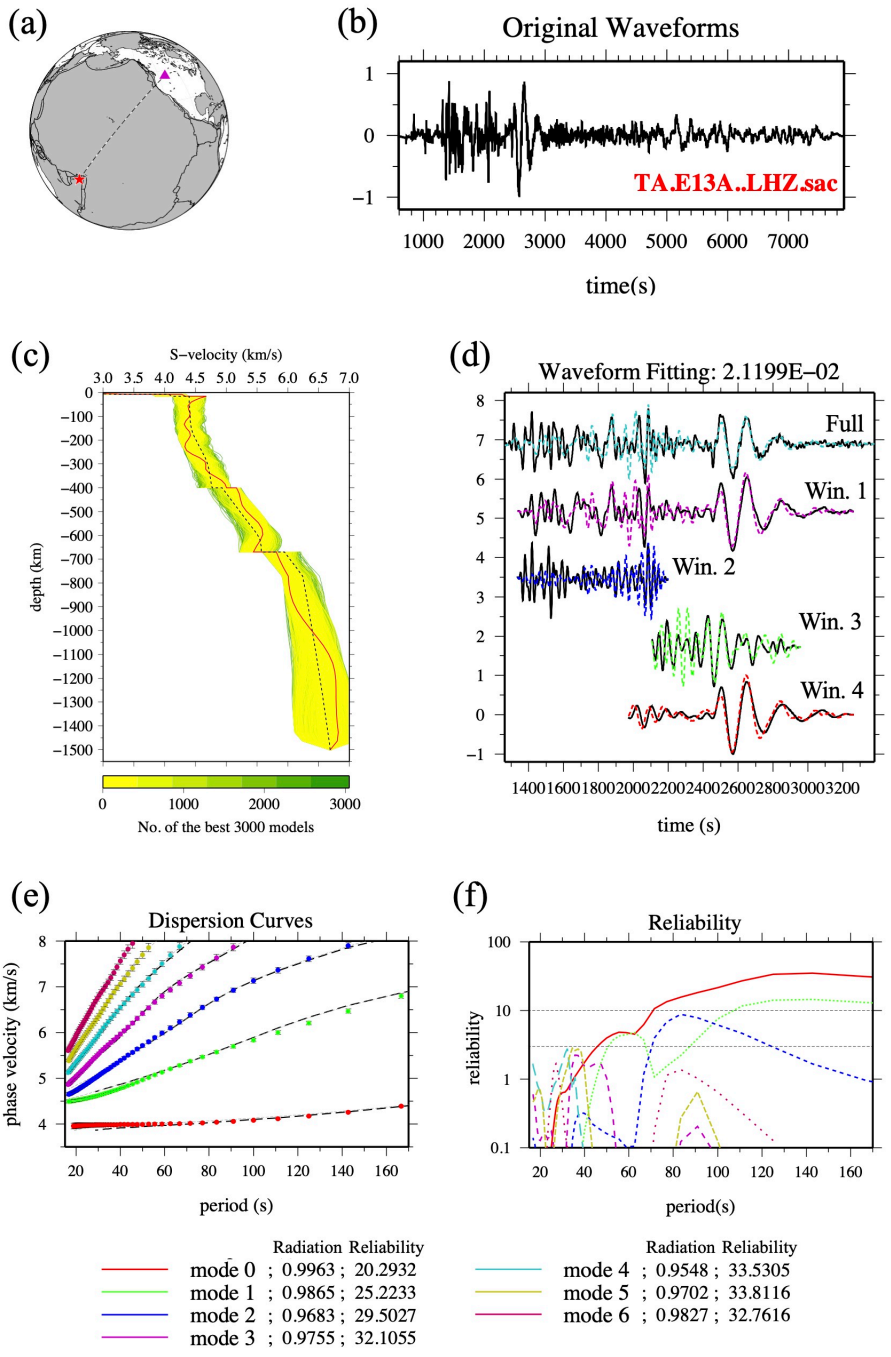



Figure 4.1: The procedure of the single-station multi-mode dispersion analysis (Yoshizawa & Ekström, 2010): (a) a ray path (black dashed line) between a source (red star in Fiji) and a receiver (purple triangle, TA.E13A station of USArray). (b) The original waveform observed at E13A. (c) Path-average 1-D S wave profile along the path in (a). The red line represents the best model with the minimum waveform misfit, and the best 3000 models (in a total of 5050 models) are ranked in order of the smaller misfit and plotted with colors varying from green (larger misfit) to yellow (smaller misfit). (d) the resultant waveform fit between the observed (the solid black lines) and synthetic waveforms (the colored dashed lines) in multiple time windows. (e) Resultant dispersion curves from the fundamental-mode to the 8th higher-mode Rayleigh waves calculated for the best-fit model in (c). (f) The reliability parameters of dispersion measurements for each mode.

observed waveform, based on the pre-defined multiple group-speed windows (four for Rayleigh / three for Love waves). Multiple band-pass filters are then applied to each window as described by Yoshizawa & Ekström (2010). Fig. 4.1(d) shows waveforms in selected time windows. The normal-mode synthetic waveforms (solid black lines in Fig. 4.1(d)) are calculated for a bunch of 1-D models derived from NA, based on the surface-wave WKBJ theory (Dahlen & Tromp, 1998) using the focal mechanism taken from the global CMT catalog (Ekström et al., 2012). The observed and synthetic seismograms are then fitted in all the time windows with multiple band-pass filters.

The 1-D shear wave speed profile with the minimum waveform misfit, searched by the NA, is shown as the solid red line in Fig. 4.1(c). This 1-D model is used to compute the multi-mode phase dispersion from the fundamental mode up to the 8th higher-mode. Fig. 4.1(e) displays the resultant dispersion curves along the ray path in Fig. 4.1(a). This dispersion curve reflects the typical oceanic S wave structure. The reliability parameters of phase speed measurements as a function of a frequency are shown in Fig. 4.1(f), estimated from the waveform misfit and the relative power of modal excitations at the source. In our single-station multi-mode dispersion measurements, we use the same *a priori* constraints (such as the number of model parameters searched by NA) and the thresholds of measurement reliability as those used by Yoshizawa & Ekström (2010) (see Table 4.1.)

In this study, we first measure the multi-mode phase speeds by the single-station analysis with non-linear waveform fittings for many seismic stations in a dense seismic array using teleseismic events. Then, the phase front maps (i.e., travel-time fields) are computed from these phase speed measurements using a dense seismic network, enabling us to construct the phase speed maps within the array at each frequency based on the eikonal tomography. The

final model is obtained by averaging these maps over a set of events. Through such a hybrid approach of multi-mode dispersion measurements for many stations and eikonal tomography, we can take into account the separation of the overlapped modes through the multi-mode waveform fitting process, and the correction of the off-great-circle propagation and the arrival-angle anomalies through the mapping of phase speed distributions.

## 4.3 Data Sets

### 4.3.1 Data for hybrid phase speed mapping

As in the previous chapter, we employed 710 teleseismic events from 2007 to 2015 with the moment magnitude greater than 5.8. The event distribution used in our hybrid phase speed mapping is displayed in Fig. 3.1. We used the vertical-component seismograms for Rayleigh wave analysis and the transverse-component for Love wave analysis. We collected 80000–100000 paths for the fundamental-mode Rayleigh waves, about 50000 paths for the fundamental-mode Love waves, 10000–70000 paths for higher modes of both Rayleigh and Love waves (Fig. 4.2). Since we employed the same thresholds as those used in Yoshizawa & Ekström (2010), the frequency dependence of the numbers of ray paths is similar to those of Yoshizawa & Ekström (2010) for both Rayleigh and Love waves.

Fig. 4.2 displays coverages, back azimuths and densities of ray paths around the U.S. for the fundamental-mode Rayleigh wave and the 4th-higher-mode Love wave. We have achieved very good coverage across the contiguous U.S. in both cases, even though the present ray path densities are undoubtedly different between these two cases.

For the eikonal tomography, the resolution check in the model space is not straightforward since we do not solve any inverse problems. Here, we show the results of checkerboard resolution tests for linear inversions using the

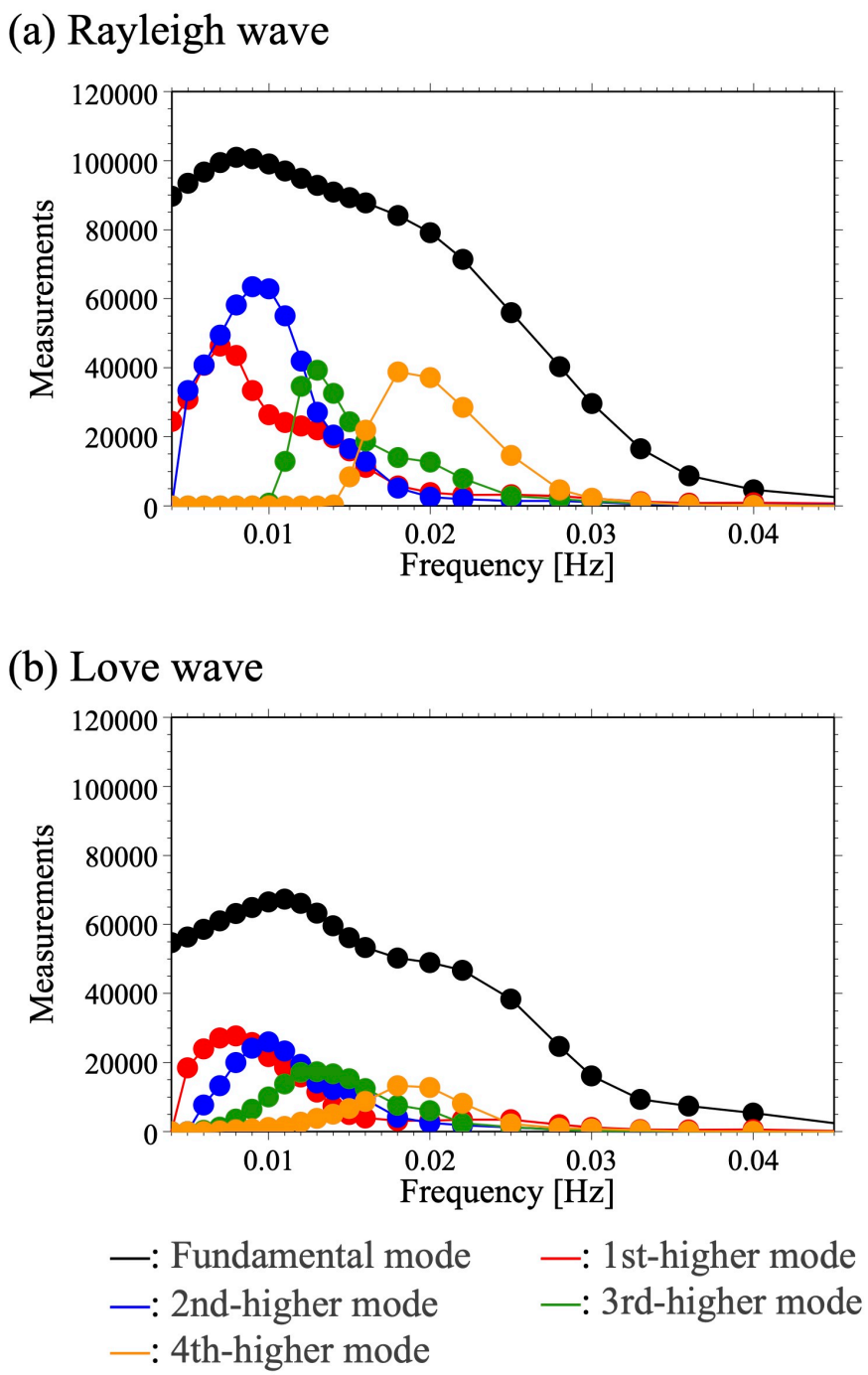



Figure 4.2: Numbers of measurements of multi-mode phase speeds for (a) Rayleigh waves and (b) Love waves, as a function of period.

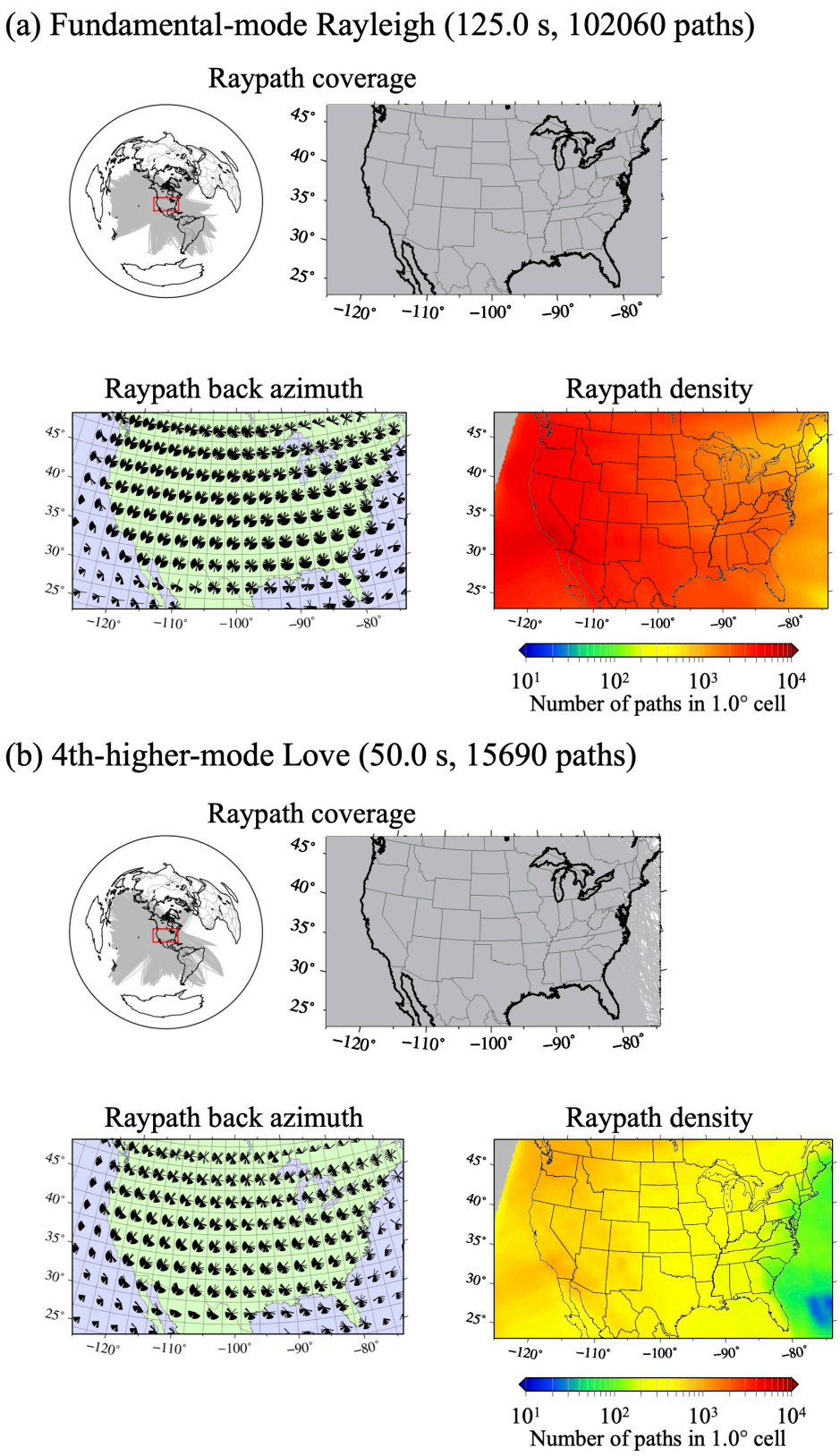



Figure 4.3: The ray path coverage, back azimuths and densities around the U.S. region for (a) the fundamental-mode Rayleigh wave at 125.0 s and (b) the 4th-higher-mode Love wave at 50.0 s.

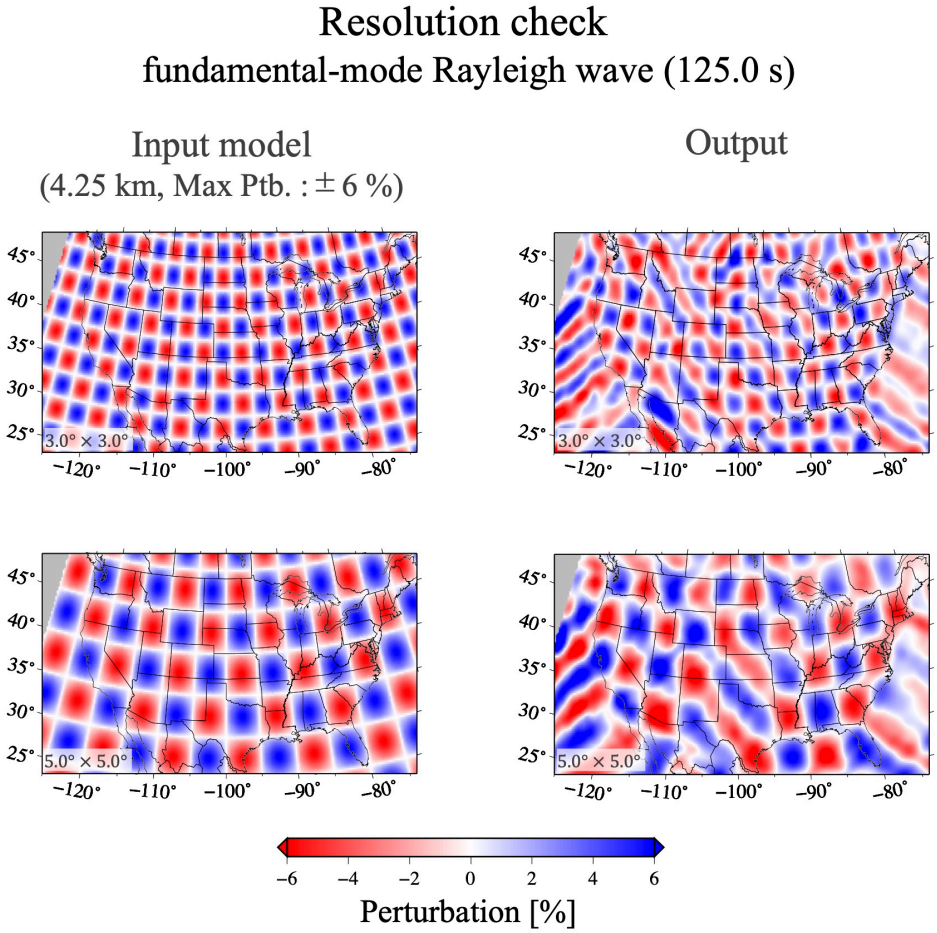



Figure 4.4: Examples of checkerboard resolution tests for the fundamental-mode Rayleigh-wave phase speed maps at 125.0 s with cell sizes of (top) 3.0° × 3.0° and (bottom) 5.0° × 5.0°. Left panels are input checkerboard patterns, and right panels are output models.

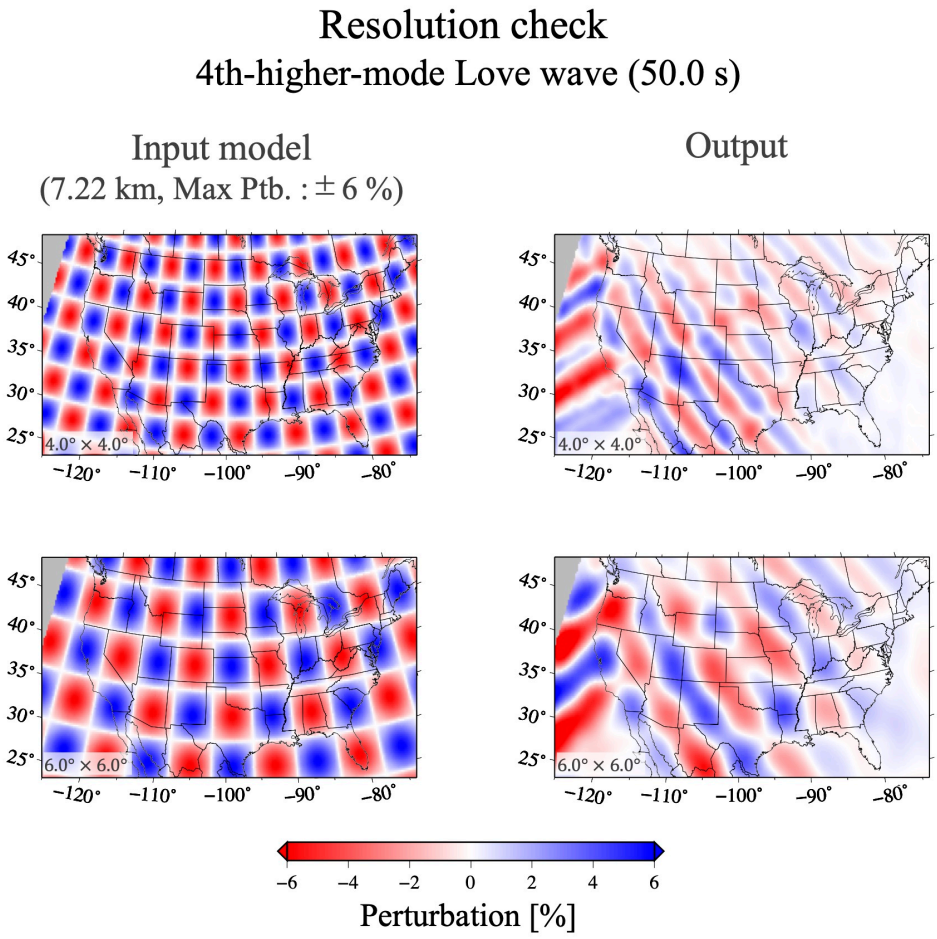



Figure 4.5: Same as Fig. 4.4, but for the 4th-higher-mode Love-wave phase speed maps at 50.0 s with cell sizes of (top) 4.0° × 4.0° and (bottom) 6.0° × 6.0°.

path-averaged phase speed measurement along source-receiver path, which provides us with the insight into the lateral resolution of our data sets. Some examples of the present checkerboard tests are shown in Fig. 4.4 for the fundamental-mode Rayleigh wave and in Fig. 4.5 for the 4th-higher-mode Love wave. In all cases, input checkerboard models have the maximum of perturbations from the reference phase speed to be about ±6.0%. In Fig. 4.4 with the cell sizes of both 3.0° and 5.0° for Rayleigh waves, both strength and pattern of phase speed perturbations in the whole U.S. can be recovered well. This is mainly because a large number (over 100000) of crossing paths from various directions in each cell. In the case of higher-mode Love waves (Fig. 4.5), the number of the ray paths is only about 15000. Thus, the lateral resolution of the maps tends to be limited compared to those of Fig. 4.4, although the large-scale features are mostly recovered. It should be noted that, in principle, small-scale structures cannot be resolved well by higher-mode waves, whose wavelengths are longer than those of the fundamental mode in a same period. We can see some smearing effects in the NW-SE direction in maps of Fig. 4.5, since the deep events used in this study, which excites the sufficient energy of higher modes, are mostly located in the NW and SE directions of North America.

To estimate the standard errors of the phase speed maps derived from the eikonal tomography, we performed a jackknife resampling test for the fundamental-mode Rayleigh wave, for which we could gather a large number of ray paths. Our jackknife resamples were generated by removing 10% of the original data (710 events). We created 10 sets of resampled data that are independently used to obtain phase speed maps by the eikonal tomography. The standard deviation $\sigma$ of phase speeds at each grid can be estimated as

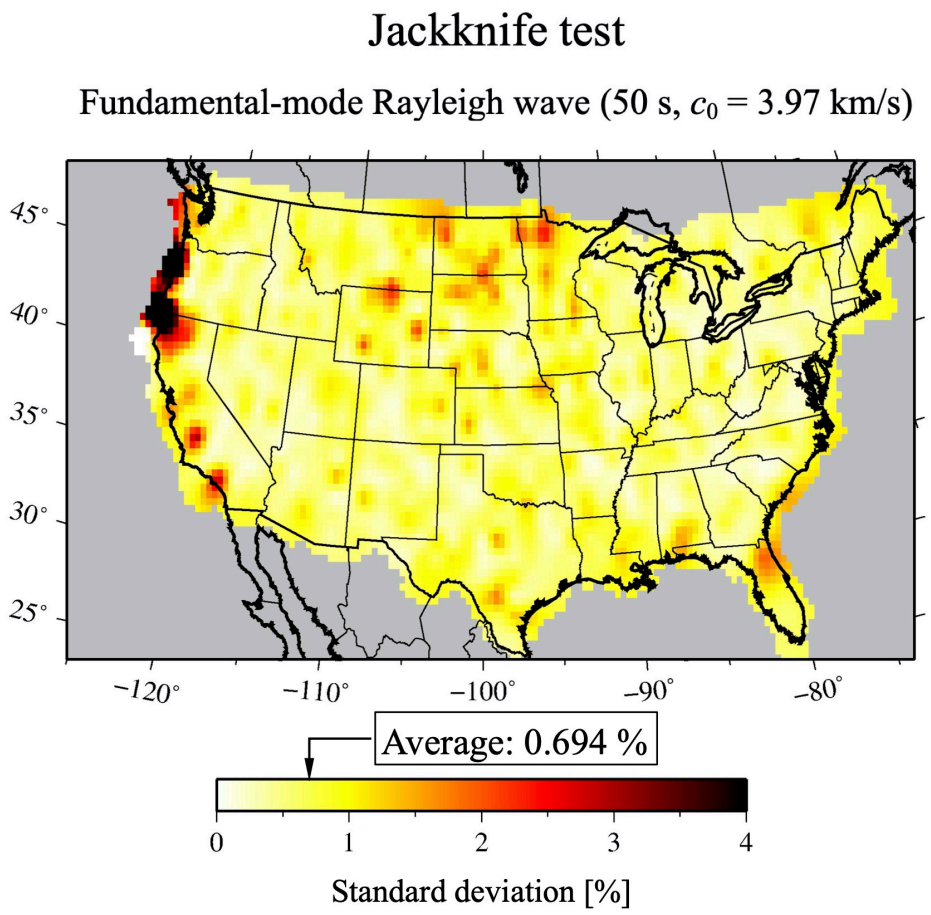



Figure 4.6: Results of jackknife resampling tests for the fundamental-mode Rayleigh wave at 50.0 s: the standard errors of phase speeds obtained by the eikonal tomography.

follows (e.g., Friedl & Stampfer, 2006; Nishimura, 2020):

$$\sigma = \sqrt{\frac{9}{10}\sum_{k=1}^{10}\left\{c\left(k\right) - \bar{c}\right\}^2}, \tag{4.1}$$

where $c(k)$ is the local phase speed derived from the $k$-th data set, and $\bar{c}$ is the average phase speed from 10 resampled data sets. Fig. 4.6 displays the results of the jackknife tests for the fundamental-mode Rayleigh wave at 50 s. The estimated errors are mostly less than 1.0–1.5 %, which are not very significant. We can see that the standard errors tend to be relatively large around the Cascadia subduction zone or the northern part of the Great Plains. Both of them coincide with locations where the lateral changes in seismic structure are relatively large, and ray paths (or phase fronts) are likely to be distorted severely. This result may suggest that the rapid lateral changes in the mantle structure lead to the instability of the derivative calculation in the eikonal tomography.

### 4.3.2 Data for the linearized inversion

For making a comparison, we conducted another phase-speed mapping by the linearized inversion based on the method of surface-wave tomography of Yoshizawa & Kennett (2004), incorporating approximate effects of finite frequency (Yoshizawa & Kennett, 2002b). We used only seismic events with epicentral distances of 8000 km or less resulting in 247 events and 35000 paths for the fundamental-mode Rayleigh waves and 15000–20000 paths for higher-modes, 245 events and 20000 paths for the fundamental-mode Love waves and 5000–10000 paths for higher-mode.

## 4.4 Phase Speed Maps with Single-station and Hybrid Methods

Now we show the phase speed maps derived from our hybrid approach based on the single-station analysis and the eikonal tomography, for the fundamental mode in Fig. 4.7 and 4.9 and for the higher modes in Fig. 4.11 and 4.12 We compare the maps derived from the single-station analysis and the linearized inversions based on the finite-frequency theory, in a similar way to the conventional surface-wave tomography (e.g., Yoshizawa & Ekström, 2010) in Figs. 4.8, 4.10, 4.11 and 4.12.

Phase speed maps in Figs. 4.7–4.12 are displayed as perturbations from the average in the U.S. of our data set. Some examples of vertical sensitivity kernels to S-wave speed for each mode and period are shown in Fig. 1.1.

Phase speed models for the fundamental mode derived from the eikonal tomography (Figs. 4.7 and 4.9) are mostly consistent with those from the linearized tomographic inversions (Figs. 4.8 and 4.10).

A typical large-scale pattern of slow anomalies in the west and fast anomaly in the east are apparent. In addition, relatively small-scale (a few hundred-kilometer-scale) tectonic features have been also imaged clearly, particularly in the eikonal tomography maps. Our fundamental-mode maps, which mostly sample the uppermost mantle, primarily reflect surface tectonic features. Both Rayleigh and Love wave maps of Figs. 4.7 and 4.9 resolve slow anomalies corresponding to the Yellowstone hotspot, the Snake River Plain, the Great Basin, and the Rio Grande Rift in the western U.S. A local fast anomaly corresponding to the Colorado Plateau can also be imaged in the fundamental-mode Rayleigh maps, particularly in a period range shorter than 70 s.

This fast anomaly in the Rayleigh wave model from the linear inversion appears to be shifted to the north from the surface location of the Plateau.

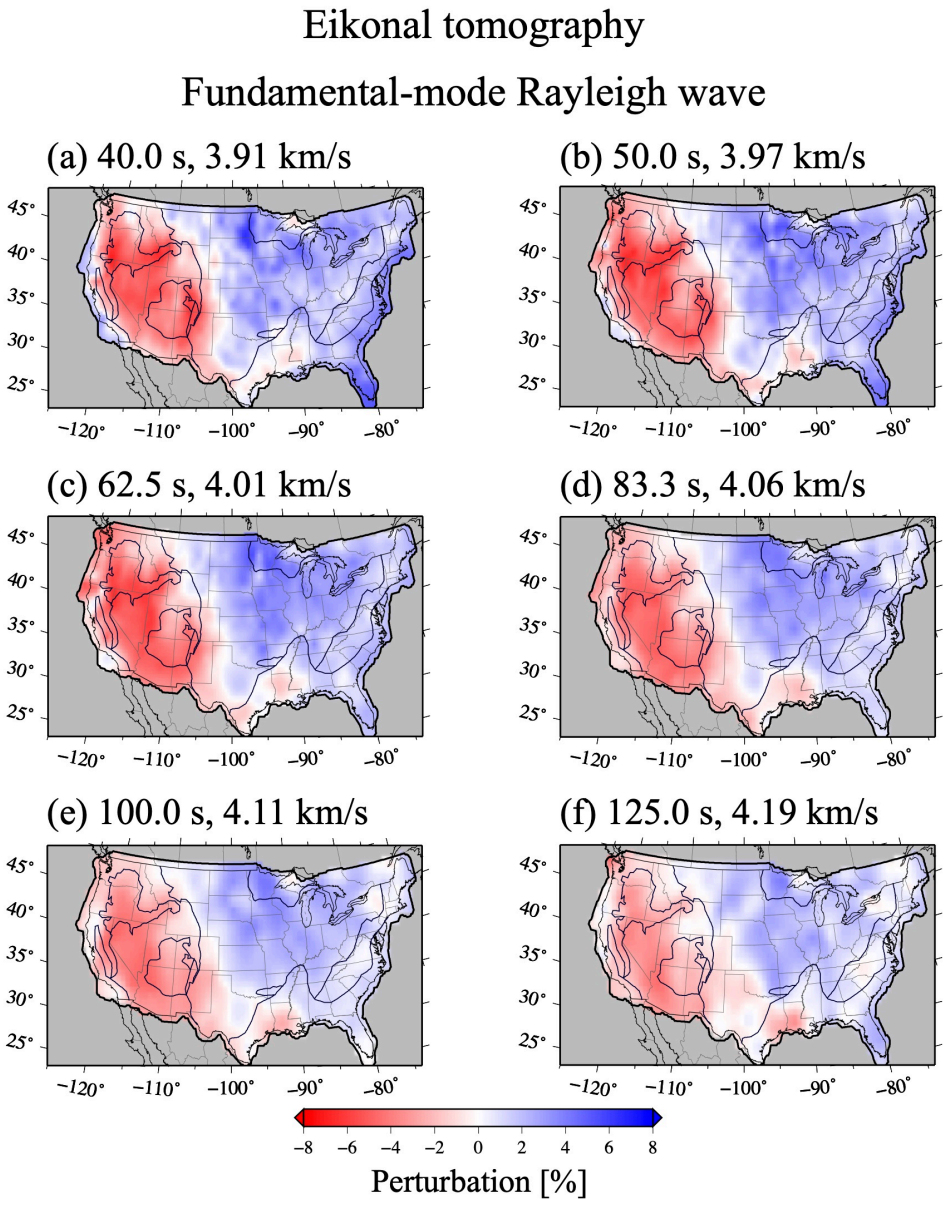



Figure 4.7: Phase speed maps derived from the eikonal tomography in the U.S. for the fundamental-mode Rayleigh wave at a period of (a) 40.0 s, (b) 50.0 s, (c) 62.5 s, (d) 83.3 s, (e) 100.0 s and (f) 125.0 s.

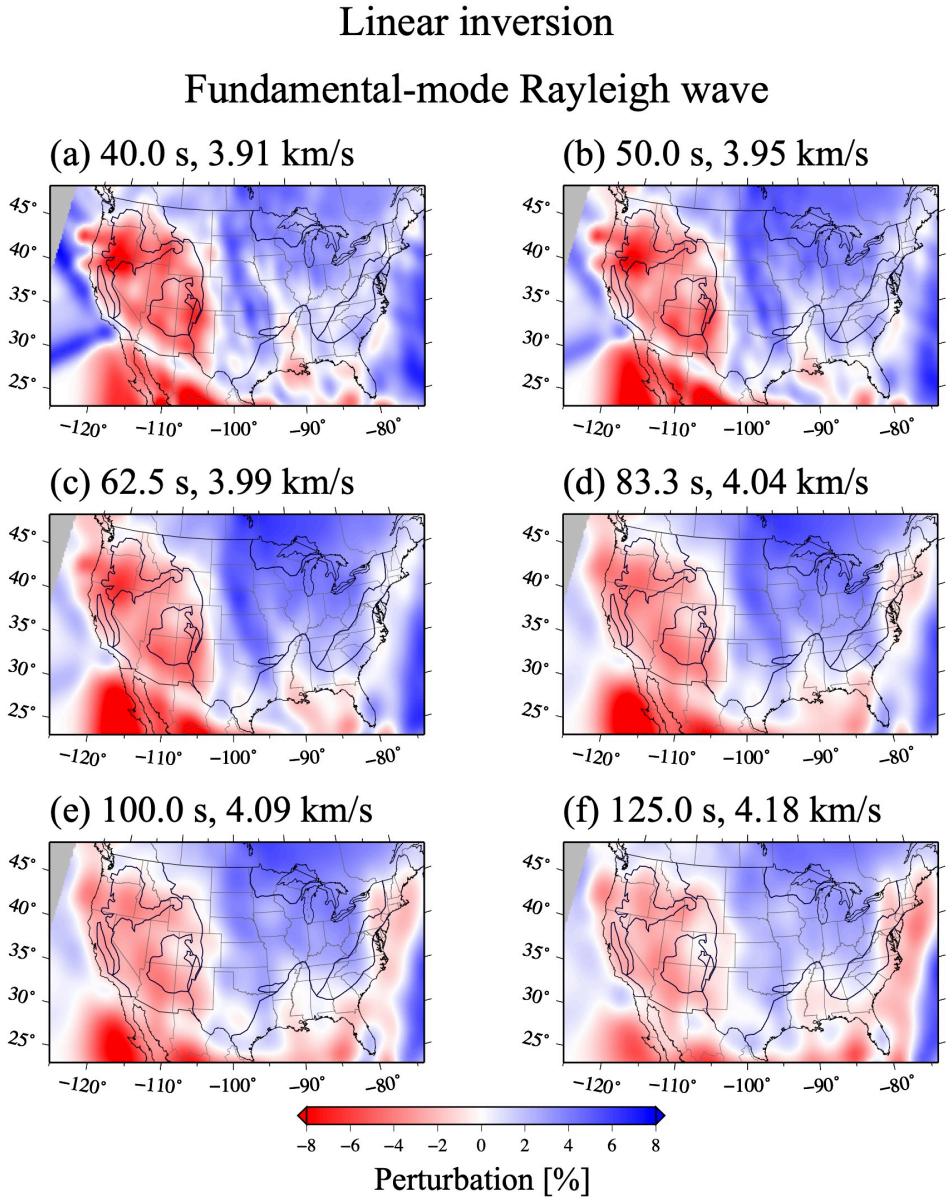



Figure 4.8: Same as Fig. 4.7, but from the linear tomographic inversions.

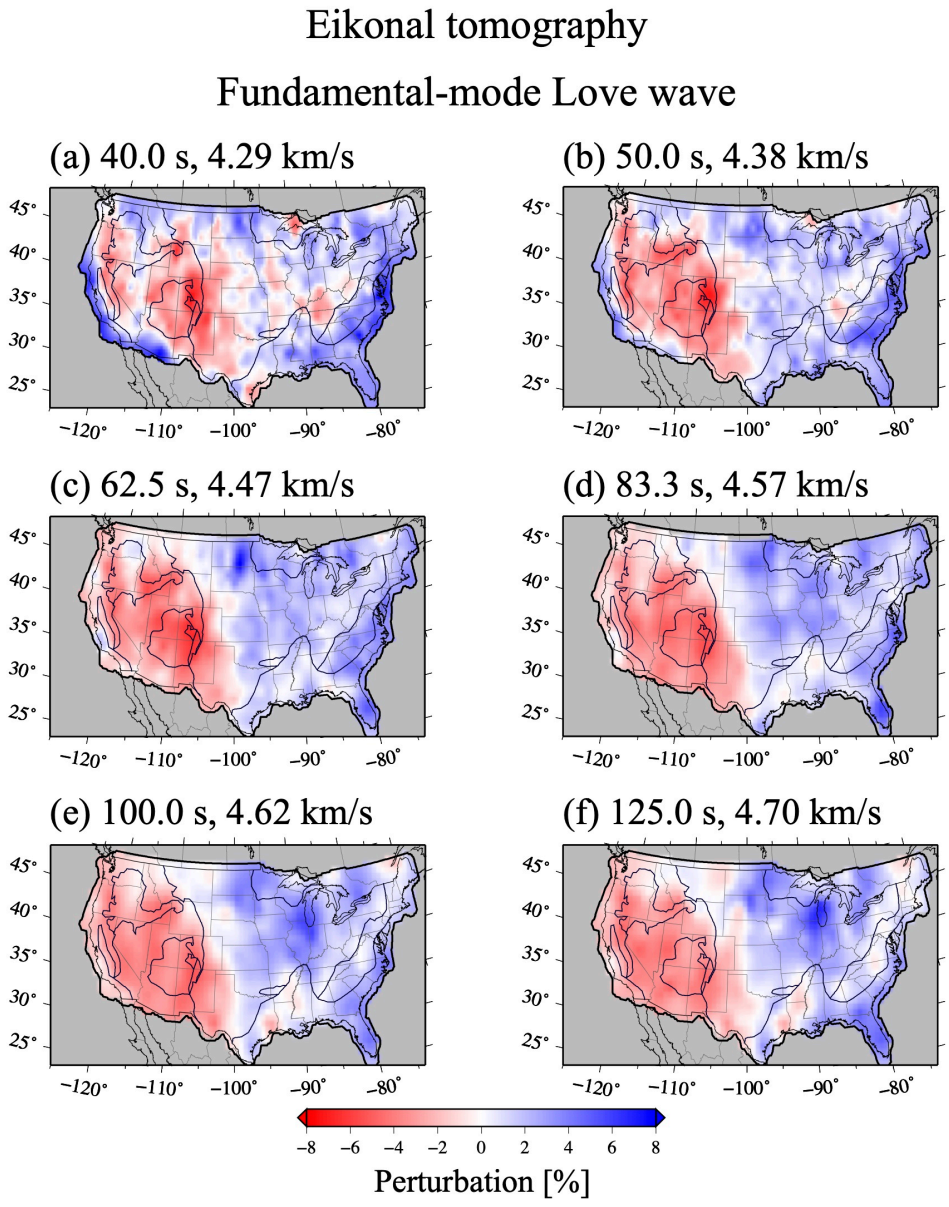



Figure 4.9: Same as Fig. 4.7, but for the fundamental-mode Love wave at a period of (a) 40.0 s, (b) 50.0 s, (c) 62.5 s, (d) 83.3 s, (e) 100.0 s and (f) 125.0 s.

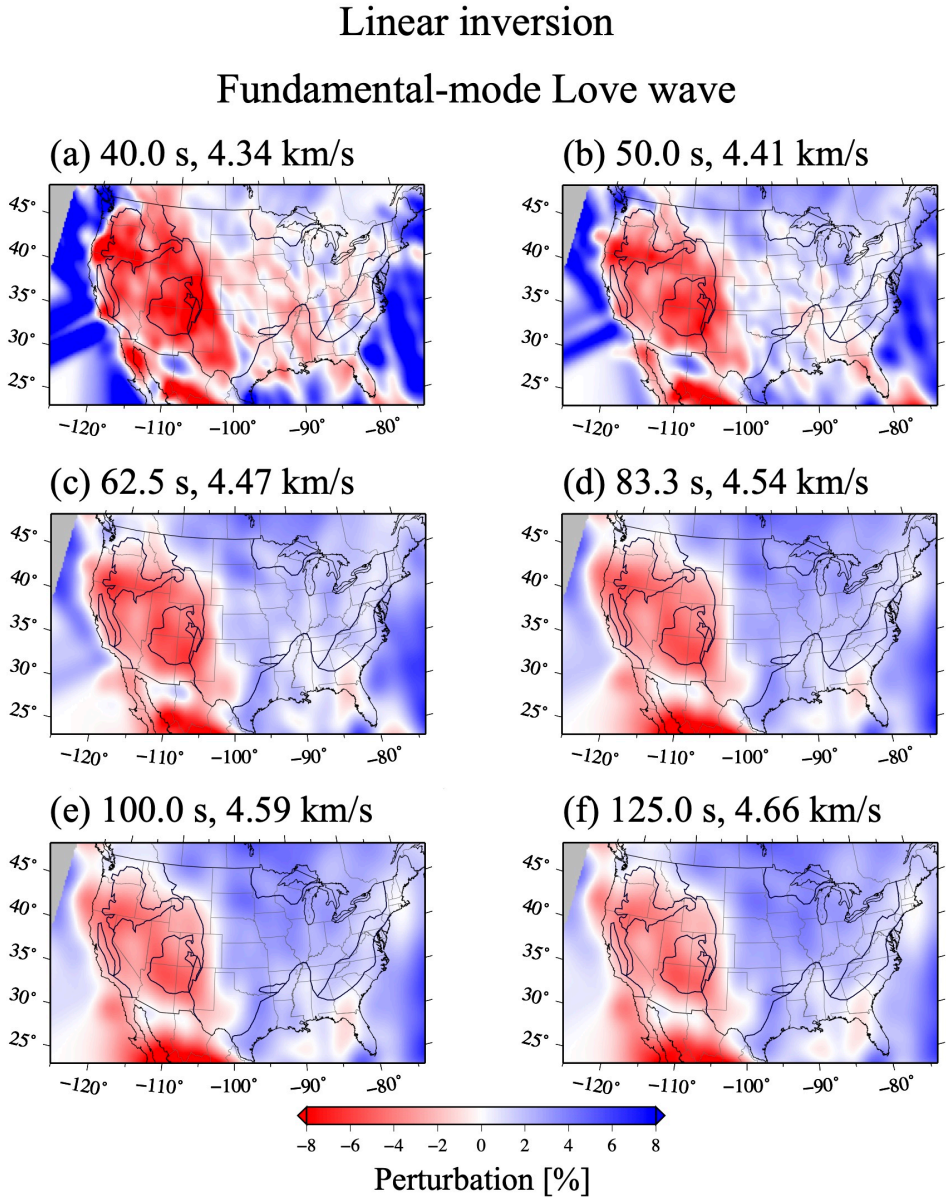



Figure 4.10: Same as Fig. 4.9, but from the linear tomographic inversions.

In the eastern U.S., phase speed maps at all the periods are dominated by the fast anomalies related to the old cratons on the surface.

Higher-mode Rayleigh wave maps of Fig. 4.11 show somewhat smaller perturbations compared to the fundamental mode ones. We can see common features in large-scale heterogeneity distribution with our higher-mode maps obtained from both the linear inversion and the eikonal tomography. A similar feature was found in previous studies on higher-mode dispersion maps of the global scale by Visser et al. (2008) and of the regional scale in North America by Yoshizawa & Ekström (2010). For example, in the second higher-mode Rayleigh maps (Figs. 4.11b), there is a slow anomaly in the south-eastern U.S. On the contrary, the higher-mode Love maps by both the linear inversion and the eikonal tomography in Fig. 4.12 show different anomaly patterns.

Higher mode waves sample the mantle structure in a very different way from the fundamental mode wave (see, Fig. 1.1). Although the 3rd (83.3 s) and the 4th higher-modes (50.0 s) of Rayleigh waves have complicated sensitivities to the upper and lower mantle, their peak sensitivities are located at about 75 km in depth, similar to that of the fundamental-mode Rayleigh wave (50 s). These maps (Figs. 4.11c and d), therefore, show similar features to the fundamental-mode map (Fig. 4.7b), although the strength of heterogeneity tends to be weak in the higher-mode models.

## 4.5 Discussion

In this chapter, the multi-mode phase speed maps have been constructed using a hybrid approach with the single-station multi-mode dispersion analysis (Yoshizawa & Kennett, 2002a; Yoshizawa & Ekström, 2010) and the eikonal tomography (Lin et al., 2009). This method is computationally efficient, and thus it can be applied to large datasets of USArray. In the case of the linear

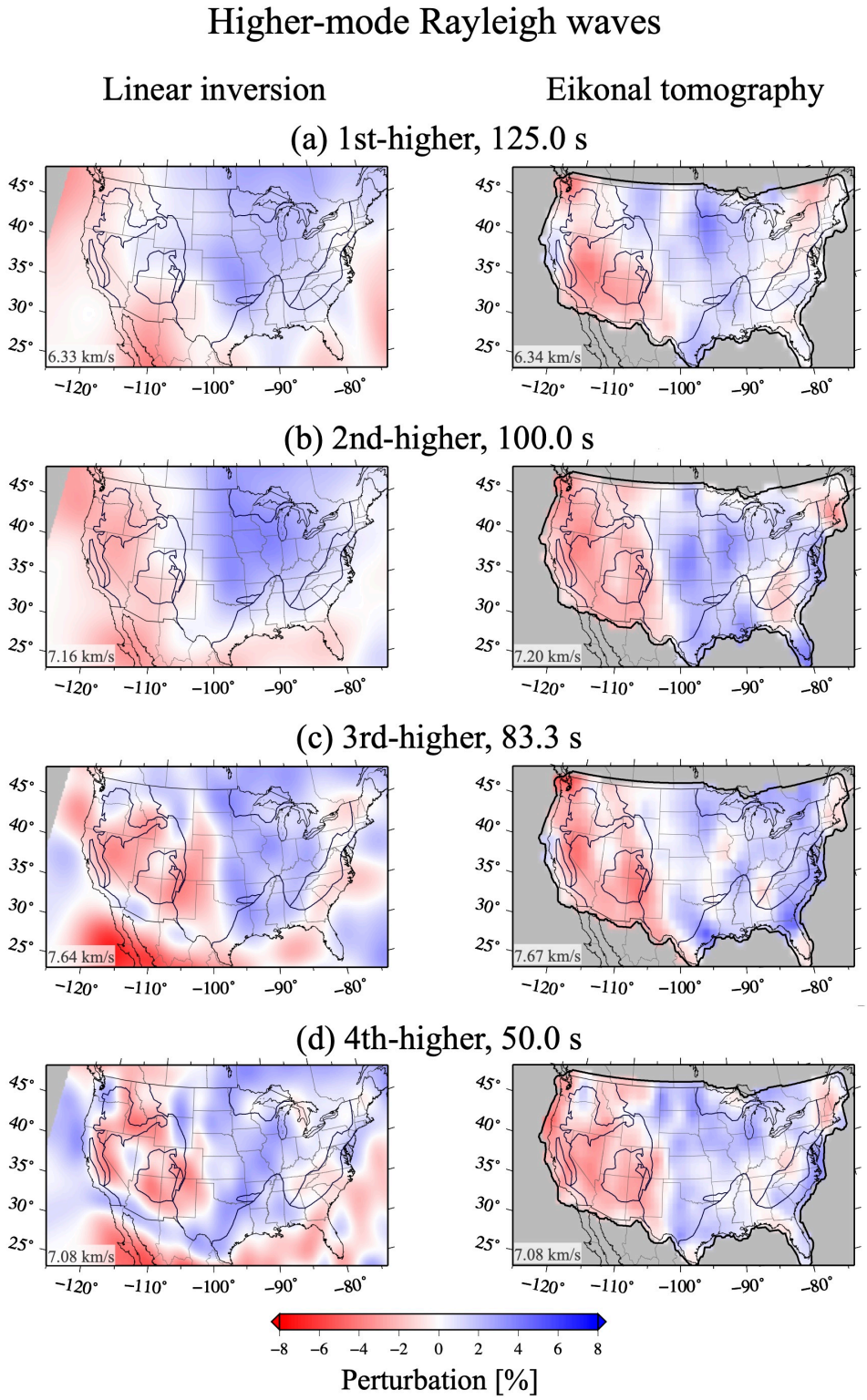



Figure 4.11: Higher-mode Rayleigh wave phase speed maps in the U.S. for (a) the 1st-higher-mode at 125.0 s, (b) the 2nd-higher-mode at 100.0 s, (c) 3rd-higher-mode at 83.3 s, and (d) the 4th-higher-mode at 50.0 s The models are derived from (left) the linear inversion and (right) the eikonal tomography.

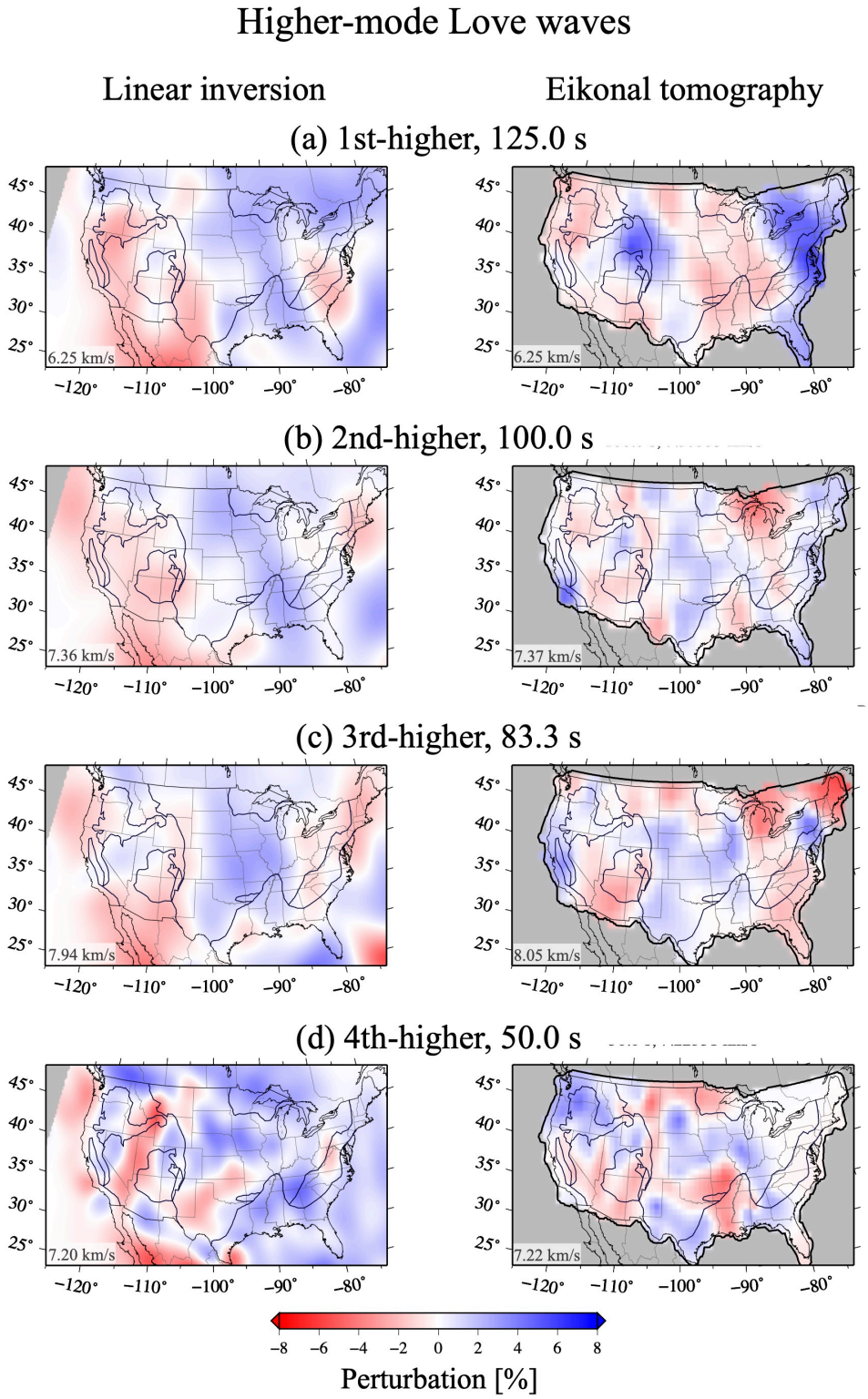



Figure 4.12: Same as Fig. 4.11 but for Love waves for (a) the 1st-higher-mode at 125.0 s, (b) the 2nd-higher-mode at 100.0 s, (c) 3rd-higher-mode at 83.3 s, and (d) the 4th-higher-mode at 50.0 s.

inversions for regional-scale maps, we used only short ray paths for events within the target region of tomographic inversions, which leads to the limited numbers of events and paths. On the contrary, for the eikonal tomography, we can also use long ray paths. Thus the large numbers of events can be used in combination of a dense seismic array, resulting in the high lateral resolution of about $3.0^\circ \times 3.0^\circ$.

The fundamental-mode maps by the linear inversion have enabled us to image large-scale anomalies. However, some small-scale structural features seem to be deviated from realistic geologic features, mainly due to the limited number of crossing paths and an uneven path distribution in target areas. On the other hand, those by the eikonal tomography have successfully imaged small-scale anomalies corresponding to surface geologic features. These results suggest that the single-station multi-mode dispersion measurements by Yoshizawa & Kennett (2002a); Yoshizawa & Ekström (2010) enable us to extract the dispersion curve of each mode, allowing us to extract phase front information across the dense seismic array, and resulting in reliable mappings of phase speed distributions based on the eikonal tomography (Lin et al., 2009).

It should be noted that the fundamental-mode Love waves tend to be contaminated by higher modes since they share similar group speeds. Some earlier studies (Nettles & Dziewoński, 2011; Foster et al., 2014c) have reported that, without proper mode separations, the phase speed measurements of the fundamental-mode Love waves are likely to include large measurement errors of about 10% for inter-station measurements, and up to 20% for mini-array measurements. Since we have separated the modal contributions through the multi-mode waveform analysis in this study, the influence of the higher-mode contamination should have been reduced. Thus, the reliability of our fundamental-mode Love waves measurements is likely to be higher than that

of conventional inter-station or mini-array methods, which directly employ observed waveforms without mode separations. The improved and stable Love wave measurements are essential to improve the accuracy of the final 3-D S-wave models, including the radial anisotropy, which will be discussed in detail in the next chapter.

We have also collected a large number of higher-mode phase speeds, despite the intrinsic difficulties in their measurements, by using the automated method based on the full nonlinear waveform fitting by Yoshizawa & Ekström (2010). The interpretation of higher-mode phase speed maps is generally not straightforward since their vertical sensitivity to the shear-wave structure is much more complicated than the fundamental mode one. Nevertheless, the eikonal tomography maps for higher modes represent reasonable phase speed distributions compared with those by the linear inversions with the limited ray path coverage. Detailed mantle structures should be discussed based on the shear wave speed models obtained from inversions of the multi-mode dispersion maps (in the chapter 5). Combining these high-resolution multi-mode phase speed maps for both Rayleigh and Love waves would allow us to construct a radially anisotropic shear wave structure over a wide depth range in the mantle, which can be derived from a joint inversion of Love and Rayleigh waves.

# Chapter 5

# Radially Anisotropic 3-D Shear Wave Structure in North America Using Array-based Multi-mode Phase Speed Mapping

## 5.1 Introduction

Using the phase speed maps of multi-mode Rayleigh and Love waves obtained in chapter 4, we now construct radially anisotropic 3-D S-wave speed models following the method by Yoshizawa (2014), which is based on the generalized nonlinear least-squares inverse scheme of Tarantola & Valette (1982). Local dispersion curves at each grid point derived from the set of phase speed maps are used to constrain local 1-D shear wave profiles, including radial anisotropy, which eventually form a 3-D anisotropic shear wave model.

## 5.2 Method of Inversions for 1-D S-wave Models

The phase speed maps obtained in chapter 4 can be used to construct 3-D S wave models. In the inversion for a radially anisotropic model, we can use either set of model parameters (a) $[\rho, \alpha, \phi, \beta, \xi, \eta]$ and (b) $[\rho, \alpha_v, \alpha_h, \beta_v, \beta_h, \eta]$. Here, $\rho$ is a density, $\alpha$ represents P-wave speed and $\beta$ S-wave speed. $\alpha_v$ and $\alpha_h$ are respectively PH (horizontally polarized P) and PV (vertically polarized

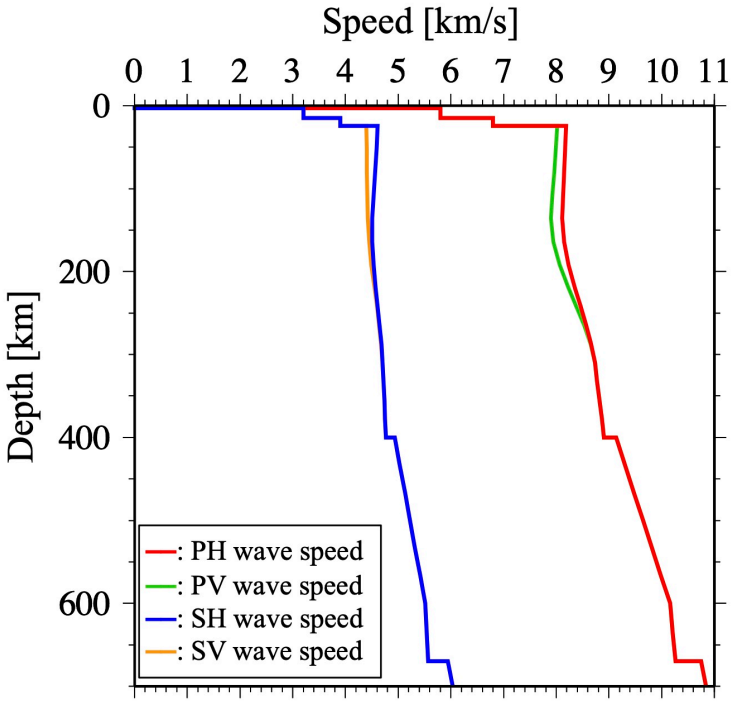



Figure 5.1: 1-D P and S velocity profiles of the anisotropic PREM.

P) wave speeds, $\beta_v$ and $\beta_h$ are respectively SV (vertically polarized S) and SH (horizontally polarized S) wave speeds. $\eta$, $\phi$ and $\xi$ are the anisotropic parameters, where $\eta$ represents the directional dependency of wave speeds, and $\phi = (\alpha_v/\alpha_h)^2$ and $\xi = (\beta_h/\beta_v)^2$, representing the polarization dependency of wave speeds. Through the careful considerations of vertical sensitivity kernels for multi-mode Love waves for these two different sets of parameterizations, Yoshizawa (2014) has argued that the parameter set (a) should be better to be used in the inversions for radially anisotropic S wave models, so we employ the model parameters (a).

The linear relationship between phase speed perturbations and model parameters in this study can be expressed as follows Dahlen & Tromp (e.g., 1998),

$$\frac{\delta c_R^{(n)}}{c_0} = \int_0^{R_E} \left[ K_{\alpha_h}^{(n)} \frac{\delta \alpha_h}{\alpha_{h0}} + K_{\alpha_v}^{(n)} \frac{\delta \alpha_v}{\alpha_{v0}} + K_{\beta_h}^{(n)} \frac{\delta \beta_v}{\beta_{v0}} + K_{\eta}^{(n)} \frac{\delta \eta}{\eta_0} + K_{\rho}^{(n)} \frac{\delta \rho}{\rho_0} \right] dz,$$

for Rayleigh waves, and

$$\frac{\delta c_L^{(n)}}{c_0} = \int_0^{R_E} \left[ K_{\beta_h}^{(n)} \frac{\delta \beta_h}{\beta_{h0}} + K_{\beta_v}^{(n)} \frac{\delta \beta_v}{\beta_{v0}} + K_{\rho}^{(n)} \frac{\delta \rho}{\rho_0} \right] dz,$$

for Love waves, where $R_E$ is the average Earth radius (= 6371 km), $\delta c_R^{(n)}, \delta c_L^{(n)}$ are phase speed perturbation of the $n$th-mode Rayleigh and Love waves. $K_{\rho}^{(n)}$, $K_{\alpha_v}^{(n)}$, $K_{\alpha_h}^{(n)}$, $K_{\beta_v}^{(n)}$ $K_{\beta_h}^{(n)}$ and $K_{\eta}^{(n)}$ are sensitivity kernels to represent the partial derivatives of multi-mode phase speeds with respect to each of the model parameters. The effects of density and P-wave speeds are smaller than those of S-wave speeds. Thus, we take density and P-wave speed into account through a scaling relationship to S-wave speeds as used in Yoshizawa (2014). Therefore, we used only S-wave speed perturbations as independent model parameters for inversions.

In the inversion of a local dispersion curve for a local 1-D shear-wave speed model, we first constructed a local reference model at each point, which

comprises the local crustal structure taken from the 3SMAC model (Nataf & Ricard, 1996) combined with the mantle and core structure from anisotropic PREM (Dziewoński & Anderson, 1981) at the reference period of 1 s, with a modification to smooth the boundary at 220 km in depth. The effects of physical dispersion due to the anelastic attenuation (Kanamori & Anderson, 1977) is taken into account using the $Q$ values of PREM, except that $Q$ for S waves in the crust has been replaced by that of the 3SMAC. In our inversions, the amplitude of shear wave perturbations and the smoothness of vertical variations of the model are controlled by two *a priori* parameters; a standard deviation, $\sigma$, and a correlation length, $L$, which forms a Gaussian function for the covariance matrix used in the inversion (e.g., Nishimura & Forsyth, 1989). In this study, we employed 0.020 km/s, and 5 km above the Moho, 0.030 km/s and 10 km in the upper mantle, 0.050 km/s and 20 km in the mantle transition zone and 0.050 km/s and 30 km in the lower mantle, respectively.

We performed the vertical resolution tests in the same way as Yoshizawa (2014). The Examples are displayed in Fig. 5.2. We created the synthetic 1-D SV and SH wave speed models with a 5%–fast anomaly at the depths of 80 km, 100 km, 150 km, 200 km, 250 km and 300 km. Then, we calculated synthetic dispersion curves for both Love and Rayleigh waves including up to the 4th-higher modes. The period range for each mode is summarized in Table 5.1. As in the real data inversions, we employed the same scaling relations to P wave speeds and density in the calculations of synthetic dispersion data. In each case, we could retrieve the input anomaly fairly well for all the target depths, despite some smearing effects in the deeper structure. The radial anisotropy models calculated from the retrieved SV and SH wave speed profiles were also recovered well.

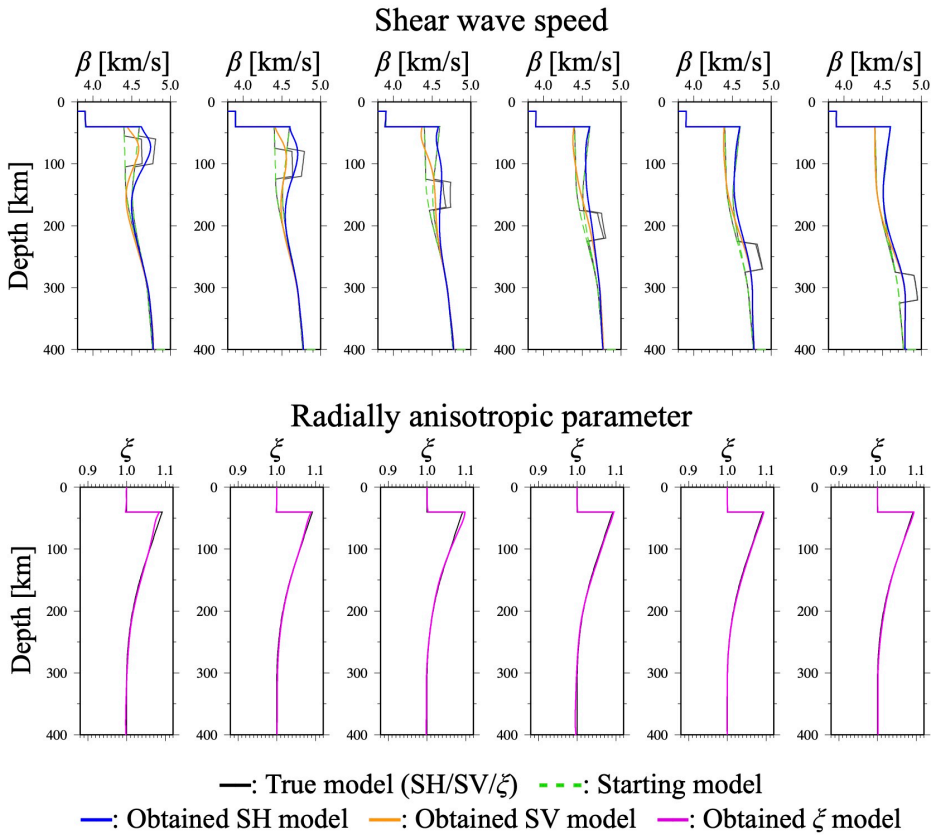



Figure 5.2: Vertical resolution tests for the retrieval of anisotropic 1-D shear wave speed models. All the inversions for SV and SH wave speeds are initiated from the starting models (green solid dashed lines), and resultant models are plotted with solid blue and orange lines in the top panels. The radial anisotropy parameter, $\xi$, in the bottom panels is calculated from the SV and SH wave speed profiles.

## 5.3 3-D S-wave Models in North America with USArray

To construct radially anisotropic 3-D shear-wave models in the contiguous U.S., we applied the iterative nonlinear inversion method by Tarantola & Valette (1982) to the local multi-mode dispersion data derived from the phase speed maps in chapter 4. The period range for each mode used in our inversion is summarized in Table 5.1. A radially anisotropic 3-D S wave model (expressed by the parameters $\beta_v$, $\beta_h$, and $\xi = (\beta_h/\beta_v)^2$), derived from the multi-mode phase speed maps based on the eikonal tomography, is shown in Fig. 5.3 for depths from 60 km to 400 km. We also display five vertical cross-sections across the continent in the east-west directions in Fig. 5.5. We calculate the upper (red solid line) and lower (black and white dashed line) bounds of the Lithosphere–Asthenosphere Transition (LAT), which is originally defined by Yoshizawa (2014) to quantify smoothly varying lithospheric roots derived from surface wave tomography. The upper bound of LAT is determined from the negative peak of the vertical gradient of the 1-D shear wave speed profile, and the lower bound is determined from the slowest shear wave speed in the low-velocity zone beneath the upper bound. We also constructed and compared another 3-D model using the multi-mode phase speed maps based on the linear inversions, as shown in Figs. 5.4 and 5.6. S-wave speed maps and vertical cross-sections are plotted as perturbations from the isotropic PREM in ranging from $-12\%$ to $+12\%$, and $\xi$ from 0.85 to 1.15.

In the uppermost mantle at depth shallower than 200 km, we find large S-wave speed variations over $\pm 6\%$ in Fig. 5.3. These anomalies are consistent with some notable geological features in the U.S., for example, strong lateral velocity contrast between the tectonically active western U.S. and the stable cratonic eastern U.S. At depth shallower than 100 km, the Snake River Plain

can be imaged as a remarkable slow anomaly, and the Colorado Plateau can be imaged as a fast anomaly. The dominant fast anomaly in the eastern region is found down to about 200 km, reflecting a thick cratonic lithosphere in North America (Gung et al., 2003; King, 2005; Yuan & Romanowicz, 2010; Calò et al., 2016). We can also see a fast anomaly extending in NNW–SSE in the western region at a depth of 400 km, which may be related to the subducted Juan de Fuca slab from the Cascadia subduction zone (Sigloch et al., 2008). In the five vertical E-W cross-sections of Fig. 5.5, a sharp contrast between the slow western and the fast eastern U.S. can be seen clearly at the Rocky Mountain front. In the northern cross section at N45°, we can see a deepened portion of the Superior craton around −95°, whose location coincides well with the location of density anomaly that may reflect the deformation of the cratonic root due to the basal drag found in an earlier study of Kaban et al. (2015).

For the radially anisotropic parameter, the entire continent at depths shallower than 100 km is characterized by $\xi > 1$, representing faster SH-wave speed ($\beta_h$) than SV-wave speed ($\beta_v$). This agrees well with the previous tomographic models in both global (e.g. Nettles & Dziewoński, 2008; Chang et al., 2014) and in the regional-scales in North America (e.g. Yuan et al., 2011; Zhu et al., 2017). The $\xi$ values in our models are mostly consistent with those in the model of Nettles & Dziewoński (2008) and Zhu et al. (2017), but larger than those of Yuan et al. (2011). Frozen-in anisotropy is one possible interpretation of the existence of $\xi > 1$ beneath the continent. The contrast of $\xi$ beneath the eastern U.S. suggests that the lithospheric keel of the Superior craton, which corresponds to the LAB, can be estimated at depth of 200–250 km. Deeper than 300 km, the two zones of $\xi < 0.95$ are noticeable: beneath the Cascadia Range and the Superior Craton. When the low $\xi$ is interpreted as the mantle up- or the down-welling, the one beneath the Cascadia Range

Table 5.1: The period ranges of multi-mode phase speed maps used to construct the 3D S-wave models.

| Mode | Rayleigh | Love |
|---|---|---|
| Fundamental mode | 35.7–250.0 s | 35.7–250.0 s |
| 1st-higher mode | 66.7–250.0 s | 83.3–200.0 s |
| 2nd-higher mode | 66.7–200.0 s | 90.9–125.0 s |
| 3rd-higher mode | 55.5–90.9 s | 62.5–83.3 s |
| 4th-higher mode | 40.0–62.5 s | 45.5–55.6 s |

reflects slab subduction, while the other beneath the Superior Craton might reflect the cratonic root delamination. The former is also supported by a fast anomaly in our isotropic S-wave speed model. The latter is consistent with the fast anomaly in the model of Zhu et al. (2017).

## 5.4 Discussion

For the SV- and SH-wave speed structures shallower than 200 km, which is constrained mainly by the fundamental-mode surface waves, we could obtain models with high lateral resolution. The upper mantle at such depth beneath the U.S. is characterized by faster SH wave speed than SV, particularly in the shallow lithosphere (Figs 5.3 and 5.5). The small-scale pattern of the heterogeneity found in the eikonal model well reflects geologic features throughout the U.S. The 3-D models derived from the phase speed maps with the linear inversion (Figs. 5.4a–d) have some patchy or linear features, which may be originated from the uneven path coverage of our data set used to construct the phase speed maps based on the linearized tomographic inversions. On the other hand, our phase speed database in the USArray is sufficiently large enough to construct high-resolution eikonal tomography maps for both Rayleigh and Love waves. In particular, we could successfully separate the influence of the overlapped higher-modes through the nonlinear waveform fitting process. As a result, the subsequent phase-front tracking with the dense

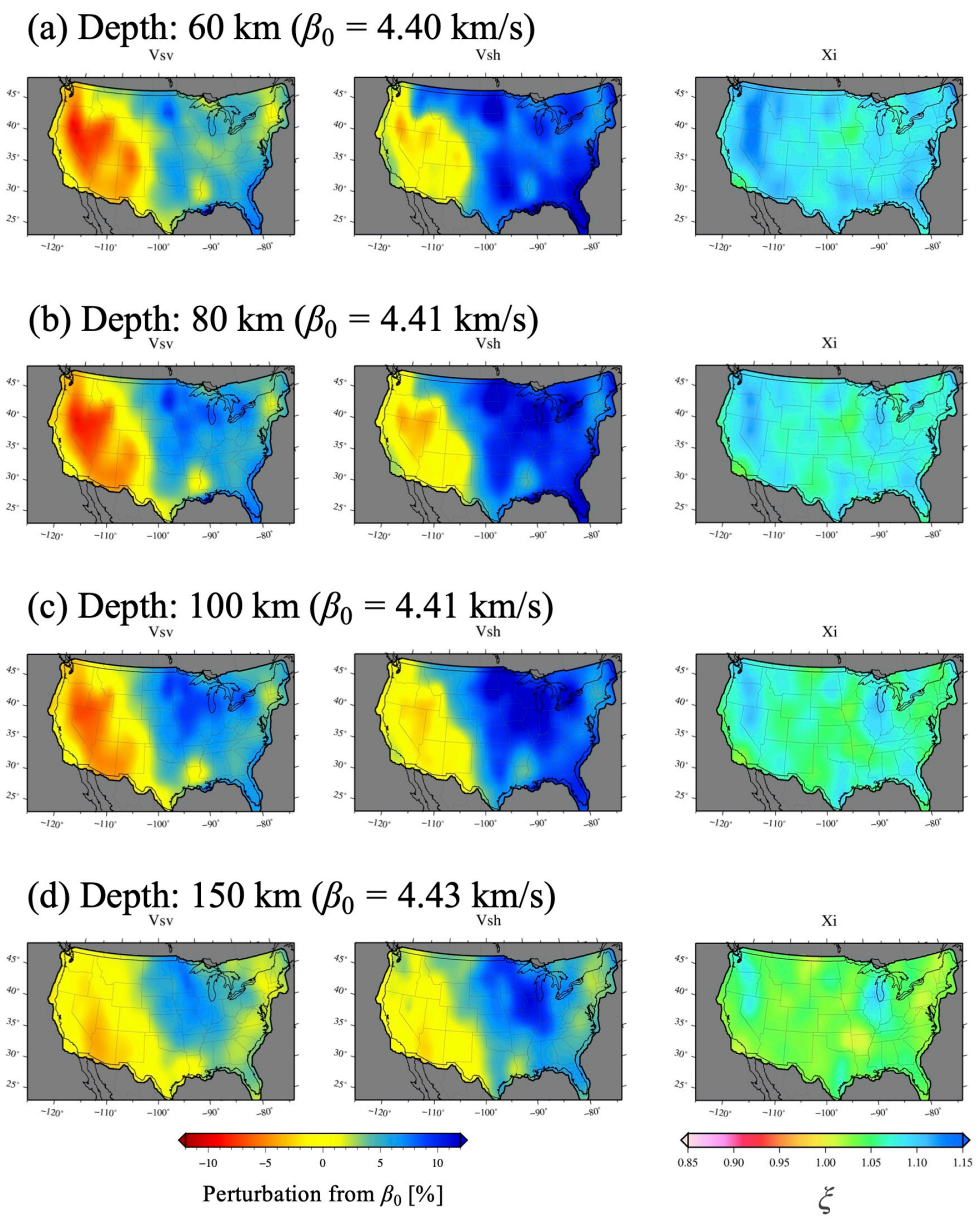



Figure 5.3: Radially anisotropic S-wave speed maps, derived from the phase speed maps based on eikonal tomography, at the depths of (a)60 km, (b)80 km, (c)100 km, (d)150 km, (e)200 km, (f)300 km and (g) 380 km. Left and middle panels show the perturbations of SV- and SH-wave from the average isotropic S-wave speeds in the U.S. Right panel shows the radially anisotropic parameter $\xi = (\beta_h/\beta_v)^2$.

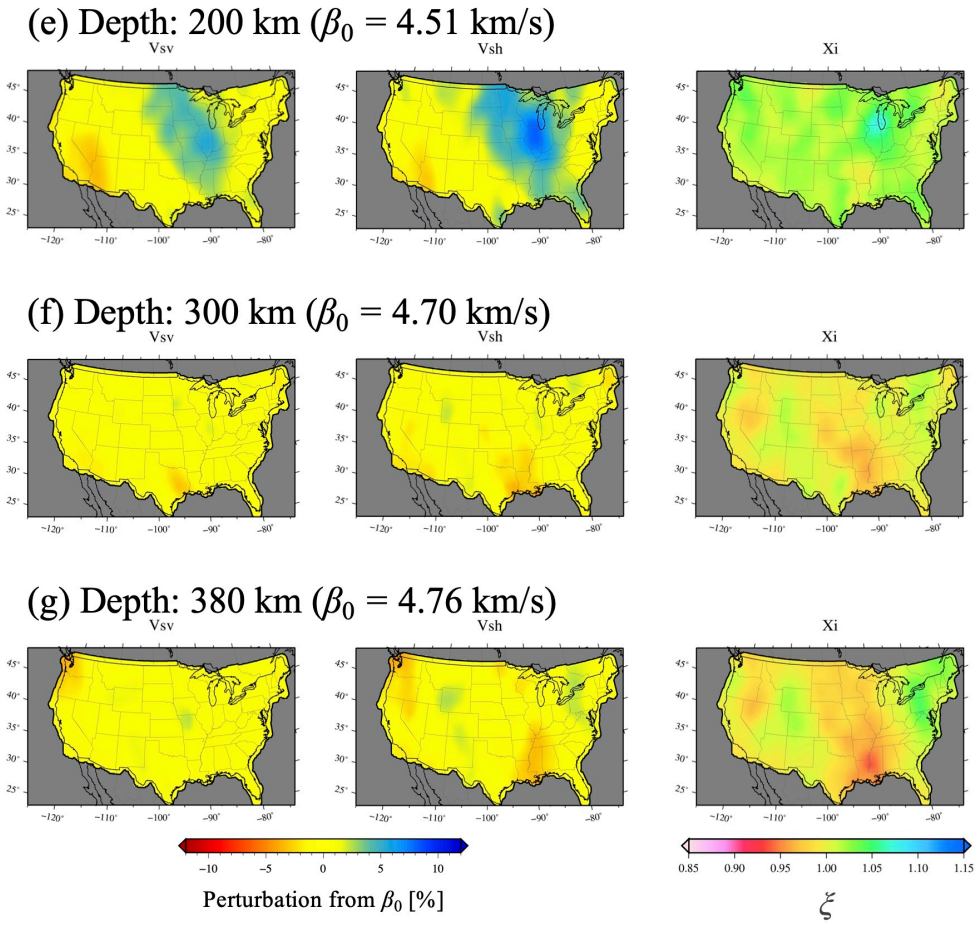



Fig. 5.3 (continue)

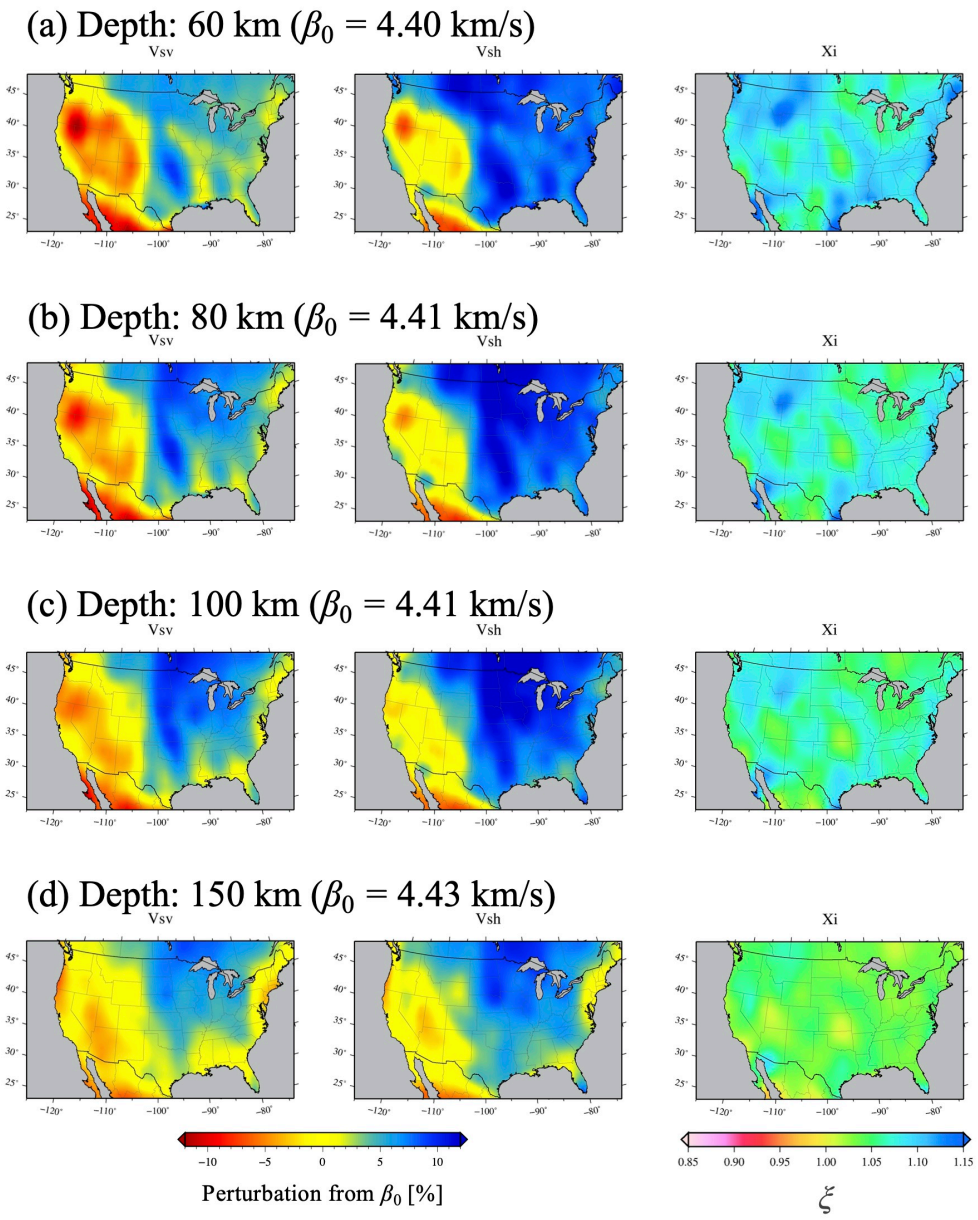



Figure 5.4: Same as Fig. 5.3, but from the phase speed maps based on the linear inversion.

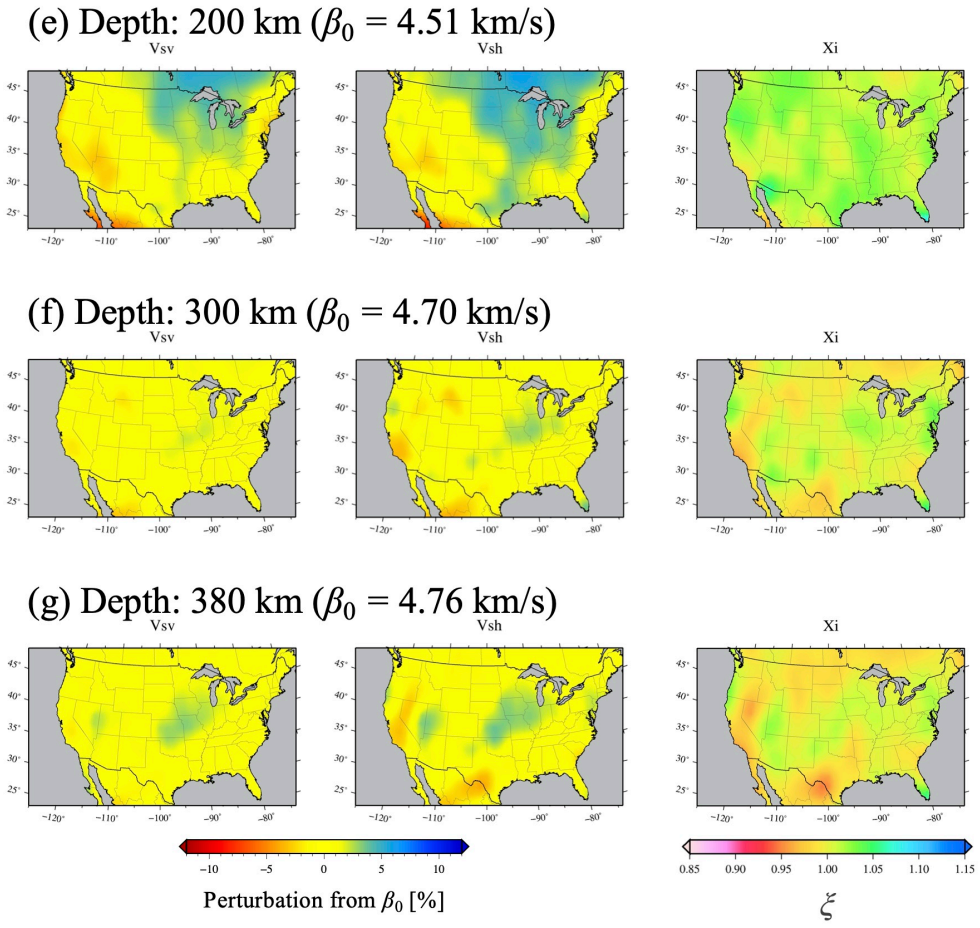



Fig. 5.4 (continue)

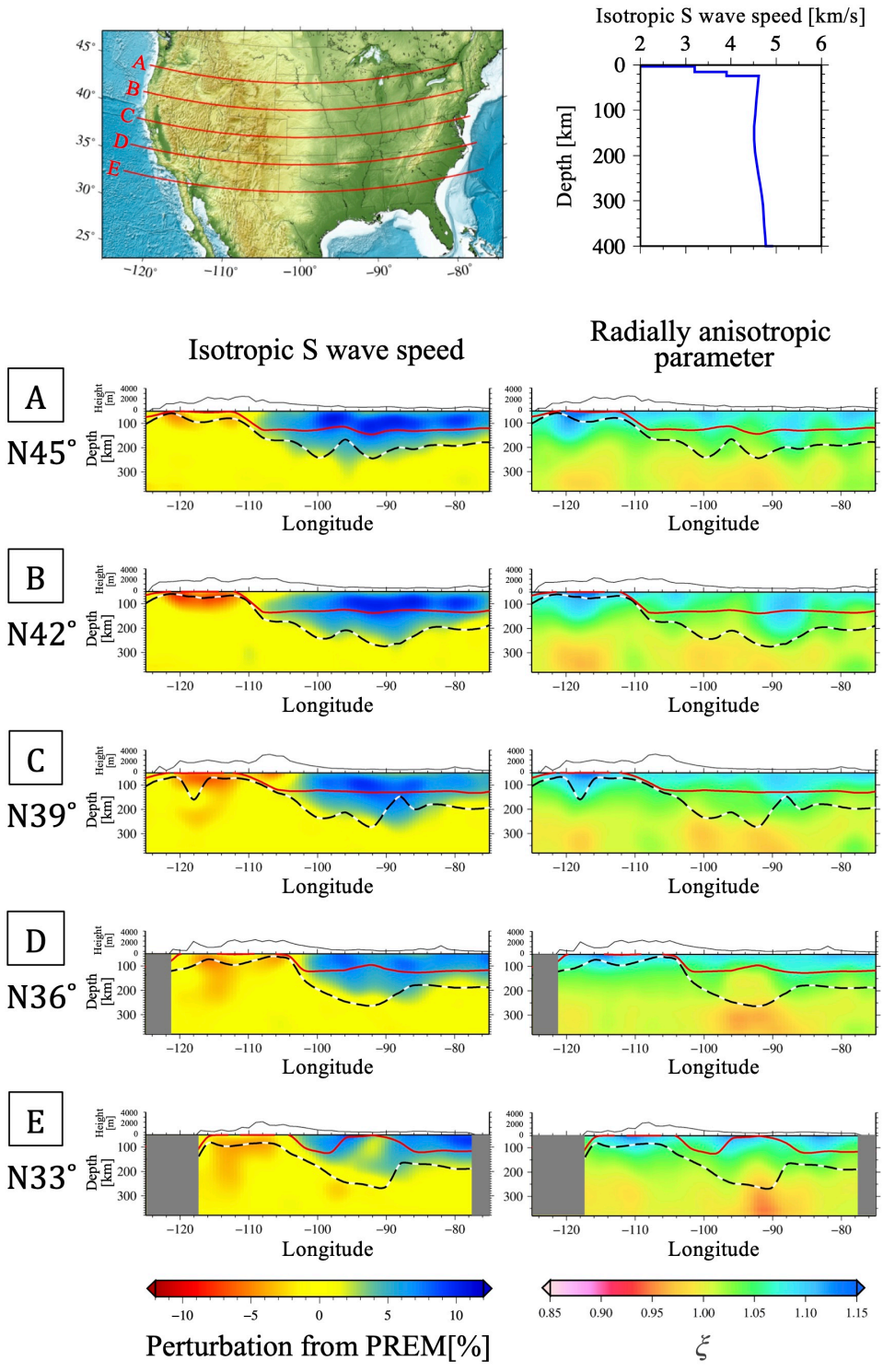



Figure 5.5: Vertical cross-sections of isotropic S wave speed and radial anisotropy models in the E-W direction along the latitudes of (A)45°, (B)42°, (C)39°, (D)36°, and (E)33°, derived from the phase speed maps based on eikonal tomography. The left panel shows the perturbations of isotropic (Voigt-average) shear wave speeds from the PREM in the upper right, and the right panel shows the radially anisotropic parameter $\xi$. The red solid line and black dashed line in the left panels are respectively the upper and lower bounds of LAT. The thin black solid line on the top of each panel represents the topography along the latitudes.

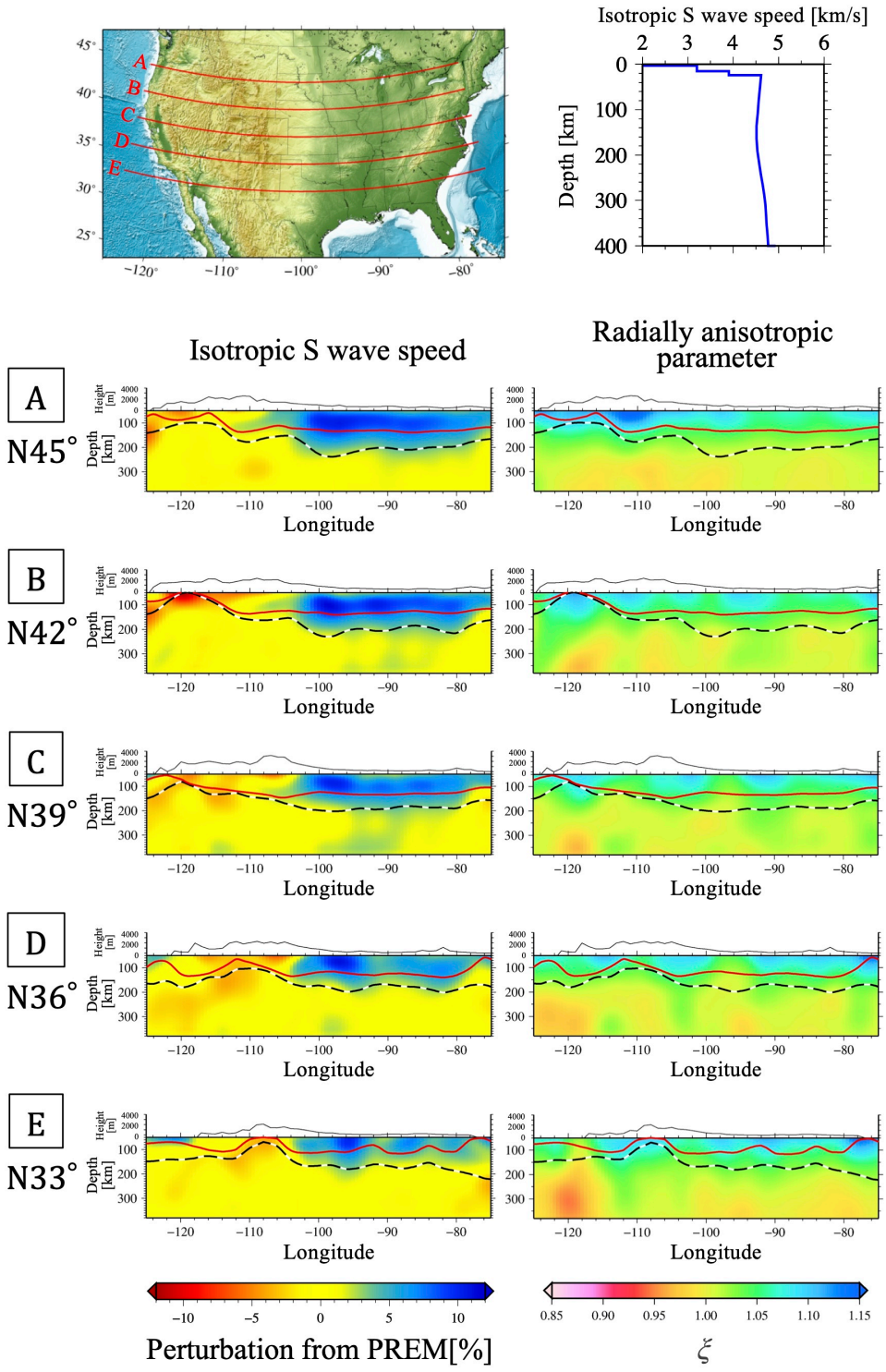



Figure 5.6: Same as Fig. 5.5, from the phase speed maps based on the linear inversion.

seismic array allows us to improve the resolution and accuracy of the phase speed maps, resulting in the robust and reliable 3-D S wave speed model. The present method works well even for Love waves, with limited numbers of ray paths compared with that of Rayleigh waves, enabling us to construct a reliable radially anisotropic S-wave structure. Our anisotropic model is consistent with recent North American models obtained by the adjoint tomography (Zhu et al., 2017) and by the joint inversion of SKS splitting and surface waves (Yuan et al., 2011).

In our S-wave models deeper than 200–250 km, constrained mainly by higher modes, there is noticeable differences between the eikonal and linear inversions due to the difficulty in collecting a number of ray paths that evenly cover the U.S. We can see some artificial features in the linear inversion models, which are not seen in the array-based eikonal tomography model, for example, a fast linear-shaped anomaly in the N-S direction in Figs. 5.4(a-d) and that in the NE-SW direction in Figs. 5.4(f-g) in the central U.S. Since the number of ray paths used for the higher-mode mapping is limited, these models are affected by specific paths with large measurement errors and/or uneven path coverage. In the eikonal tomography, a number of measurements at many seismic stations allow us to avoid such biases in the ray path coverage. In vertical cross-sections of the isotropic S-wave model, the velocity contrast between the western and the eastern U.S. at a depth shallower than 100–150 km is clearly imaged in the eikonal model. On the contrary, such lateral heterogeneities tend to be smoothly varying in the linear inversion model, likely reflecting the effect of smearing due to the longer and uneven paths used in the inversion. This feature directly affects the lateral variations of the estimated LAT depth. In the linear inversion model, the upper and lower bounds of the LAT smoothly vary across the U.S. in the west-east direction in the depth range around 150–250 km. However, in our

eikonal model, we can see significant lateral changes in the LAT across the Rocky Mountains; e.g., the LAT tends to be shallower at around 100–200 km depth in the tectonically active western region but becomes deeper at around 150–300 km depth in the eastern stable cratonic areas. Also, some local tectonic features can be seen in the LAT of the eikonal model; e.g., the lithospheric thinning with the shallow upper bound in the New Madrid Seismic Zone around $-92^\circ$ in Line E of Fig. 5.5. Since the eikonal model can effectively use the relatively small number of higher-mode measurements, both the lateral and vertical resolutions have been improved in our model, allowing us to image the localized lateral variations that reflect surface tectonics and cratonic roots.

In the previous and present chapters, we have shown the multi-mode phase speed distributions together with radially anisotropic shear wave structure in North America. Those inversion results suggest that our hybrid method for the multi-mode surface wave tomography, incorporating multi-mode single-station measurements and the eikonal tomography, can be of help in enhancing both lateral and vertical resolutions. Such an approach with the efficient use of the modern high-density seismic arrays enables us to image the whole upper mantle beneath the continents with much improved resolution.

# Chapter 6

# Conclusions and Future Directions

## 6.1 Summary of this thesis

The use of higher-mode surface waves is essential for enhancing the vertical resolution of 3-D shear wave structure, although the measurement of their phase speeds is intrinsically difficult due to the overlapping of several modes in a recoreded seismogram. In this thesis, we have developed and devised several array-based approaches for analyzing multi-mode dispersions to improve surface wave tomography utilizing a recent high-density seismic network.

First of all, we have developed a two-step array-based method for the multi-mode phase speed measurements based on the $f$–$k$ analysis and the modal waveform decomposition for the centroid location of a long linear array, based on the linear Radon transform. In chapter 2, we explained and demonstrated our linear array analysis through several experiments with synthetic and observed waveforms. The method allows us to measure the multi-mode surface wave dispersions by the classical single-plane-wave beamforming technique. The weighted-average phase speeds within a linear array longer than 2000-3000 km can be obtained precisely in a wide period range in which the wavetrains of several modes overlapped each other in the original data. After determining multi-mode dispersion curves for a long linear array, the linear Radon transform enables us to extract mode-branch waveforms from

a dispersion spectrogram in the $c$–$f$ domain. This approach can be used in the subsequent analysis for further extraction of localized phase speeds, such as inter-station analysis and two-dimensional array analysis. Our numerical experiments with real seismograms observed at USArray also suggest that local phase speeds and propagation direction can be retrieved well from the 2-D array analysis using the mode-branch waveforms.

This linear array analysis has been applied to the large dataset of USArray to map fundamental-mode phase speed distributions in chapter 3. We have employed the inter-station analysis (Hamada & Yoshizawa, 2015) and the eikonal tomography technique (Lin et al., 2009). We have obtained three types of phase speed maps in the U.S.; (a) a low-resolution large-scale heterogeneity model inverted from the average phase speed along each long linear array, and two types of high-resolution maps inverted from (b) average phase speeds of centroid pairs, and (c) the eikonal tomography based on the phase tracking across two-dimensional centroid arrays using mode-branch waveforms. Since the number of employed events is limited (greater than Mw 6.5 in this case), the eikonal models appear to suffer from relatively large measurement errors. On the other hand, the inter-station model enables us to image some small-scale tectonic features.

In chapter 4, as another approach for mapping multi-mode phase speed distributions of surface waves, we have devised a hybrid method combining the single-station dispersion analysis (Yoshizawa & Kennett, 2002a) and the eikonal tomography (Lin et al., 2009). Applying this hybrid technique to USArray data, we have obtained phase speed maps of the first five modes in the U.S. The lateral resolution of the fundamental-mode maps is nearly comparable to recent high-resolution tomographic models in the U.S. We can retrieve the well-known and distinct large-scale heterogeneity contrast between the active western and the stable eastern U.S., as well as the small-

scale anomalies indicating major tectonic features in North America. The higher-mode models can be determined stably in eikonal tomography models since the large number of measurements can be used for near-field and teleseismic events.

In chapter 5, radially anisotropic shear wave structures have been constructed from the multi-mode surface wave models in chapter 4. The multi-mode phase speed maps in a wide period range allow us to image the continental upper mantle to the depth of the mantle transition zone. We can find the deep root of the cratonic lithosphere of North America at 200–250 km depth. The distributions of the radially anisotropic parameter ($\xi$) shows that $\xi > 1$ in North America at depth shallower than 100 km and $\xi < 1$ related to the Juan de Fuca slab subduction and the possible delamination of cratonic keels at depth deeper than 250 km.

## 6.2 Discussion on multi-mode dispersion analyses and their applications to structural reconstruction

In this thesis, we employed two different ways of the multi-mode dispersion analysis; the one based on the long-linear-array analysis (in chapters 2 and 3), and the other based on the hybrid method of the single-station dispersion measurements and the eikonal tomography (in chapters 4 and 5).

In the former case, as mentioned in chapter 2, a linear array longer than 2000–3000 km is required for the precise measurement of higher-mode phase speeds using our linear-array analysis. This style of array-based analysis allows us to measure multi-mode dispersions using only observed waveforms without any synthetics or seismic source mechanism. However, for separating the overlapped modes using the linear array, seismic signals of the target mode and frequency need to propagate a certain distance equivalent to several wavelengths along the array. In practical applications, such a dis-

tance limitation holds an important key. In phase speed mapping using the average phase speeds of long arrays with several thousand kilometers, it is not easy to resolve heterogeneities of a scale of a few hundred kilometers. The method can be used in larger-scale areas where the lateral heterogeneity varies smoothly, such as the oceanic mantle in the Pacific, but it may not be very suitable to resolve regional/local-scale tectonic features in the contiguous United States covered by USArray, whose lateral extent is only about 4000 km in the east-west and about 2000 km in the north-south directions. Also, azimuthal coverages can be limited when we apply the linear array method to USArray, which makes it difficult to reconstruct the phase speed model, including azimuthal anisotropy.

To overcome such intrinsic limitations in the linear-array method for making regional-scale tomography models using USArray, we devised an alternative hybrid approach combining the single-station multi-mode dispersion measurements and the eikonal tomography in the later chapters (4 and 5) of this thesis. Unlike the array-based analysis, the multi-mode dispersion measurements using the single-station method (e.g., Yoshizawa & Kennett, 2002a; Yoshizawa & Ekström, 2010) requires synthetic seismograms using the global CMT solutions. Still, this method does not impose significant restrictions on the propagation distances and has been applied to many regional-scale tomographic studies (e.g., Yoshizawa, 2014; Isse et al., 2019). Thus, we can use many observed waveforms to extract multi-mode dispersion information in the entire array. In the conventional mapping methods using the single-station measurements, path-average phase speeds for many source-receiver pairs have been inverted for tomography models based on linearized inversions. In contrast, we applied the measured multi-mode dispersion data to extract the local multi-mode phase speed structures in the array using the eikonal tomography method. Since this eikonal method requires a very

dense seismic network to properly reconstruct the phase fronts (or travel-time fields) of each mode and frequency, the contiguous U.S. covered by USArray is one of the best-suited target areas of this hybrid approach. The successful recovery of the 3-D tomographic model in the U.S. using our hybrid approach implies the utility of this style of analysis for continental regions with high-density broad-band seismic networks, as discussed in the next section.

Both approaches used in this study have pros and cons, and a proper choice of the method suited for the target areas and the available seismic network is essential. Also, both methods require multiple steps of data processing. To retrieve the precise phase speed models, it is important to eliminate unwanted data that may affect the final results, e.g., observed waveforms with a weak excitation at source, a bad S/N ratio, and phase speed measurements with large errors and lower reliability.

## 6.3 Future directions

Our linear array-based analysis explained in chapter 2 can be applied to ambient noise tomography. In recent years, distributed acoustic sensing (DAS) using fiber-optic telecommunication cables have been used to image subsurface structures (e.g., Dou et al., 2017) as a very dense linear array. By applying the noise cross-correlation for a linear DAS system, it will be possible to measure the phase speed of multi-mode Rayleigh waves at high frequency.

On the other hand, our hybrid approach of the multi-mode phase speed mapping both using the single-station analysis and the eikonal tomography can be used for many recent broad-band seismic networks because there are almost no limitations on the array size required for the multi-mode dispersion measurements with the single-station, although we need high-density broad-band network for high-resolution mapping with the eikonal tomography. There are many possible candidates for further applying our approaches

such as AlpArray in Europe and AusArray in Australia, and a combination of F-net and NECESSArray in Japan and China.

Recently, Taira & Yoshizawa (2020) have developed the joint inversion of P receiver functions and multi-mode surface wave dispersion based on the transdimensional Bayesian approach. Through synthetic experiments, they have revealed that the higher-modes are of great help to recover the radial anisotropy in the whole depth range of the upper mantle. 3-D S wave models derived from the joint inversion of multi-mode surface waves and P receiver functions are expected to improve the accuracy of the retrieved upper mantle structure with discontinuities such as the MLD (Mid-Lithosphere Discontinuity) and LAB (Lithosphere-Asthenosphere Boundary) beneath the continental lithosphere.

# Appendix A

# Methods for Linear Array Analysis

As explained in chapter 2, our array-based multi-mode phase speed measurements are modeled in the frequency-wavenumber ($f$–$k$) analysis for a linear array along a great-circle path originally developed by Nolet (1975, 1976). The subsequent analysis of modal waveform decompositions is based on the linear Radon transform (e.g., Luo et al., 2008, 2009, 2015). In this appendix, we briefly summarize procedures of these two methods. Note that this appendix is based on the electronic supplementary material of our earlier publication (Matsuzawa & Yoshizawa, 2019).

## A.1 Multi-mode Phase Speed Measurements

Here we briefly summarize the data processing procedure for linear array multi-mode dispersion measurements mainly following the descriptions by Nolet (1976).

At first, we apply various group-speed windows to extract seismic signals that propagate with a common group speed. For extracting signals whose group speed is $U$ [km/s] from a seismogram $d_j(t)$ at the $j$-th station ($j = 1, 2, \cdots, N$; where $N$ is the number of stations in an array), we apply a group-speed window whose average arrival time is $x_j/U$ [s] with a window width $w = x_j/\{(1-r)U\} - x_j/\{(1+r)U\}$ [s], where $x_j$ is the epicentral

distance of the $j$-th station in kilometers. A real value $r$ is determined by an empirical relation $r = (1.5U - 3.5) \times 0.01$. Usng a 10 % cosine taper applied to both ends of the time window, the group speed window function $g_j(U,t)$ can be expressed as follows,

$$g_j(U,t) = \begin{cases} 1 & \frac{x_j}{U} - \frac{40}{100}w < t < \frac{x_j}{U} + \frac{40}{100}w, \\ 0 & t < \frac{x_j}{U} - \frac{w}{2}, \frac{x_j}{U} + \frac{w}{2} < t, \\ \frac{1}{2}\left[1 + \cos\left\{\pi\left(1 + \frac{t - x_j/U}{10w/100}\right)\right\}\right] & \text{otherwise.} \end{cases} \tag{A.1}$$

Then, the windowed seismograms $\tilde{d}_j(U,t)$ are given as,

$$\tilde{d}_j(U,t) = d_j(t) \cdot g_j(U,t). \tag{A.2}$$

Next, we generate a beam waveform by stacking windowed seismograms $\tilde{d}_j(U,t)$, assuming a constant phase speed, $c$, across an array. Here, we slant-stacked $\tilde{d}_j$ with respect to the centroid of an array (i.e., reference position) by shifting time with a constant phase speed, which forms the beam $b(c,U,t)$ as follows,

$$b(c,U,t) = \frac{1}{N}\sum_{j=1}^{N} \tilde{d}_j\left(U, t + \frac{x_j - \bar{x}}{c}\right), \tag{A.3}$$

where $\bar{x}$ is the epicentral distance of the centroid of the array, where

$$\bar{x} = \frac{1}{N}\sum_{j=1}^{N} x_j. \tag{A.4}$$

Through this stacking process, coherent signals are enhanced, while incoherent signals and noises are canceled out.

The Fourier spectrum of the beam $B(c,U,\omega)$ is represented as,

$$\begin{aligned} B(c,U,\omega) &= \int b(c,U,t) e^{i\omega t}\, dt \\ &= \frac{1}{N}\sum_{j=1}^{N} D_j(U,\omega) \exp\left(-i\omega \frac{x_j - \bar{x}}{c}\right), \end{aligned} \tag{A.5}$$

where $\omega$ is angular frequency and $D_j(U,\omega)$ is the Fourier spectrum of $\tilde{d}_j(U,t)$. We can rewrite (A.5) by using a wavenumber $k$ $(=\omega/c)$,

$$B(k,U,\omega) = \frac{1}{N}\sum_{j=1}^{N} D_j(U,\omega)\exp[-ik\,(x_j-\bar{x})]\,. \tag{A.6}$$

When $\tilde{d}_j(U,t)$ at $U=U_0$ includes several different surface waves modes (e.g., from $n_{min}$ to $n_{max}$), $D_j(U_0,\omega)$ can be expressed as the summation of multiple modes,

$$D_j(U_0,\omega) = \sum_{n=n_{min}}^{n_{max}} F_{nj}(\omega)\exp\left[i\left\{k_n(\omega)x_j+\phi_{nj}(\omega)\right\}\right], \tag{A.7}$$

where the subscript $n$ indicates the mode number, $F_{nj}$, $k_n(\omega)$ and $\phi_n(\omega)$ are the Fourier spectrum, wavenumber and initial phase of the $n$-th mode for the $j$-th station, respectively. Since the geometry of the array is linear, we can ignore the difference in the radiation pattern of surface waves as long as the azimuth of the ray path is sufficiently away from any nodal directions, so that all the $\phi_{nj}$ become $\phi_n$. With the correction for the effect of geometric spreading, we can replace $F_{nj}=F_n$. Then, (A.7) can be represented as,

$$D_j(U_0,\omega) = \sum_{n=n_{min}}^{n_{max}} F_n(\omega)\exp\left[i\left\{k_n(\omega)x_j+\phi_n(\omega)\right\}\right]. \tag{A.8}$$

By substituting (A.8) into (A.6), we can get the following relation,

$$\begin{aligned} &B(k,U_0,\omega)\\ &= \frac{1}{N}\sum_{j=1}^{N}\left[\sum_{n=0}^{\infty} F_n(\omega)\exp\left[i\left\{k_n(\omega)\Delta_j+\phi_n(\omega)\right\}\right]\right]\exp\left[-ik\left(\Delta_j-\bar{\Delta}\right)\right]\\ &= \sum_{n=n_{min}}^{n_{max}} F_n(\omega)\exp\left[i\left\{k_n(\omega)\bar{x}+\phi_n(\omega)\right\}\right]H(k_n(\omega)-k), \end{aligned} \tag{A.9}$$

where $H(k)$ represents the array response function controlled by the station configuration in an array,

$$H(k) = \frac{1}{N}\sum_{j=1}^{N} \exp\left[ik\left(x_j - \bar{x}\right)\right]. \tag{A.10}$$

An example of the array response function is shown in Fig. 2.3. The central peak of the main lobe of the array response function is one at $k = 0$, accompanied by wiggly sidelobes on both sides. In practice, it is desirable to place seismometers so that the shape of the array response function becomes closer to the delta function.

The beam spectrum is represented as functions of wavenumber $k$, group speed $U$, and angular frequency $\omega$. So, we can make a spectrogram in the $k$–$U$ domain for each $\omega$. Since the beam spectrum obtained by (A.9) represents the weighted average at the centroid location multiplied by the array response function, there are many spurious spectral peaks in the $k$–$U$ spectrogram mainly attributed to the sidelobes of array response.

We can eliminate such spurious peaks and leave only true peaks by the following cleaning process;

1. Define $B_1(k)$ as $B(k, U_0, \omega_0)$, where $U_0$ and $\omega_0$ are target group speed and angular frequency, respectively.

2. Find $k = k_i$ $(i = 1, 2, \cdots)$ for which $|B_i(k)|$ is its maximum, where $i$ denotes the iteration number. Calculate $B_i(k)$ using a recurrence formula, $B_{i+1}(k) = B_i(k) - \gamma B_i(k_i) H(k_i - k)$, where $\gamma$ is a real number $(0 < \gamma \leq 1)$.

3. Find $i_0$ as the maximum of $i$ satisfying $\int |B_i(k)|\, dk > \epsilon \int |B_1(k)|\, dk$, where $\epsilon$ is a real number $(0 < \epsilon \ll 1)$. Calculate $\tilde{B}(k, U_0, \omega_0) = B_{i_0+1}(k) + \gamma \sum_{i=1}^{i_0} B_i(k_i) M(k_i - k)$, where $M(k)$ corresponds to the mainlobe of the array response applied by a narrow wavenumber filter.

4. Calculate $\tilde{B}(k, U, \omega)$ for all the pair of $(U_0, \omega_0)$ to represent a spectrogram with suppressed spurious peaks.

The convergence of this iterative process depends on the selection of arbitrary parameters $\gamma$ and $\epsilon$. We use 0.8 for $\gamma$ and 0.1 for $\epsilon$ which are determined empirically. For the narrow wavenumber filter applied to the array response function to enhance the mainlobe, we employ the Gaussian function whose standard deviation $\sigma$ is set to be 1.0 % of the wavenumber of the fundamental-mode surface wave.

After this cleaning process, we project the $k$–$U$ spectrogram into the $c$–$T$ domain. This procedure is schematically summarized in Fig A.1. In this process, no matter whether a dominant spectral peak exists or not, the maximum value of the cleaned power spectrum $|\tilde{B}(k_0, U, \omega_0)|^2$ at the target wavenumber $k_0$ and angular frequency $\omega_0$ in the $k$–$U$ domain is projected onto a new point $(\omega_0/k_0, 2\pi/\omega_0)$ in the $c$–$T$ domain. The resultant continuous peaks in the $c$-$T$ spectrogram (e.g., Fig. 2.4c) derived from this projection process represent the phase speed dispersion curves of multi-mode surface waves.

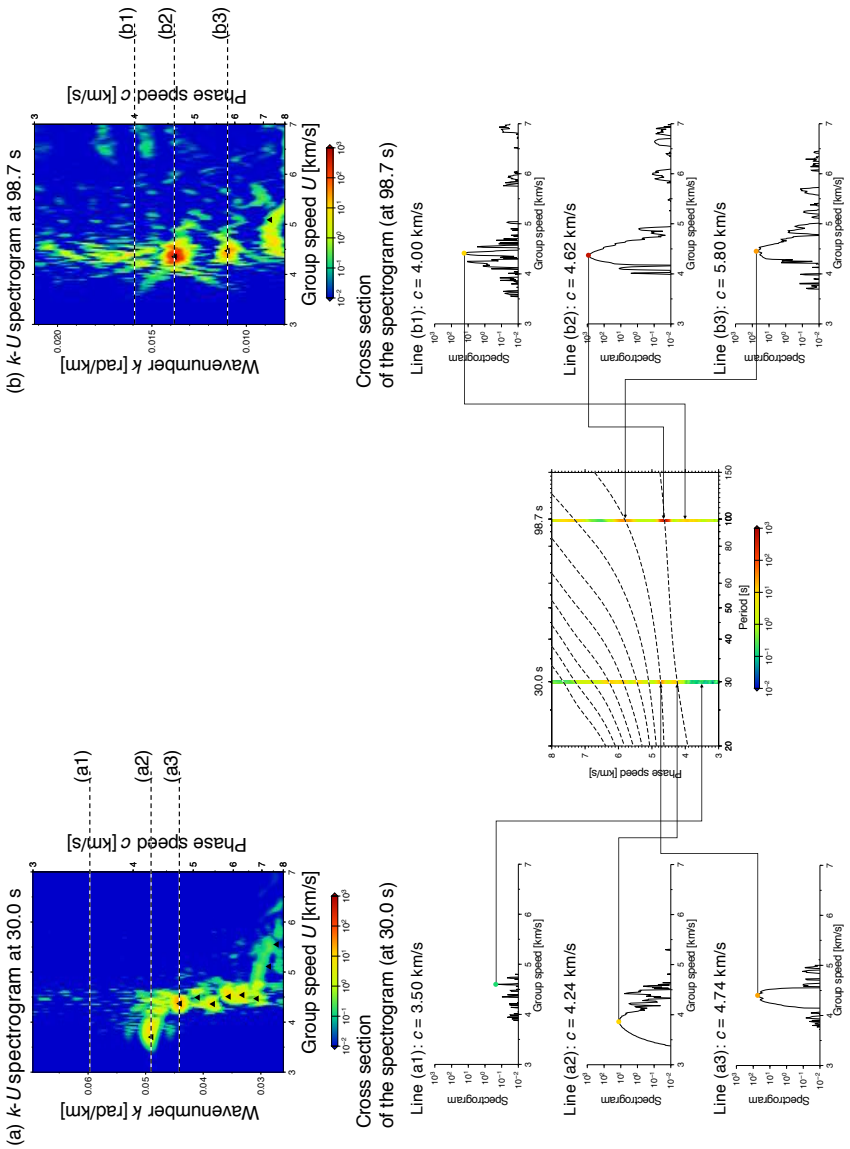



Figure A.1: Schematic diagram of the projection process from the set of spectrograms in the $k$–$U$ domain (top) into the $c$–$T$ spectrogram (bottom center).

## A.2 Linear Radon Transform

In this study, we employ the method based on the linear Radon transform (e.g., Luo et al., 2008, 2009, 2015) for the decomposition of an observed seismogram into modal waveforms as described in chapter 2.2.2. Here we briefly summarize this procedure.

The Fourier spectrum of the observed seismogram $s(x, \omega)$ in an array can be expressed as,

$$s(x, \omega) = \sum_{p=p_{min}}^{p_{max}} m(p, \omega) \exp(i\omega p x), \tag{A.11}$$

where $p$ is the slowness in [s/km] which is the inverse of phase speed $c$, and $m(p, \omega)$ is the spectrum of the seismogram in the $p$-$\omega$ domain. We can rewrite this in a matrix form,

$$\mathbf{d} = \mathbf{L}\mathbf{m}, \tag{A.12}$$

where $\mathbf{d}$ and $\mathbf{m}$ are the vectors of $s$ and $m$, respectively, and the matrix $\mathbf{L}$ is the linear Radon transform operator. The matrix and vector elements of (A.12) can be given explicitly as follows,

$$\begin{pmatrix} s(x_1, \omega) \\ s(x_2, \omega) \\ \vdots \\ s(x_N, \omega) \end{pmatrix} = \begin{pmatrix} e^{i\omega p_1 (x_1 - \bar{x})} & e^{i\omega p_2 (x_1 - \bar{x})} & \dots & e^{i\omega p_{max} (x_1 - \bar{x})} \\ e^{i\omega p_1 (x_2 - \bar{x})} & e^{i\omega p_2 (x_2 - \bar{x})} & \dots & e^{i\omega p_{max} (x_2 - \bar{x})} \\ \vdots & \vdots & \ddots & \vdots \\ e^{i\omega p_1 (x_N - \bar{x})} & e^{i\omega p_2 (x_N - \bar{x})} & \dots & e^{i\omega p_{max} (x_N - \bar{x})} \end{pmatrix} \begin{pmatrix} m(p_1, \omega) \\ m(p_2, \omega) \\ \vdots \\ m(p_{max}, \omega) \end{pmatrix}. \tag{A.13}$$

This linear relationship between the spectrum in the "distance"–"frequency" domain and that in the "slowness (or phase-speed)"–"frequency" domain corresponds to the linear Radon transform (LRT).

The vector $\mathbf{m}$ corresponds to multi-mode dispersion curves as shown in Fig. 2.4. We can, therefore, reconstruct single-mode waveforms in the frequency domain by applying the LRT operator $\mathbf{L}$ to a single-mode dispersion

spectrogram $\mathbf{m}$ extracted from our array-based dispersion analysis. Then, the inverse Fourier transform of $s(x, \omega)$ with respect to the angular frequency $\omega$ will give us the single-mode waveform in the time domain.

# Bibliography


Aki, K. & Richards, P. G., 2002. *Quantitative Seismology, 2nd Ed.*, University Science Books.

Alvizuri, C. & Tanimoto, T., 2011. Azimuthal anisotropy from array analysis of Rayleigh waves in Southern California, *Geophys. J. Int.*, **186**(3), 1135–1151.

Beucler, É., Stutzmann, É., & Montagner, J. P., 2003. Surface wave higher-mode phase velocity measurements using a roller-coaster-type algorithm, *Geophys. J. Int.*, **155**(1), 289–307.

Bodin, T., Leiva, J., Romanowicz, B., Maupin, V., & Yuan, H., 2016. Imaging anisotropic layering with Bayesian inversion of multiple data types, *Geophys. J. Int.*, **206**(1), 605–629.

Busby, R., Woodward, R., Hafner, K., Vernon, F., & Frassetto, A., 2018. *The Design and Implementation of EarthScope's USArray Transportable Array in the Conterminous United States and Southern Canada*, EarthScope.

Calò, M., Bodin, T., & Romanowicz, B., 2016. Layered structure in the upper mantle across North America from joint inversion of long and short period seismic data, *Earth Planet. Sci. Lett.*, **449**, 164–175.

Cara, M., 1978. Regional variations of higher Rayleigh mode phase velocities: a spatial- filtering method, *Geophys. J. R. Astron. Soc.*, **54**(2), 439–460.

Cara, M. & Minster, J. B., 1981. Multi-Mode Analysis of Rayleigh-Type Lg. Part 1. Theory and Applicabability of the Method, *Bull. Seismol. Soc. Am.*, **71**(4), 973–984.

Cara, M., Nercessian, A., & Nolet, G., 1980. New inferences from higher mode data in western Europe and northern Eurasia, *Geophys. J. Int.*, pp. 459–478.

Cara, M., Minster, J. B., & Bras, R. L., 1981. Multi-Mode Analysis of Rayleigh-Type Lg Part 2. Application to Southern California and the Northwestern Sierra Nevada, *Bull. Seismol. Soc. Am.*, **71**(4), 985–1002.

Chang, S.-J., Ferreira, A. M., Ritsema, J., van Heijst, H. J., & Woodhouse, J. H., 2014. Global radially anisotropic mantle structure from multiple datasets: A review, current challenges, and outlook, *Tectonophysics*, **617**, 1–19.

Dahlen, F. A. & Tromp, J., 1998. *Theoretical Global Seismology*, Princeton University Press, Princeton, NJ.

Datta, A., 2019. On the application of the *fk*-MUSIC method to measurement of multimode surface wave phase velocity dispersion from receiver arrays, *J. Seismol.*, **23**(2), 243–260.

Debayle, E. & Kennett, B. L. N., 2000. The Australian continental upper mantle: Structure and deformation inferred from surface waves, *J. Geophys. Res.*, **105**, 25423–25450.

Dou, S., Lindsey, N., Wagner, A. M., Daley, T. M., Freifeld, B., Robertson, M., Peterson, J., Ulrich, C., Martin, E. R., & Ajo-Franklin, J. B., 2017. Distributed Acoustic Sensing for Seismic Monitoring of the Near Surface: A Traffic-Noise Interferometry Case Study, *Sci. Rep.*, **7**(1), 1–12.

Dziewoński, A. M. & Anderson, D. L., 1981. Preliminary reference Earth model, *Phys. Earth Planet. Inter.*, **25**(4), 297–356.

Dziewoński, A. M. & Hales, A. L., 1972. Numerical analysis of dispersed seismic waves, *Methods Comput. Phys.*, **11**, 39–85.

Dziewoński, A. M., Chou, T.-A., & Woodhouse, J. H., 1981. Determination of earthquake source parameters from waveform data for studies of global and regional seismicity, *J. Geophys. Res. Solid Earth*, **86**(B4), 2825–2852.

Ekström, G., 2011. A global model of Love and Rayleigh surface wave dispersion and anisotropy, 25-250s, *Geophys. J. Int.*, **187**(3), 1668–1686.

Ekström, G., 2017. Short-period surface-wave phase velocities across the conterminous United States, *Phys. Earth Planet. Inter.*, **270**, 168–175.

Ekström, G., Tromp, J., & Larson, E. W. F., 1997. Measurements and global models of surface wave propagation, *J. Geophys. Res.*, **102**, 8137–8157.

Ekström, G., Nettles, M., & Dziewoński, A. M., 2012. The global CMT project 2004-2010: Centroid-moment tensors for 13,017 earthquakes, *Phys. Earth Planet. Inter.*, **200-201**, 1–9.

Forsyth, D. W. & Li, A., 2005. Array Analysis of Two-Dimensional Variations in Surface Wave Phase Velocity and Azimuthal Anisotropy in the Presence of Multipathing Interference, *In: Levander A and Nolet G (eds.), Seismic Earth: Array Analysis of Broadband Seismograms. Geophysical Monograph,157*, pp. 81–97.

Foster, A., Ekström, G., & Hjörleifsdóttir, V., 2014a. Arrival-angle anomalies across the USArray Transportable Array, *Earth Planet. Sci. Lett.*, **402**(C), 58–68.

Foster, A., Ekström, G., & Nettles, M., 2014b. Surface wave phase velocities of the Western United States from a two-station method, *Geophys. J. Int.*, **196**(2), 1189–1206.

Foster, A., Nettles, M., & Ekström, G., 2014c. Overtone Interference in array-based love-wave phase measurements, *Bull. Seismol. Soc. Am.*, **104**(5), 2266–2277.

Friedl, H. & Stampfer, E., 2006. Jackknife Resampling, in Encycl. Environmetrics, vol. 2, pp. 1089–1098, eds El-Shaarawi, A. H. & Piegorsch, W. W., John Wiley & Sons Ltd.

Goldstein, P. & Archuleta, R. J., 1987. Array Analysis of Seismic Signals, *Geophys. Res. Lett.*, **14**(1), 13–16.

Gung, Y., Panning, M., & Romanowicz, B., 2003. Global anisotropy and the thickness of continents, *Nature*, **422**(6933), 707–711.

Hamada, K., 2017. *High Resolution Mapping of the Upper Mantle Using Interstation Phase and Amplitude Data of Surface Waves*, Ph.D. thesis, Hokkaido University.

Hamada, K. & Yoshizawa, K., 2015. Interstation phase speed and amplitude measurements of surface waves with nonlinear waveform fitting: Application to USArray, *Geophys. J. Int.*, **202**(3), 1463–1482.

Hariharan, A., Dalton, C. A., Ma, Z., & Ekström, G., 2020. Evidence of Overtone Interference in Fundamental-Mode Rayleigh Wave Phase and Amplitude Measurements, *J. Geophys. Res. Solid Earth*, **125**(1), 1–17.

Isse, T., Kawakatsu, H., Yoshizawa, K., Takeo, A., Shiobara, H., Sugioka, H., Ito, A., Suetsugu, D., & Reymond, D., 2019. Surface wave tomography

for the Pacific Ocean incorporating seafloor seismic observations and plate thermal evolution, *Earth Planet. Sci. Lett.*, **510**, 116–130.

Jin, G. & Gaherty, J. B., 2015. Surface wave phase-velocity tomography based on multichannel cross-correlation, *Geophys. J. Int.*, **201**(3), 1383–1398.

Kaban, M. K., Mooney, W. D., & Petrunin, A. G., 2015. Cratonic root beneath North America shifted by basal drag from the convecting mantle, *Nat. Geosci.*, **8**(10), 797–800.

Kanamori, H. & Anderson, D. L., 1977. Importance of physical dispersion in surface wave and free oscillation problems: Review, *Rev. Geophys. Sp. Phys.*, **15**(1), 105–112.

King, S. D., 2005. Archean cratons and mantle dynamics, *Earth Planet. Sci. Lett.*, **234**(1-2), 1–14.

Laske, G. & Widmer-Schnidrig, R., 2015. *Theory and Observations: Normal Mode and Surface Wave Observations*, vol. 1, Elsevier B.V.

Laske, G., Masters, G., Ma, Z., & Pasyanos, M., 2013. Update on crust1.0 - a 1-degree global model of earth's crust, in Geophys. Res. Abstracts, vol. 15, EGU General Assembly 2013.

Lay, T. & Wallace, T. C., 1995. *Modern Global Seismology*, Academic Press.

Lebedev, S., Nolet, G., Meier, T., & van der Hilst, R. D., 2005. Automated multimode inversion of surface and S waveforms, *Geophys. J. Int.*, **162**(3), 951–964.

Levshin, A. L., Pisarenko, V. F., & Pogrebinsky, G. A., 1972. On a frequency-time analysis of oscillations, *Ann. Geophys.*, **28**(January 1972), 211–218.

Lin, F. C. & Ritzwoller, M. H., 2011. Helmholtz surface wave tomography for isotropic and azimuthally anisotropic structure, *Geophys. J. Int.*, **186**(3), 1104–1120.

Lin, F.-C., Ritzwoller, M. H., & Snieder, R., 2009. Eikonal tomography: Surface wave tomography by phase front tracking across a regional broadband seismic array, *Geophys. J. Int.*, **177**(3), 1091–1110.

Lin, F. C., Schmandt, B., & Tsai, V. C., 2012. Joint inversion of Rayleigh wave phase velocity and ellipticity using USArray: Constraining velocity and density structure in the upper crust, *Geophys. Res. Lett.*, **39**(12), 1–7.

Lin, F. C., Li, D., Clayton, R. W., & Hollis, D., 2013. High-resolution 3D shallow crustal structure in Long Beach, California: Application of ambient noise tomography on a dense seismic array, *Geophysics*, **78**(4).

Luo, Y., Xia, J., Miller, R. D., Xu, Y., Liu, J., & Liu, Q., 2008. Rayleigh-wave dispersive energy imaging using a high-resolution linear radon transform, *Pure Appl. Geophys.*, **165**(5), 903–922.

Luo, Y., Xia, J., Miller, R. D., Xu, Y., Liu, J., & Liu, Q., 2009. Rayleigh-wave mode separation by high-resolution linear radon transform, *Geophys. J. Int.*, **179**(1), 254–264.

Luo, Y., Yang, Y., Zhao, K., Xu, Y., & Xia, J., 2015. Unraveling overtone interferences in Love-wave phase velocity measurements by radon transform, *Geophys. J. Int.*, **203**(1), 327–333.

Masters, G., Woodhouse, J., & Freeman, G., 2011. *Mineos v1.0.2 [software]*, Computational Infrastructure for Geodynamics.

Matsuzawa, H., 2018. *Phase speed measurements of higher-mode surface*

*waves with array-based analysis : Application to USArray*, Master's thesis, Hokkaido University.

Matsuzawa, H. & Yoshizawa, K., 2019. Array-based analysis of multimode surface waves: Application to phase speed measurements and modal waveform decomposition, *Geophys. J. Int.*, **218**(1), 295–312.

Maupin, V., 2011. Upper-mantle structure in southern Norway from beamforming of Rayleigh wave data presenting multipathing, *Geophys. J. Int.*, **185**(2), 985–1002.

Moulik, P. & Ekström, G., 2014. An anisotropic shear velocity model of the Earth's mantle using normal modes, body waves, surface waves and long-period waveforms, *Geophys. J. Int.*, **199**(3), 1713–1738.

Nakanishi, I. & Anderson, D. L., 1982. Worldwide distribution of group velocity of mantle Rayleigh waves as determined by spherical harmonic inversion, *Bull. Seismol. Soc. Am.*, **72**(4), 1185–1194.

Nakanishi, I. & Anderson, D. L., 1983. Measurement of mantle wave velocities and inversion for lateral heterogeneity and anisotropy: 1. Analysis of Great Circle Phase Velocities, *J. Geophys. Res.*, **88**(B12), 10267–10283.

Nataf, H. C. & Ricard, Y., 1996. 3SMAC: An a priori tomographic model of the upper mantle based on geophysical modeling, *Phys. Earth Planet. Inter.*, **95**(1-2), 101–122.

Nettles, M. & Dziewoński, A. M., 2008. Radially anisotropic shear velocity structure of the upper mantle globally and beneath North America, *J. Geophys. Res. Solid Earth*, **113**(2), 1–27.

Nettles, M. & Dziewoński, A. M., 2011. Effect of higher-mode interference on

measurements and models of fundamental-mode surface-wave dispersion, *Bull. Seismol. Soc. Am.*, **101**(5), 2270–2280.

Nishimura, C. E. & Forsyth, D. W., 1989. The anisotropic structure of the upper mantle in the Pacific, *Geophys. J.*, **96**(2), 203–229.

Nishimura, Y., 2020. *Mapping azimuthal anisotropy in the Australasian upper mantle with multi-mode surface waves*, Master's thesis, Hokakido University.

Nolet, G., 1975. Higher Rayleigh modes in western Europe, *Geophys. Res. Lett.*, **2**(2), 6–8.

Nolet, G., 1976. *Higher modes and the determination of upper mantle structure*, Ph.D. thesis, Utrecht University.

Nolet, G., 1990. Partitioned waveform inversion and two-dimensional structure under the network of autonomously recording seismographs, *J. Geophys. Res.*, **95**(89), 8499.

Nolet, G. & Panza, G. F., 1976. Array analysis of seismic surface waves: Limits and possibilities, *Pure Appl. Geophys. PAGEOPH*, **114**(5), 775–790.

Owens, T. J., Crotwell, H. P., Groves, C., & Oliver-Paul, P., 2004. SOD: STANDING ORDER FOR DATA, *Seismological Research Letters*, **75**(4), 515–520.

Paige, C. C. & Saunders, M. A., 1982. LSQR: An Algorithm for Sparse Linear Equations and Sparse Least Squares, *ACM Trans. Math. Softw.*, **8**(1), 43–71.

Reed, J. C. & Bush, C. A., 2007. About the geologic map in the national atlas of the United States of America, Tech. rep., U.S. Geological Survey.

Ritzwoller, M. H. & Levshin, A. L., 1998. Eurasian surface wave tomography: Group velocities, *J. Geophys. Res. Solid Earth*, **103**(B3), 4839–4878.

Ritzwoller, M. H., Lin, F. C., & Shen, W., 2011. Ambient noise tomography with a large seismic array, *Comptes Rendus - Geosci.*, **343**(8-9), 558–570.

Saito, M., 1988. DISPER80: A subroutine package for the calculation of seismic normal-mode solutions, in Seismol. Algorithms Comput. Methods Comput. Programs, chap. IV, pp. 293—-319, ed. Doornbos, D. J., Academic Press, New York.

Sambridge, M., 1999a. Geophysical inversion with a neighbourhood algorithm - I. Searching a parameter space, *Geophys. J. Int.*, **138**(2), 479–494.

Sambridge, M., 1999b. Geophysical inversion with a neighbourhood algorithm–II. Appraising the ensemble, *Geophys. J. Int.*, **138**(3), 727–746.

Schaeffer, A. J. & Lebedev, S., 2014. Imaging the North American continent using waveform inversion of global and USArray data, *Earth Planet. Sci. Lett.*, **402**(C), 26–41.

Schmidt, R. O., 1986. Multiple emitter location and signal parameter estimation, *IEEE Trans. Antennas Propag.*, **34**(3), 276–280.

Shearer, P. M., 1999. *Introduction to Seismology*, Cambridge University Press.

Sigloch, K., McQuarrie, N., & Nolet, G., 2008. Two-stage subduction history under North America inferred from multiple-frequency tomography, *Nature Geoscience*, **1**(7), 458–462.

Stutzmann, E. & Montagner, J. P., 1993. An inverse technique for retrieving higher mode phase velocity and mantle structure, *Geophys. J. Int.*, **113**(3), 669–683.

Taira, T. & Yoshizawa, K., 2020. Upper-mantle discontinuities beneath Australia from transdimensional Bayesian inversions using multimode surface waves and receiver functions, *Geophys. J. Int.*, **223**(3), 2085–2100.

Takeuti, H. & Saito, M., 1972. Seismic surface waves, *Methods Comput. Phys.*, **11**.

Tanimoto, T. & Anderson, D. L., 1985. Lateral Heterogeneity and Azimuthal Anisotropy of the Upper Mantle: Love and Rayleigh Waves 100-250 s, *J. Geophys. Res.*, **90**, 1842–1858.

Tanimoto, T. & Prindle, K., 2011. Surface wave analysis with beamforming, *Earth, Planets Sp.*, **59**, 453–458.

Tanimoto, T. & Tsuboi, S., 2009. Variational principle for Rayleigh wave ellipticity, *Geophys. J. Int.*, **179**(3), 1658–1668.

Tarantola, A. & Valette, B., 1982. Generalized nonlinear inverse problems solved using the least squares criterion, *Rev. Geophys.*, **20**(2), 219.

Trabant, C., Hutko, A. R., Bahavar, M., Karstens, R., Ahern, T., & Aster, R., 2012. Data Products at the IRIS DMC: Stepping Stones for Research and Other Applications, *Seismological Research Letters*, **83**(5), 846–854.

Trampert, J. & Woodhouse, J. H., 1995. Global phase velocity maps of Love and Rayleigh waves between 40 and 150 s, *Geophys. J. Int.*, **122**(February), 675–690.

Tsuboi, S. & Saito, M., 1983. Partial derivatives of Rayleigh wave particle motion, *J. Phys. Earth*, **31**(2), 103–113.

van der Lee, S. & Nolet, G., 1997a. Upper mantle S velocity structure of North America, *J. Geophys. Res.*, **102**(B10), 22815–22838.

van der Lee, S. & Nolet, G., 1997b. Seismic image of the subducted trailing fragments of the Farallon plate, *Nature*, **386**(6622), 266–269.

van Heijst, H. J. & Woodhouse, J., 1997. Measuring surface-wave overtone phase velocities using a mode-branch stripping technique, *Geophys. J. Int.*, **131**(2), 209–230.

van Heijst, H. J. & Woodhouse, J., 1999. Global high-resolution phase velocity distributions of overtone and fundamental-mode surface waves determined by mode branch stripping, *Geophys. J. Int.*, **137**(3), 601–620.

Visser, K., Lebedev, S., Trampert, J., & Kennett, B. L., 2007. Global Love wave overtone measurements, *Geophys. Res. Lett.*, **34**(3), 2–6.

Visser, K., Trampert, J., & Kennett, B. L. N., 2008. Global anisotropic phase velocity maps for higher mode Love and Rayleigh waves, *Geophys. J. Int.*, **172**(1), 1016–1032.

Wessel, P., Smith, W. H. F., Scharroo, R., Luis, J., & Wobbe, F., 2013. Generic Mapping Tools: Improved Version Released, *Eos Trans. AGU*, **94**(45), 409–410.

Wielandt, E., 1993. Propagation and Structural Interpretation of Non-Plane Waves, *Geophysical Journal International*, **113**(1), 45–53.

Xu, H. & Beghein, C., 2019. Measuring higher mode surface wave dispersion using a transdimensional Bayesian approach, *Geophys. J. Int.*, **218**(1), 333–353.

Yoshizawa, K., 2014. Radially anisotropic 3-D shear wave structure of the Australian lithosphere and asthenosphere from multi-mode surface waves, *Phys. Earth Planet. Inter.*, **235**, 33–48.

Yoshizawa, K. & Ekström, G., 2010. Automated multimode phase speed measurements for high-resolution regional-scale tomography: application to North America, *Geophys. J. Int.*, **183**(3), 1538–1558.

Yoshizawa, K. & Kennett, B. L., 2002a. Non-linear waveform inversion for surface waves with a neighbourhood algorithm - Application to multimode dispersion measurements, *Geophys. J. Int.*, **149**(1), 118–133.

Yoshizawa, K. & Kennett, B. L. N., 2002b. Determination of the influence zone for surface wave paths, *Geophys. J. Int.*, **149**(2), 440–453.

Yoshizawa, K. & Kennett, B. L. N., 2004. Multimode surface wave tomography for the Australian region using a three-stage approach incorporating finite frequency effects, *J. Geophys. Res. Solid Earth*, **109**(B2), 1–19.

Yuan, H. & Romanowicz, B., 2010. Lithospheric layering in the North American craton, *Nature*, **466**(7310), 1063–1068.

Yuan, H., Romanowicz, B., Fischer, K. M., & Abt, D., 2011. 3-D shear wave radially and azimuthally anisotropic velocity model of the North American upper mantle, *Geophys. J. Int.*, **184**(3), 1237–1260.

Zhou, L., Xie, J., Shen, W., Zheng, Y., Yang, Y., Shi, H., & Ritzwoller, M. H., 2012. The structure of the crust and uppermost mantle beneath South China from ambient noise and earthquake tomography, *Geophys. J. Int.*, **189**(3), 1565–1583.

Zhu, H., Komatitsch, D., & Tromp, J., 2017. Radial anisotropy of the North American upper mantle based on adjoint tomography with USArray, *Geophys. J. Int.*, **211**(1), 349–377.